5-1-2010

# Nanophotonic and nanoplasmonic couplers: Analysis and fabrication

Rami Wahsheh

# NANOPHOTONIC AND NANOPLASMONIC COUPLERS: ANALYSIS AND FABRICATION

by

Rami A. Wahsheh

A DISSERTATION

Submitted in partial fulfillment of the requirements
For the degree of Doctor of Philosophy
in
Microsystems Engineering
at the
Rochester Institute of Technology

May 2010

Author: _____
Microsystems Engineering Program

Certified by: _____
Mustafa A. G. Abushagur
Professor of Microsystems Engineering

Approved by: _____
Bruce Smith
Director of the Microsystems Engineering Program

Certified by: _____
Harvey J. Palmer
Dean of the Kate Gleason College of Engineering

# NOTICE OF COPYRIGHT



**REPRODUCTION PERMISSION STATEMENT:**

Permission Granted

**TITLE:**

**"Nanophotonic and Nanoplasmonic Couplers: Analysis and Fabrication"**

I, *Rami A. Wahsheh*, hereby grant permission to the Wallace Library of the Rochester Institute of Technology to reproduce my dissertation in whole or in part. Any reproduction will not be for commercial use or profit.

Signature of Author: _____ Date: _____

# Nanophotonic and Nanoplasmonic Couplers: Analysis and Fabrication

by

Rami A. Wahsheh

Submitted by Rami A. Wahsheh in partial fulfillment of the requirements for the degree of Doctor of Philosophy in Microsystems Engineering and accepted on behalf of the Rochester Institute of Technology by the dissertation committee.

We, the undersigned members of the Faculty of the Rochester Institute of Technology, certify that we have advised and/or supervised the candidate on the work described in this dissertation. We further certify that we have reviewed the dissertation manuscript and approve it in partial fulfillment of the requirements of the degree of Doctor of Philosophy in Microsystems Engineering.

**Approved by:**

Dr. Mustafa A. G. Abushagur _____
(Committee Chair and Dissertation Advisor) Date

Dr. Zhaolin Lu _____

Dr. Stefan Preble _____

Dr. Thomas Smith _____

MICROSYSTEMS ENGINEERING PROGRAM
ROCHESTER INSTITUTE OF TECHNOLOGY
May 2010

# ABSTRACT

Kate Gleason College of Engineering
Rochester Institute of Technology

Degree: Doctor of Philosophy Program: Microsystems Engineering

Name of Candidate: Rami A. Wahsheh

Title: Nanophotonic and Nanoplasmonic Couplers: Analysis and Fabrication

Mode mismatch between waveguides of different geometries and propagation mechanisms causes radiation and back reflection, which results in significant loss of optical power. This is considered one of the obstacles that prevents multiple applications of the optical integrated circuits. In this dissertation, we design, fabricate, and experimentally demonstrate four novel photonic couplers that achieve mode matching between hybrid waveguides. These hybrid waveguides include conventional optical waveguides, photonic crystal (PC) waveguides, and plasmonic waveguides. First, we propose a novel method to enhance the coupling efficiency between a dielectric waveguide and a planar PC. This method is based on introducing structural imperfections that cause a change in the mode size and shape inside the taper to match that of the PC line-defect waveguide. These imperfections are introduced by changing the size and position of the inner taper rods. Our results show that introducing the structural imperfections increases the coupling to 96% without affecting the transmission spectrum of the structure. Second, we demonstrate through numerical simulations and experiments that low crosstalk between two crossed line-defect waveguides formed in a square lattice PC structure can be achieved by using a resonant cavity at the intersection area. The PC resonator consists of cubic air-holes in silicon. The theoretical and experimental crosstalk values are approximately -40 dB and -20 dB, respectively. Third, we introduce a novel silicon microring vertical coupler that efficiently couples light into a silicon-on-insulator (SOI) waveguide. A specific mode is excited to match the effective index of the SOI guided mode by oblique incidence. The vertical leakage from the microring forms gradual coupling into the SOI slab. Coupling efficiency up to 91% is demonstrated numerically. The coupler is fabricated and tested to confirm the analytical results. Fourth, we present a novel design, analysis, and fabrication of an ultracompact coupler and a 1 × 2 splitter based on plasmonic waveguides. In addition, we present two nano-scale plasmonic devices: a directional coupler and a Mach-Zehnder interferometer. The devices are embedded between two dielectric waveguides. Our simulation results show a coupling efficiency of 88% for the coupler, 45% for each splitter's branch, 37% for a 2 × 2 directional coupler switch, and above 50% for the proposed designs of the Mach-Zehnder interferometer. In order to confirm the analytical results, the plasmonic air-slot coupler and splitter are fabricated and tested.

Abstract Approval: Committee Chair _____

Program Director _____

Dean KGCOE _____

# ACKNOWLEDGMENTS

I am immensely grateful to God for providing me with the knowledge, health, strength, and patience that have made the completion of this endeavor possible.

I would like to express my deepest gratitude to my advisor Dr. Mustafa Abushagur for his continuous support and guidance throughout my studies. Dr. Abushagur, thank you for challenging me to come up with new ideas, to do groundbreaking science, and to write rigorous research papers. Despite the fact that I took a three-year leave, you always showed support and encouragement, for which I will always be thankful.

I would also like to express my deepest gratitude to my doctoral committee members for their feedback and support. Dr. Zhaolin Lu, thank you for being available to help even late into the evening. Dr. Stefan Preble and Dr. Thomas Smith, thank you both for your support.

I dedicate this dissertation to my parents Abdullah Wahsheh and Asmahan Fraihat. You are the ones who encouraged me to pursue my Ph.D. degree. My achievements would not have been possible without your support and prayers. Thank you for your guidance that has helped me fulfill my dreams and bring happiness into my life. My brothers Dr. Luay Wahsheh, Dr. Moayad Wahsheh, and Dr. Waseem Wahsheh, thank you all for being available when I needed you and thank you for your continuous support and advice throughout my academic journey.

Other members of my family have contributed to this dissertation in very special ways. This work would not have been possible without the support of my wife Tasneem Al-Hamdan and daughters Raneem and Ranci Wahsheh. Thank you for your tremendous patience and all the support you have given me throughout my years of doctoral study. My dear wife, I know how difficult it was to raise two children without having support from extended family. I hope that I will be able to make it up to you in the years to come.

I would like to acknowledge the support of: AlHaj Zuhair Al-Hamdan, my aunt Muneera Fraihat, and my cousins Dr. Qusai Al-Hamdan, Dr. Ashraf Al-Hamdan, Dr. Mohammed Al-Hamdan, Basel Al-Hamdan, Baha Al-Hamdan, Dr. Osama Al-Hamdan, Rabee Al-Hamdan, and Eman Al-Hamdan. Many thanks to Marouf Rababa, Ezdihar Al-Hamdan, and their children Diala, Mohammed, and Dana Rababa for their support.

# Table of Contents

# List of Figures

# List of Tables

# Chapter 1

# Introduction

Optical fiber interconnects and optical integrated circuits (OICs) are replacing their electrical counterparts mainly due to their low transmission losses, small size, large bandwidth, and high speed. Silicon-on-insulator (SOI) technology is used in the fabrication of both the optical and electrical integrated circuits, which makes it possible for future miniaturization of optoelectronic components and integration on the same chip. A class of photonic waveguides that have been widely used is based on SOI. The main source of losses in the SOI waveguides is from the sidewall roughness which can be reduced by oxidation smoothing and anisotropic etching methods [1]. Other sources involve coupling light into and out of the OIC as well as connecting different types of waveguides on the same chip. Mode correction is needed when coupling light between two waveguides that have different mode profiles. The mismatch in the mode profile causes radiation and back reflection losses. This problem is considered one of the main obstacles that prevents the multiple applications of the optical integrated circuits. The

future of dense optical integrated circuits requires the use of hybrid waveguides. Three main types of waveguides are used in OICs: conventional optical waveguides, photonic crystal (PC) waveguides, and plasmonic waveguides. The first guides light by total internal reflection, while the second by Bragg reflection, and the third by surface plasmon polariton. Integrating and connecting these waveguides, which usually have different geometries and propagation mechanisms, is needed to build efficient optical integrated circuits. Butt coupling is not the optimum solution to achieve high coupling efficiency due to the existence of mode mismatch [2]. The interface between these waveguides should be designed to achieve high power transmission. Therefore, the proposed methods in the literature aim to match the mode profile in each waveguide so that high coupling efficiency is achieved.

One way that is widely used to achieve modal conversion is by using a taper to change the mode size adiabatically [3-10]. The key point is to change the waveguide dimensions so that the mode size matches that of the input or output waveguide. Theoretically, as the taper length goes to infinity, all modes couple to the fundamental mode. Practically, taper lengths are finite and in turn total coupling cannot be achieved. To achieve high coupling efficiency, the light beam inside the tapered waveguide should be perturbed by means other than the linear geometry of the tapered waveguide. Sanchis *et al.* [10] used both a PC tapered waveguide and two extra defects at the interface between a dielectric and a PC waveguide. They achieved over 80% coupling efficiency. We advanced their work by using a nonlinear tapered waveguide and extra defects [11-14]. We achieved 96% coupling efficiency by changing the size and position of the inner taper rods.

Tapered waveguides are also used to couple light between dielectric waveguides and plasmonic waveguides [15-17]. Veronis and Fan [17] achieved 93% coupling efficiency between a silicon waveguide and a silver-air-silver plasmonic waveguide. Their proposed taper is long (400 nm) and its design requires the use of special software. We designed a compact taper of a length of 33 nm and achieved 90% coupling efficiency [18]. Then we designed different optical devices [19-22]: splitters, directional couplers, and Mach-Zehnder interferometers. To the best of our knowledge, this is the first time that one reports optical devices that couples light from dielectric waveguides into plasmonic waveguides. We fabricated and tested the proposed coupler and splitter to confirm the analytical results.

Coupling light from one waveguide into another can be achieved by placing them close to each other so that the evanescent tail of the mode in one waveguide overlaps with that in the adjacent waveguide [23-29]. The two coupled waveguides can be placed next to each other or on top of each other with an isolation layer in between. Due to the mode overlap, light couples from one waveguide into the adjacent one. Total beam switching occurs when phase matching occurs between the two modes over a specific interaction length. Lu [29] applied the vertical coupling method to couple light from a single mode fiber into an SOI waveguide. First, light is coupled from a single mode fiber into a dielectric waveguide that is terminated by a ring (top layer). Then, the circulated light in the ring performs many attempts to couple light into the SOI waveguide. Coupling occurs when the refractive index of the microring is slightly larger than the effective refractive index of the SOI waveguide. This requires using different dielectric material than that used in SOI. To simplify the fabrication process, we designed a microring coupler that has the

same material as that of the SOI waveguide [30]. The coupling occurs when the incident angle of the microring mode matches that of the SOI mode. The theoretical coupling efficiency is 91%. We fabricated the proposed microring coupler and experimentally demonstrated its operation.

Another way to couple light between waveguides is by using a resonant coupler [31-34]. The disadvantage of this coupler is that the increase in the coupling efficiency is only going to be within the resonance linewidth. Johnson *et al.* [31] proposed a resonant cavity that supports two orthogonal modes at the intersection area of two line-defect waveguides in a two dimensional (2D) square lattice PC structure. Their proposed design cannot be experimentally realized because there is no out-of-plane confinement. We proposed transverse magnetic (TM) and transverse electric (TE) PC devices that achieve crosstalk reduction for telecom wavelengths [35-39]. The former one consists of silicon pillars in oxide and the latter one consists of air-holes in silicon. The proposed TM devices achieved crosstalk reduction lower than those reported in the literature. We fabricated the proposed TE devices and experimentally achieved low crosstalk reduction as small as -20 dB.

Although many methods were proposed to increase the coupling efficiency between a single mode fiber and a dielectric waveguide as well as between a dielectric waveguide and both a photonic crystal and a plasmonic waveguide, further development on increasing the coupling efficiency and simplifying the fabrication process is still needed. The goal of this dissertation is to introduce efficient and compact couplers at the interface between the waveguides under investigation that can increase the coupling efficiency much more than those reported in the literature. We used tapered waveguides, vertical

couplers, and resonant couplers to achieve our goals. The second goal is to fabricate some of the proposed couplers and experimentally demonstrate that the proposed couplers achieve high coupling efficiency. The third goal is to demonstrate potential applications of the proposed plasmonic coupler in designing very short nanoplasmonic devices: splitters, directional couplers, and Mach-Zehnder interferometers.

This dissertation is divided into several chapters.

In **Chapter 2**, the concepts of operation of the conventional optical waveguides, photonic crystal waveguides, and plasmonic waveguides are discussed. Also, coupling light from one waveguide into another is explained using the coupled mode theory.

Efficient coupling between dielectric waveguides and PC waveguides is of great significance. In **Chapter 3**, different devices were presented for a planar PC tapered waveguide to enhance the coupling between a dielectric waveguide and a PC. The proposed couplers are based on changing both the size and position of the inner taper rods before and after adding extra defects. We show the design steps and the numerical results associated with each step.

A method to achieve ultra-low crosstalk in crossed strip waveguides using a PC cavity is reported in **Chapter 4.** We design, fabricate, and experimentally demonstrate TM and TE devices for telecom wavelengths. We propose two intersecting waveguides formed in a square lattice PC structure. One supports TM modes (i.e., silicon pillars in oxide) and the other supports TE modes (i.e., air-holes in silicon). Both structures provide index guiding and confinement in the vertical direction. By doing so, the size of the device can be dramatically reduced and ultra-low crosstalk can be realized. These two structures are practical for applications with index guiding applied in the out-of-plane direction. Our

simulation results show that our proposed TM device resulted in crosstalk reduction lower than that reported in literature. We have fabricated several different variations of the devices where the waveguides are separated by a different number of rods or air-holes to improve the coupling efficiency and reduce the crosstalk.

In **Chapter 5**, we present the design, fabrication, and experimental demonstration of a vertical microring coupler to couple light from a single mode fiber into an SOI waveguide. To simplify the fabrication process of the proposed microring coupler introduced by Lu [29], we propose another design for the coupler by using silicon as the fabrication material for the microring which matches the material used in the SOI waveguide. High coupling efficiency is achieved by controlling the incident angle of the light beam into the vertical microring coupler.

In **Chapter 6**, we propose a direct yet efficient short plasmonic coupler of a length of 33 nm to increase the coupling efficiency between an optical waveguide and a silver-air-silver plasmonic waveguide. Based on this coupler, we also propose a splitter that delivers light from a silicon waveguide into two plasmonic waveguides. To the best of our knowledge, this is the first time a 1 × 2 splitter from a silicon waveguide into two metal-dielectric-metal plasmonic waveguides is introduced. The fabrication procedure and the experimental results for the proposed coupler and splitter are shown. Two potential applications of the proposed coupler and splitter in directional couplers and Mach-Zehnder interferometers are also demonstrated. We also show other benefits of using the proposed coupler in improving the alignment tolerance of the plasmonic waveguide with respect to the dielectric waveguide and broadening the spectrum response of the splitter.

In **Chapter 7**, we describe the fabrication processes that were used for each fabricated device in this dissertation. The fabrication is made using SOI wafers. The fabrication process includes electron-beam lithography, dry and wet etching, dicing, and polishing. The fabrication processes are optimized by performing a dose test to find out the required dose to fabricate the desired devices. The results of the dose tests are presented for each fabricated device.

In **Chapter 8**, we summarize our research findings and propose directions for future work.

Our research work resulted in 15 publications [11-14,18-22,30,35-39]. We provide a copy of three publications [39,21,22] in Appendix A, B, and C, respectively.

## References


[1] K. K. Lee, D. R. Lim, L. C. Kimerling, J. Shin, and F. Cerrina, "Fabrication of ultralow-loss Si/SiO2 waveguides by roughness reduction," Optics Letters, vol. 26, December 2001, pp. 1888-1890.

[2] R. G. Hunsperger, *Integrated Optics: Theory and Technology*. Berlin; New York: Springer-Verlag, 2002, ch. 7.

[3] A. Mekis and J. D. Joannopoulos, "Tapered couplers for efficient interfacing between dielectric and photonic crystal waveguides," Journal of Lightwave Technology, vol. 19, June 2001, pp. 861-865.

[4] M. Banaee, A.G. Pattantyus-Abraham, and M.W. McCutcheon, "Efficient coupling of photonic crystal microcavity modes to a ridge waveguide," Applied Physics Letters, vol. 90, May 2007, pp. 193106.1-193106.3.

[5] A. Talneau, Ph. Lalanne, M. Agio, and C. M. Soukoulis, “Low-reflection photonic-crystal taper for efficient coupling between guide sections of arbitrary widths,” Optics Letters, vol. 27, September 2002, pp. 1522-1524.

[6] T. D. Happ, M. Kamp, and A. Forchel, “Photonic crystal tapers for ultracompact mode conversion,” Optics Letters, vol. 26, July 2001, pp. 1102-1104.

[7] P. Sanchis, J. Marti, A. Garcia, A. Martinez, and J. Blasco, “High efficiency coupling technique for planar photonic crystal waveguides,” Electronics Letters, vol. 38, August 2002, pp. 961-962.

[8] E. H. Khoo, A. Q. Liu, and J. H. Wu, “Nonuniform photonic crystal taper for high-efficiency mode coupling,” Optics Express, vol. 13, October 2005, pp. 7748-7759.

[9] S. Mittal and J. Sabarinathan, “Optimization of coupling and transmission through finite height SOI photonic crystal slab waveguides,” Proceedings of SPIE - The International Society for Optical Engineering, vol. 5971, October 2005, pp. 59711J.1-59711J.8.

[10] P. Sanchis, J. Marti, J. Blasco, A. Martinez, and A. Garcia, “Mode matching technique for highly efficient coupling between dielectric waveguides and planar photonic crystal circuits,” Optics Express, vol. 10, December 2002, pp. 1391-1397.

[11] M. A. G. Abushagur and R. A. Wahsheh, “Highly efficient optical coupler using hybrid photonic crystal structures,” Proceedings of SPIE - The International Society for Optical Engineering, vol. 5510, October 2004, pp. 68-70.

[12] M. A. G. Abushagur and R. A. Wahsheh, “Radii changing effect on the coupling efficiency between a silica waveguide and a planar photonic crystal,” Proceedings of

SPIE - The International Society for Optical Engineering, vol. 5510, October 2004, pp. 71-77.

[13] R. A. Wahsheh and M. A. G. Abushagur, “The effect of changing the position of the inner taper crystals on the coupling efficiency between a silica waveguide and a planar photonic crystal,” International Symposium on High Capacity Optical Networks and Enabling Technologies, HONET, November 2007, pp. 1-5.

[14] R. A. Wahsheh and M. A. G. Abushagur, “Compact and ultra-low-loss planar photonic crystal taper,” Microwave and Optical Technology Letters, vol. 52, March 2010, pp. 1454-1459.

[15] D. F. P. Pile and D. K. Gramotnev, “Adiabatic and nonadiabatic nanofocusing of plasmons by tapered gap plasmon waveguides,” Applied Physics Letters, vol. 89, July 2006, pp. 041111.1-041111.3.

[16] P. Ginzburg, D. Arbel, and M. Orenstein, “Gap plasmon polariton structure for very efficient microscale-to-nanoscale interfacing,” Optics Express, vol. 31, November 2006, pp. 3288-3290.

[17] G. Veronis and S. Fan, “Theoretical investigation of compact couplers between dielectric slab waveguides and two-dimensional metal-dielectric-metal plasmonic waveguides,” Optics Express, vol. 15, February 2007, pp. 1211-1221.

[18] R. A. Wahsheh, Z. Lu, and M. A. G. Abushagur, “Efficient couplers and splitters from dielectric waveguides to plasmonic waveguides”, in Frontiers in Optics, OSA Technical Digest (CD) (Optical Society of America), October 2008, pp. FThS4. http://www.opticsinfobase.org/abstract.cfm?URI=FiO-2008-FThS4

[19] R. A. Wahsheh, Z. Lu, and M. A. G. Abushagur, “Ultra-compact nanoplasmonic splitter,” International Symposium on High Capacity Optical Networks and Enabling Technologies, HONET, December 2009, pp. 179-181.

[20] R. A. Wahsheh, Z. Lu, and M. A. G. Abushagur, “Compact Nanoplasmonic Mach-Zehnder Interferometers,” International Symposium on High Capacity Optical Networks and Enabling Technologies, HONET, December 2009, pp. 182-183.

[21] R. A. Wahsheh, Z. Lu, and M. A. G. Abushagur, “Nanoplasmonic couplers and splitters,” Optics Express, vol. 17, October 2009, pp. 19033-19040.

[22] R. A. Wahsheh, Z. Lu, and M. A. G. Abushagur, “Nanoplasmonic Directional Couplers and Mach-Zehnder Interferometers,” Optics Communications, vol. 282, September 2009, pp. 4622-4626.

[23] R. G. Hunsperger, *Integrated Optics: Theory and Technology*. Berlin; New York: Springer-Verlag, 2002, ch. 8.

[24] V. R. Almeida, R. R. Panepucci, and M. Lipson, “Nanotaper for compact mode conversion,” Optics Letters, vol. 28, August 2003, pp. 1302-1304.

[25] L. Vivien, S. Laval, E. Cassan, X. L. Roux, and D. Pascal, “2-D taper for low-loss coupling between polarization-insensitive microwaveguides and single-mode optical fibers,” Journal of Lightwave Technology, vol. 21, October 2003, pp. 1-5.

[26] D. W. Prather, J. Murakowski, S. Shi, S. Venkataraman, A. Sharkawy, C. Chen, and D. Pustai, “High-efficiency coupling structure for a single-line-defect photonic-crystal waveguide,” Optics Letters, vol. 27, September 2002, pp. 1601-1603.

[27] D. Taillaert, W. Bogaerts, P. Bienstman, T. F. Krauss, P. Van Daele, I. Moerman, S. Verstuyft, K. De Mesel, R. Baets “An out-of-plane grating coupler for efficient

butt-coupling between compact planar waveguides and single-mode fibers," IEEE Journal of Quantum Electronics, vol. 38, July 2002, pp. 949-955.

[28] Z. Lu, D. W. Prather, "Total internal reflection-evanescent coupler for fiber-to-waveguide integration of planar optoelectric devices," Optics Letters, vol. 29, August 2004, pp. 1748-1750.

[29] Z. Lu, "Efficient fiber-to-waveguide coupling through the vertical leakage from a microring," Optics Letters, vol. 32, October 2007, pp. 2861-2863.

[30] R. A. Wahsheh, Z. Lu, Jun Yang, and M. A. G. Abushagur, "Silicon microring vertical coupler," International Symposium on High Capacity Optical Networks and Enabling Technologies, HONET, December 2009, pp. 280-283.

[31] S. G. Johnson, C. Manolatou, S. Fan, P. R. Villeneuve, J. D. Joannopoulos, and H. A. Haus, "Elimination of cross talk in waveguide intersections," Optics Letters, vol. 23, December 1998, pp. 1855-1857.

[32] T. Liu, M. Fallahi, M. Mansuripur, A. R. Zakharian, and J. V. Moloney, "Intersection of nonidentical optical waveguides based on photonic crystals," Optics Letters, vol. 30, September 2005, pp. 2409-2411.

[33] Y. G. Roh, S. Yoon, H. Jeon, S. H. Han, and Q. H. Park, "Experimental verification of cross talk reduction in photonic crystal waveguide crossings," Applied Physics Letters, vol. 85, October 2004, pp. 3351-3353.

[34] S. H. G. Teo, A. Q. Liu, J. B. Zhang, and M. H. Hong, "Induced free carrier modulation of photonic crystal optical intersection via localized optical absorption effect," Applied Physics Letters, vol. 89, August 2006, pp. 091910.1-091910.3.

[35] R. A. Wahsheh, M. A. G. Abushagur, and Z. Lu, “A method for cross talk reduction in crossed strip waveguides,” International Symposium on High Capacity Optical Networks and Enabling Technologies, HONET, November 2007, pp. 1-4.

[36] R. A. Wahsheh, M. A. G. Abushagur, Z. Lu, and S. F. Preble, “Cross talk reduction of nanophotonic crossed waveguides using a resonant cavity,” International Nanotechnology Conference, Jeddah, Saudi Arabia, November 2008.

[37] R. A. Wahsheh, Z. Lu, M. A. G. Abushagur, and S. F. Preble, “Ultra low cross talk in crossed strip waveguides with the assistance of a photonic crystal cavity,” Proceedings of SPIE - The International Society for Optical Engineering, vol. 7056, August 2008, pp. 70560E.1-70560E.8.

[38] R. A. Wahsheh, Z. Lu, S. F. Preble, and M. A. Abushagur, "Cross talk reduction by photonic crystal cavities", in Frontiers in Optics, OSA Technical Digest (CD) (Optical Society of America), October 2008, pp. FThK3.
http://www.opticsinfobase.org/abstract.cfm?URI=FiO-2008-FThK3

[39] R. A. Wahsheh, Z. Lu, and M. A. G. Abushagur, “Cross talk reduction in square cavities,” IEEE Photonics Journal, vol. 1, September 2009, pp. 191-196.

# Chapter 2

# Background Concepts

In this chapter, we discuss the concepts of operation of three types of waveguides that are relevant to this dissertation. These waveguides are: conventional optical waveguides, photonic crystal waveguides, and plasmonic waveguides. We also discuss mode coupling between waveguides using the coupled mode theory.

## 2.1 Types of Optical Waveguides

Different optical waveguides have been proposed to achieve compact optical integrated circuits. The three main types of waveguides are: conventional optical waveguides, photonic crystal waveguides, and plasmonic waveguides. The physics of operations and the properties of guiding light in each type are different. Interfacing these waveguides to other optical devices, such as light sources, detectors, and optical fibers requires optical couplers. Couplers are very critical in order to transfer optical power with high efficiency and low loss between different types of waveguides and other photonic devices.

To achieve that, one should understand the principle of operation in each type of waveguide. Herein, the basic physics of how light is guided in these waveguides will be explained.

### 2.1.1 Conventional Optical Waveguides (Slab Waveguides)

A slab waveguide is the most fundamental guiding device. It is made of a core that is surrounded by a material, called cladding, which has a lower refractive index than that of the core. Two methods are used to describe the modes inside a slab waveguide: one is the ray optic method and the other is the physical or wave optic method [1]. Based on the ray optic method, slab waveguides guide light by total internal reflection. To achieve that, the incident angle, $\theta_{incident}$, should be larger than a critical angle. As shown in Figure 2.1, the refractive index of silicon should be greater than that of the substrate and cladding (i.e., $n_{silicon} > n_{substrate} > n_{cladding}$). The critical angle at the silicon interface with the cladding is given by $\theta_{cladding} = sin^{-1}(n_{cladding}/n_{silicon})$ and that with the substrate is given by $\theta_{substrate} = sin^{-1}(n_{substrate}/n_{silicon})$. The latter angle is greater than the former one (i.e., $\theta_{substrate} > \theta_{cladding}$) because the refractive index of the substrate is greater than that of the cladding. A waveguide can support three types of modes based on $\theta_{incident}$. A guided mode occurs when $\theta_{substrate} < \theta_{incident} < 90^o$ (as shown in Figure 2.1(a)), whereas, a leaky mode into the substrate occurs when $\theta_{cladding} < \theta_{incident} < \theta_{substrate}$ (as shown in Figure 2.1(b)). Another leaky mode into both the substrate and cladding occurs when $\theta_{incident} < \theta_{cladding}$ (as shown in Figure 2.1(c)).

Not all incident angles given by $\theta_{substrate} < \theta_{incident} < 90^o$ are guided modes. Only discrete values of $\theta_{incident}$ can be guided. The smaller the incident angle, the higher the mode order and the larger the evanescent tail. The fundamental mode is the mode that

occurs when $\theta_{incident} = 90^o$. All guided modes are orthogonal to each other. Mode coupling may occur in the case of surface perturbations.

Based on the physical optic method, the modes supported by a slab waveguide should satisfy both Maxwell's equations and the boundary conditions at each interface with the guided layer. The propagation constant of the supported mode is as shown in Figure 2.2. The propagation constants in the $x$ and $z$ directions are given by $k_x = k_{mode}\, cos\theta_{incident}$ and $k_z = k_{mode}\, sin\theta_{incident}$, respectively, where $k_{mode} = k_o n_{silicon}$ and $k_o = 2\pi/\lambda_o$.

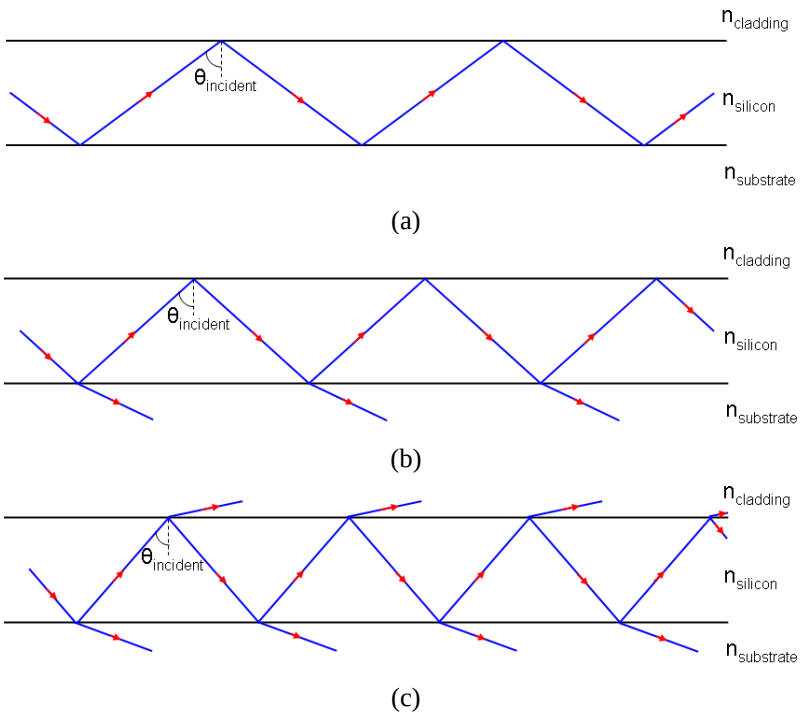


Figure 2.1: Types of modes supported by a slab waveguide based on the ray-optic approach: (a) guided mode in silicon, (b) radiation mode in substrate, and (c) radiation mode in both the substrate and cladding [1].

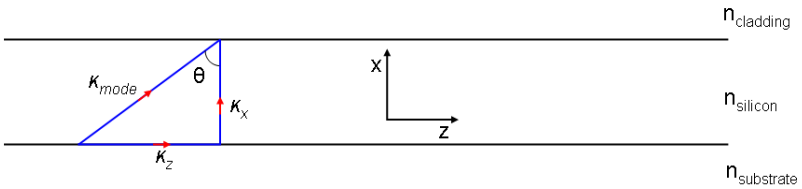


Figure 2.2: Propagation constant of the supported mode.

Maxwell's equations in a linear, isotropic, source and charge free, frequency independent, and lossless periodic dielectric medium can be written as:

$$\nabla.\vec{D}(\vec{r},t)=0 \tag{2.1}$$

$$\nabla.\vec{B}(\vec{r},t)=0 \tag{2.2}$$

$$\nabla\times\vec{E}(\vec{r},t)=-\frac{1}{c}\frac{\partial\vec{B}(\vec{r},t)}{\partial t} \tag{2.3}$$

$$\nabla\times\vec{H}(\vec{r},t)=\frac{1}{c}\frac{\partial\vec{D}(\vec{r},t)}{\partial t}. \tag{2.4}$$

Solving Maxwell's equations by the frequency domain method requires expanding the fields into harmonic modes to cancel out the time dependence.

$$\vec{E}(\vec{r},t)=\vec{E}(\vec{r})e^{jwt} \tag{2.5}$$

$$\vec{H}(\vec{r},t)=\vec{H}(\vec{r})e^{jwt}. \tag{2.6}$$

The wave equation of the electric and magnetic fields are given by

$$\nabla^2\vec{E}(\vec{r},t)=\frac{n^2(\vec{r})}{c^2}\frac{\partial^2\vec{E}(\vec{r},t)}{\partial t^2} \text{ and } \nabla^2\vec{H}(\vec{r},t)=\frac{n^2(\vec{r})}{c^2}\frac{\partial^2\vec{H}(\vec{r},t)}{\partial t^2}. \tag{2.7}$$

Substituting Eqs. (2.5) and (2.6) we obtain

$$\nabla^2\vec{E}(\vec{r})+k_o^2n^2(\vec{r})\vec{E}(\vec{r})=0 \text{ and } \nabla^2\vec{H}(\vec{r})+k_o^2n^2(\vec{r})\vec{H}(\vec{r})=0. \tag{2.8}$$

The electric and magnetic fields of a plane wave propagating in the *z*-direction (as shown in Figure 2.2) are given by

$$\vec{E}(\vec{r})=E(x,y)e^{-j\beta z} \text{ and } \vec{H}(\vec{r})=H(x,y)e^{-j\beta z}. \tag{2.9}$$

The slab waveguide supports two orthogonal modes that are independent of the y-direction. One is called the transverse electric (TE) mode and the other is called the transverse magnetic (TM) mode. The TE mode equations are described by

$$\frac{\partial^2 E_y}{\partial x^2} + (k_o^2 n^2 - \beta^2) E_y = 0 \tag{2.10}$$

$$H_x = \frac{-\beta}{\omega \mu_o} E_y$$
$$H_z = \frac{-1}{j\omega \mu_o} \frac{\partial E_y}{\partial x} \quad , \tag{2.11}$$

where the refractive index, $n$, is not as a function of position. The same kind of equations can be written for the TM mode by replacing $E_y$, $H_x$, $H_z$, and $\mu_o$ by $H_y$, $E_x$, $E_z$, and $\varepsilon_o$, respectively.

The field distribution of the supported modes by the waveguide can be found by solving Eq. (2.10) at each boundary with the guiding layer. The transverse electric $E_y$ at each boundary is given by

$$\begin{aligned}
&\text{Cladding:} && E_y = A\exp(-\varphi_{cladding} x), && 0 \le x \le \infty \\
&\text{Core of thickness (T):} && E_y = B\cos(\varphi_{silicon} x + \Phi), && -T \le x \le 0 \\
&\text{Substrate:} && E_y = C\exp[\varphi_{substrate}(x+T)], && -\infty \le x \le -T \quad ,
\end{aligned} \tag{2.12}$$

where $\varphi_{cladding} = k_o \sqrt{n_{silicon}^2 \sin^2 \theta_{incident} - n^2{}_{cladding}}$ , $\varphi_{silicon} = k_o \sqrt{n_{silicon}^2 - n_{silicon}^2 \sin^2 \theta_{incident}}$ ,

$\varphi_{substrate} = k_o \sqrt{n_{silicon}^2 \sin^2 \theta_{incident} - n^2{}_{substrate}}$ , $\Phi = \tan^{-1} \frac{\varphi_{cladding}}{\varphi_{silicon}}$ , $A = B\cos\Phi$ , and $C = B\cos(\varphi_{silicon} T - \Phi)$

Solving the above equations for $\varphi_{silicon} T$ , results in the eigenvalue equation $\varphi_{silicon} T = (n+1)\pi - \tan^{-1}(\frac{\varphi_{silicon}}{\varphi_{substrate}}) - \tan^{-1}(\frac{\varphi_{silicon}}{\varphi_{cladding}})$, where $n$ is an integer number that denotes the mode number.

The electric field distribution of $E_y$ is as shown in Figure 2.3.

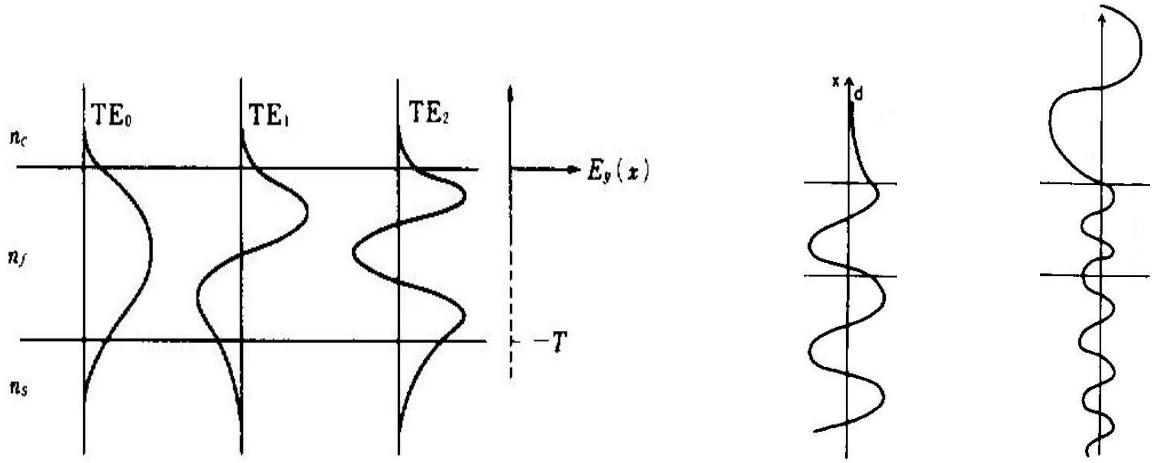


Figure 2.3: Types of modes supported by a slab waveguide based on the physical-optic approach: (a) guided mode, (b) radiation mode in substrate, and (c) radiation mode in both the substrate and cladding [1].

The decay rate inside the cladding is given by $\varphi_{cladding} = k_o \sqrt{n^2_{silicon} \sin^2 \theta_{incident} - n^2_{cladding}}$ . When the effective refractive index of the mode approaches the refractive index of the cladding by reducing the size of the core ( $N_{eff} = n^2_{silicon} \sin^2 \theta_{incident} \rightarrow n^2_{cladding}$ ), the decay rate $\varphi_{cladding}$ approaches zero. The closer the decay rate to zero, the larger the mode size [2,3]. The minimum mode size is limited by the diffraction limit ($\lambda_o/2n_{silicon}$).

### 2.1.2 Photonic Crystal Waveguides

The field of guiding and controlling light has been enhanced since the invention of the photonic crystals (PCs) [4]. A PC is defined as an artificial engineered periodic structure in one, two, or three dimensions of at least two different materials with a suitable refractive index contrast. Unlike the dielectric waveguides that guide light by total internal reflection, a PC guides light by trapping and localizing it. The light waves with a certain range of frequencies cannot propagate through a PC structure due to the distributed Bragg

reflection from the bulk crystals. This aforementioned range of frequencies is called photonic band gap (PBG). The width of the PBG depends on the refractive index contrast in addition to the lattice geometry and filling factor of the highest refractive index. The higher the refractive contrast, the wider the PBG. The two widely used lattice geometries are the square and triangular geometries. The latter one has a wider PBG than the former one. PBG can support TE, TM, or both depending on the filling factor. Figure 2.4 shows TE (i.e., air-holes in silicon) and TM (i.e., silicon pillars in air) PC structures. The high refractive index material is connected in the TE PC structure and disconnected in the TM PC structure.

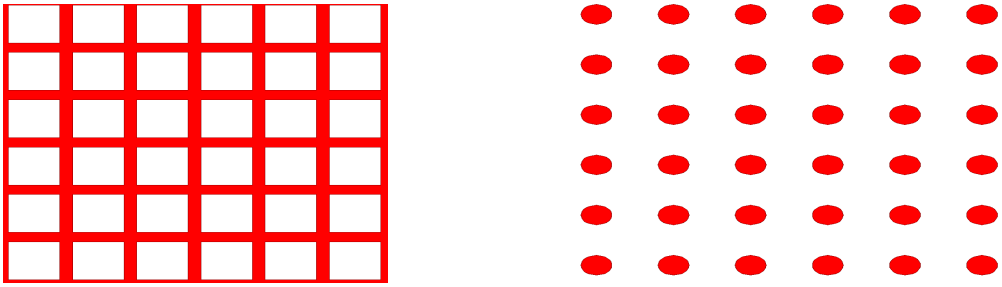

(a) (b)

Figure 2.4: A photonic crystal structure that supports (a) transverse electric mode and (b) transverse magnetic mode.

Taking the curl of Eq. (2.4) after dividing it by $\varepsilon(\vec{r})$ and substituting Eq. (2.3) gives the wave equation of the magnetic field [5,6],

$$\nabla\times[\frac{1}{\varepsilon(\vec{r})}\nabla\times\vec{H}(\vec{r})]=(\frac{w}{c})^2\vec{H}(\vec{r}). \tag{2.13}$$

Equation (2.13) can be written as an eigenvalue problem

$$\Theta\vec{H}(\vec{r})=(\frac{w}{c})^2\vec{H}(\vec{r}), \tag{2.14}$$

where $\Theta$ is a Hermitian differential operator and $(\omega/c)^2$ is the eigenvalue. According to the Bloch-Floquet theorem [5,6], the solution of this equation is of the

form $\vec{H}(\vec{r}) = H_{n,\vec{k}}(\vec{r}) = \vec{v}_{n,\vec{k}}(\vec{r})e^{j\vec{k}.\vec{r}}$ where $\vec{v}_{n,\vec{k}}(\vec{r}).\vec{k} = 0$ (i.e., transverse electromagnetic waves), $\vec{v}_{n,\vec{k}}(\vec{r})$ is a periodic function, *n* is the band index, and *k* is a wave vector in the first brillouin zone.

To find the electric field modes, $\vec{H}(\vec{r})$ is substituted in Eq. (2.15).

$$\vec{E}(\vec{r}) = (\frac{-jc}{w\varepsilon(\vec{r})})\nabla \times \vec{H}(\vec{r}). \tag{2.15}$$

Since $\varepsilon(\vec{r})$ and $H_{n,\vec{k}}(\vec{r})$ are periodic functions of $\vec{r}$, they can be expanded by using the Fourier series,

$$\frac{1}{\varepsilon(\vec{r})} = \sum_{\vec{G}} k(\vec{G}).e^{j\vec{G}.\vec{r}} \tag{2.16}$$

$$H_{n,\vec{k}}(\vec{r}) = \sum_{\vec{G}} H_{n,\vec{k}}(\vec{G}).e^{j(\vec{k}+\vec{G}).\vec{r}}, \tag{2.17}$$

where $\vec{G}$ is the reciprocal lattice vector. Substituting $H_{n,\vec{k}}(\vec{r})$ in the eigenvalue equation gives

$$-\sum_{\vec{G}'} k(\vec{G}-\vec{G}')(k+\vec{G})\times\{(k+\vec{G}')\times H_{n,\vec{k}}(\vec{G}')\} = \frac{w_{n,\vec{k}}^2}{c^2} H_{n,\vec{k}}(\vec{G}). \tag{2.18}$$

The PBG can be obtained by solving Eq. (2.18) by numerical methods. Figure 2.5 shows the PBG of a triangular-lattice PC structure of silicon pillars in oxide. The normalized frequency range of the PBG is between $0.267a/\lambda$ and $0.361a/\lambda$. It is almost centered at $\lambda_o = 1.55$ μm.

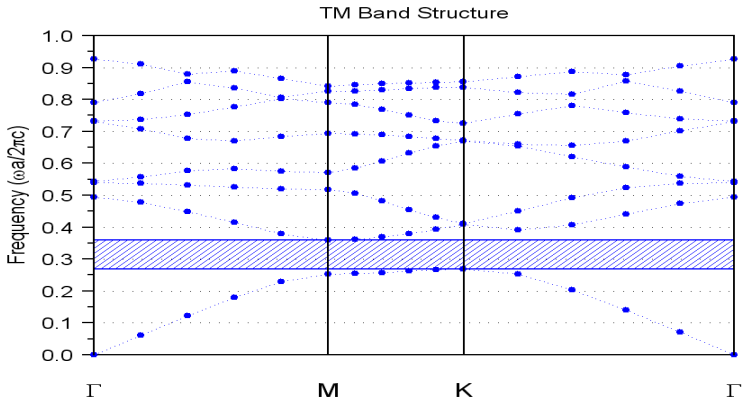


Figure 2.5: TM band structure of a triangular-lattice PC structure of silicon pillars in oxide.

Defects should be introduced in the PC structure to enable light waves with frequencies inside the PBG to propagate through the PC structure. A point defect can act as an electromagnetic cavity by either adding (as shown in Figure 2.6(a)) or removing dielectric material from a unit cell [7]. A line defect can act as a waveguide by either adding or removing dielectric material (as shown in Figure 2.6(b)) from a whole row or column from the crystal [8]. Another way to create a waveguide is by coupling light from one cavity into another adjacent one (as shown in Figure 2.6(c)). This kind of waveguide is called the coupled cavity waveguide (CCW) [9-11]. The mode in each cavity overlaps with the mode in the adjacent cavity so that mode coupling occurs. Changing the size, shape, and dielectric material or adding extra defects will change the dielectric constant of the unit cell by $\delta\varepsilon$ where $\varepsilon$ is a function of position only [12].

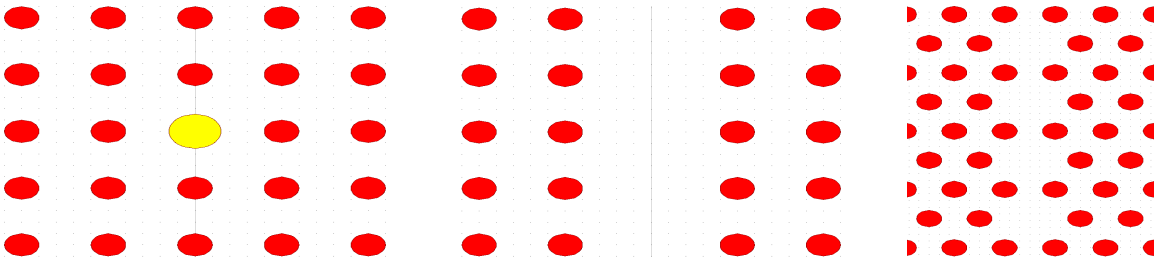


Figure 2.6: (a) Point defect acts as a cavity; (b) line defect acts as a waveguide; (c) series of cavities act as a waveguide (CCW).

A two-dimensional (2D) PC structure is much easier to fabricate than a three-dimensional (3D) structure. One method that is widely utilized to make a 2D PC structure act as a 3D structure is by using a slab PC structure [13]. The propagated light in the slab is localized in the in-plane direction by the distributed Bragg reflection and in the out-of-plane direction by the total internal reflection.

### 2.1.3 Plasmonic Waveguides

Surface plasmon polariton (SPP) occurs at the interface between metal and dielectric material due to the interaction between the free surface electrons with the incident photons (as shown in Figure 2.7(a)) [14]. This interaction results in oscillating the electron plasma. Gauss's law (i.e., $\nabla.\vec{E} = \rho/\varepsilon$) states that free electric charge, $\rho$, produces electric field, $E$. The interaction of electromagnetic field and free surface charges of a metal is given by the Drude model [15] as

$$\varepsilon_{metal} = 1 - \frac{w_p^2}{w(w + i\gamma)}, \tag{2.19}$$

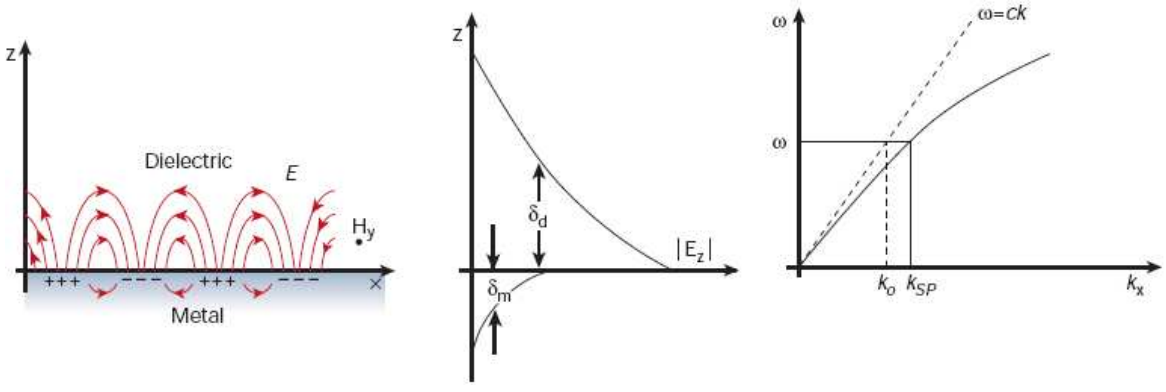


(a) (b) (c)

Figure 2.7: (a) Surface plasmon polariton at the interface between metal and dielectric; (b) field distribution at the interface; (c) dispersion curve [14].

where $w_p$ is the plasma frequency and $\gamma$ is the damping rate of electrons. When $w < w_{sp}$, light can propagate at the interface between metal and dielectric. This is called SPP wave. The excited SPP decays exponentially from the interface into both metal and dielectric regions. The decay length into the metal, $\delta_m$, is much shorter than that into the dielectric region, $\delta_d$, (see Figure 2.7(b)). This is because the real value of the permittivity of metal is negative and much smaller than the positive permittivity of the dielectric materials (i.e., $\Re(\varepsilon_{metal}) < 0 < \varepsilon_{dielectric}$). SPPs support only TM modes in which the magnetic field is perpendicular to the direction of propagation. The dispersion relation for the SPP (see Figure 2.7(c)) is given by

$$\beta = k_{sp} = \frac{w}{c}\sqrt{\frac{\varepsilon_{metal}\varepsilon_{dielectric}}{\varepsilon_{metal}+\varepsilon_{dielectric}}} = k_o\sqrt{\frac{n_{metal}n_{dielectric}}{n_{metal}+n_{dielectric}}}\,. \tag{2.20}$$

To confine light in the dielectric region, the dielectric region is put between two metals, as shown in Figure 2.8. The thickness of the metal needed to confine light in the dielectric region can be slightly larger than $\delta_m$. In this configuration, the decaying SPP mode at each dielectric-metal interface interacts with the other one, creating a confined light in the dielectric region. The dielectric width can be below the diffraction limit because as the dielectric width decreases the effective refractive index increases. Reducing the width of the dielectric region increases the mode confinement and decreases the propagation length [16,17]. The propagation length is decreased because as the mode confinement increases, the interaction with metal increases and consequently the losses increase. For example, the propagation length at a wavelength of 1.55 μm for the metal-dielectric-metal waveguide shown in Figure 2.8(a) is about 5 μm when the width of the dielectric region is equal to 50 nm and it increases to 10 μm when the width increases to 100 nm [16].

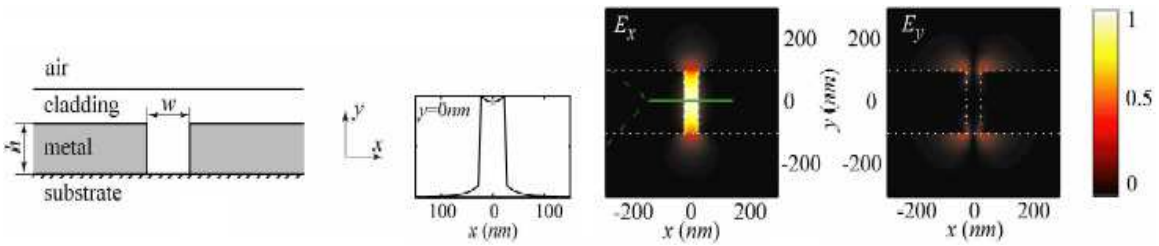


(a) (b) (c) (d)

Figure 2.8: Metal-dielectric-metal plasmonic waveguide (a) schematic diagram, (b) amplitude distribution of the fundamental mode, (c and d) power density profile of the coupled light [17].

Silver and gold are widely used in the fabrication of plasmonic waveguides. Silver has the highest electrical and thermal conductivity, highest optical reflectivity, and lowest contact resistance of any other metal [18]. On the other hand, gold is the most ductile metal which has good electrical and thermal conductivity [19]. Silver is cheaper and slightly harder than gold. Unlike gold, silver can easily oxidize.

## 2.2 Coupled Mode Theory

The coupled mode theory is used to explain how mode coupling occurs. Mode coupling may occur within the supported modes in an isolated waveguide by surface perturbations, or from one waveguide mode into another by placing them close to each other so that the evanescent tail of the mode in one waveguide overlaps with that in the adjacent waveguide, or by using a resonant cavity between waveguides. Herein, mode coupling between waveguides will be explained using the coupled mode theory.

### 2.2.1 Vertical and Side-by-Side Waveguide Couplers

To couple light from one waveguide into another, the waveguides are placed next to each other (see Figure 2.9(a)) or on top of each other with an isolation layer in between (see Figure 2.9(b)). Due to the mode overlap, light couples from one waveguide into the

adjacent one. Mode coupling is periodic between the two coupled waveguides. Total beam switching occurs when phase matching occurs between the two modes over a specific interaction length.

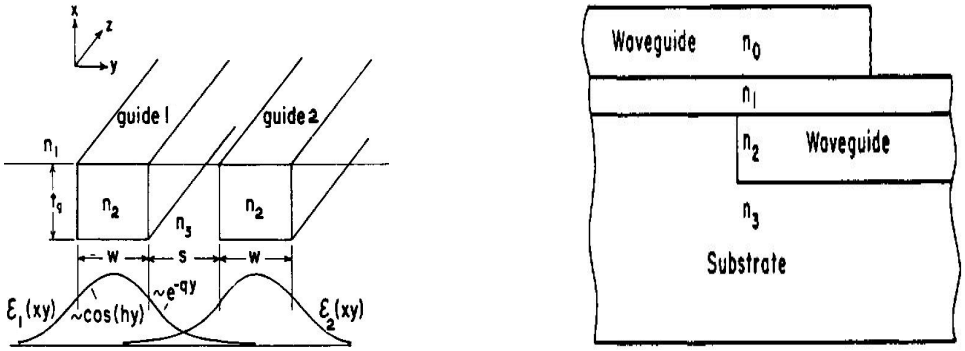


(a) (b)

Figure 2.9: Coupled waveguides geometries: (a) side-by-side coupling and (b) vertical coupling [20].

The coupled mode theory is used to describe the coupling between mode *A* in waveguide 1 and mode *B* in waveguide 2 [20,21]. The electric field of the supported mode in each waveguide without perturbation from the other waveguide can be written as

$$\begin{aligned} E_1(x,y,z,t) &= A(z)\exp[\,j(wt-\beta_1 z)]\mathrm{M}_1(x,y) \\ E_2(x,y,z,t) &= B(z)\exp[\,j(wt-\beta_2 z)]\mathrm{M}_2(x,y) \end{aligned}, \tag{2.21}$$

where *M* is the spatial field distribution in each standalone waveguide, and *A(z)* and *B(z)* are complex amplitudes. The propagation constants $\beta_1$ and $\beta_2$ in each waveguide are given by

$$\begin{aligned} \frac{dA(z)}{dz} &= -j\beta_1 A(z) + \kappa_{AB} B(z) \\ \frac{dB(z)}{dz} &= -j\beta_2 B(z) + \kappa_{BA} A(z) \end{aligned}, \tag{2.22}$$

where $\kappa_{AB}$ and $\kappa_{BA}$ are the coupling coefficients between the two modes. Since the coupling between *A* and *B* is the same ( $\kappa_{AB} = \kappa_{BA} = -j\kappa$ ), then Eq. (2.22) becomes

$$\begin{aligned} \frac{dA(z)}{dz} &= -j\beta_1 A(z) - j\kappa B(z) \\ \frac{dB(z)}{dz} &= -j\beta_2 B(z) - \kappa A(z) \end{aligned} . \tag{2.23}$$

In a directional coupler, light is excited in one waveguide. The boundary conditions when mode *A* is excited are

$$A(z=0)=1 \text{ and } B(z=0)=0 . \tag{2.24}$$

The expression for each mode when there is a propagation constant difference, $\Delta\beta$, between the two waveguides, is given by

$$\begin{aligned} A(z) &= (\cos\chi z - j\frac{\Delta\beta}{2\chi}\sin\chi z)\exp[-j(\beta_1 - \frac{\Delta\beta}{2})z] \\ B(z) &= j\frac{k}{\chi}\sin\chi z\exp[-j(\beta_2 + \frac{\Delta\beta}{2})z] \end{aligned} , \tag{2.25}$$

where $\chi = \sqrt{\kappa^2 + (\frac{\Delta\beta}{2})^2}$. The power transfer between the two waveguides taking into account the waveguide loss coefficient, $\alpha$, is demonstrated by

$$\begin{aligned} P_A(z) &= A(z)A^*(z) = [\cos^2(\chi z) + (\frac{\Delta\beta}{2})^2\frac{\sin^2(\chi z)}{\chi^2}]\exp-\alpha z \\ P_B(z) &= B(z)B^*(z) = \frac{k^2}{\chi^2}\sin^2(\chi z)\exp-\alpha z \end{aligned} . \tag{2.26}$$

The power transfer between two identical waveguides (see Figure 2.10) is given by

$$\begin{aligned} P_A(z) &= A(z)A^*(z) = \cos^2(\kappa z)\exp-\alpha z \\ P_B(z) &= B(z)B^*(z) = \sin^2(\kappa z)\exp-\alpha z \end{aligned} . \tag{2.27}$$

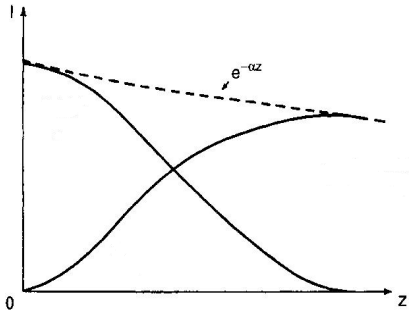


Figure 2.10: Power transfer in a directional coupler [20].

The interaction length, *L*, needed to transfer light from one waveguide into another is given by

$$L = \frac{\pi}{2\kappa} + \frac{n\pi}{\kappa}, \tag{2.28}$$

where *n* is an integer number that equals 0, 1, 2,…etc.

### 2.2.2 Resonant Couplers

Manolatou *et al*. [22] mathematically analyzed and explained (by using the coupled mode theory in time) the coupling of a four-port cavity that is connected to four waveguides (*W1*, *W2*, *W3* and *W4*) as shown in Figure 2.11. *Out* and *In* are the output and input waves of *W*, respectively. The cavity supports two modes: *X* and *Z*. The *X*-mode is excited from *W3* while the *Z*-mode is excited from *W1*. Crosstalk occurs when both the *X*- and *Z*-modes coexist. The two supported modes are given by

$$X = \frac{\sqrt{\frac{2}{\tau x_{W3}}}}{j(\omega-\omega_o)+\frac{1}{\tau x_{W1}}+\frac{1}{\tau x_{W2}}+\frac{1}{\tau x_{W3}}+\frac{1}{\tau x_{W4}}+\frac{1}{\tau x_{C0}}} Out1 \qquad Z = \frac{\sqrt{\frac{2}{\tau z_{W1}}}}{j(\omega-\omega_o)+\frac{1}{\tau z_{W1}}+\frac{1}{\tau z_{W2}}+\frac{1}{\tau z_{W3}}+\frac{1}{\tau z_{W4}}+\frac{1}{\tau z_{C0}}} Out1, \tag{2.29}$$

where $1/\tau_{W1,2,3,4}$ is the decay rate of the supported cavity mode into each waveguide, $1/\tau_{C0}$ is the decay rate of the cavity due to radiation losses, and $\omega_o$ is the resonant frequency. Since all waveguides are symmetric, then the decay rate of the two modes *X* and *Z* into each waveguide will be the same and equal to $1/\tau x$ and $1/\tau z$, respectively. For a lossless cavity (i.e., $1/\tau_{C0} = 0$), the two modes are given by

$$X = \frac{\sqrt{\frac{2}{\tau x}}}{j(\omega-\omega_o)+\frac{4}{\tau x}} Out1 \qquad Z = \frac{\sqrt{\frac{2}{\tau z}}}{j(\omega-\omega_o)+\frac{4}{\tau z}} Out1. \tag{2.30}$$

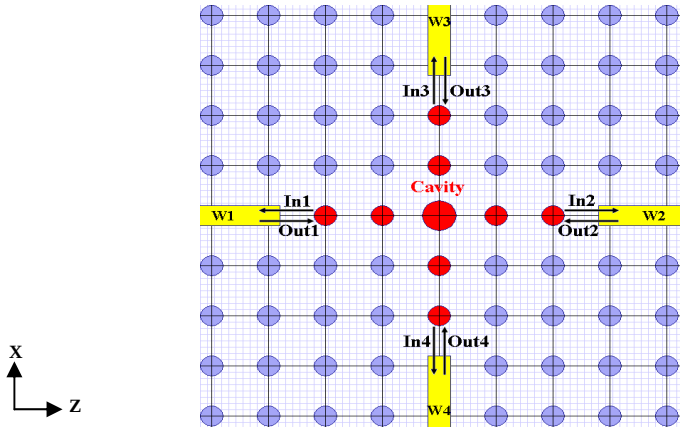


Figure 2.11: A four-port cavity connected to four waveguides.

If light is launched into *W1*, then the transmission into *W2* (denoted below as *T*), reflection into *W1* (denoted below as *R*), crosstalk into *W3* (denoted below as $X_U$), and crosstalk into *W4* (denoted below as $X_L$) at any frequency are as follows [22]:

$$\frac{In2}{Out1} \equiv T = \frac{\frac{2}{\tau x}}{j(\omega-\omega_o)+\frac{4}{\tau x}} + \frac{\frac{2}{\tau z}}{j(\omega-\omega_o)+\frac{4}{\tau z}} \tag{2.31}$$

$$\frac{In1}{Out1} \equiv R = -1+\frac{\frac{2}{\tau x}}{j(\omega-\omega_o)+\frac{4}{\tau x}} + \frac{\frac{2}{\tau z}}{j(\omega-\omega_o)+\frac{4}{\tau z}} \tag{2.32}$$

$$\frac{In3}{Out1} \equiv X_U = \frac{\frac{2}{\tau x}}{j(\omega-\omega_o)+\frac{4}{\tau x}} - \frac{\frac{2}{\tau z}}{j(\omega-\omega_o)+\frac{4}{\tau z}} \tag{2.33}$$

$$\frac{In4}{Out1} \equiv X_L = X_U \,. \tag{2.34}$$

For a lossless cavity and symmetric waveguides, total transmission with no crosstalk occurs when the operating frequency is at the resonance frequency of the cavity (i.e., $\omega = \omega_o$) and the two modes have the same decay rate into each waveguide (i.e., $\tau x = \tau z$). The disadvantage of the resonant couplers is that the increase in the coupling efficiency is only going to be over the resonance width.

## 2.3 Summary

In this chapter, we discussed the principle of operation of three optical waveguides that are relevant to our research work: the conventional optical waveguides, the photonic crystal waveguides, and the plasmonic waveguides. We also explained how mode coupling occurs between waveguides.

## References


[1] H. Nishihara, M. Haruna, and T. Suhara, *Optical Integrated Circuits*. New York: McGraw-Hill, 1989, ch. 2,3.

[2] L. Vivien, S. Laval, E. Cassan, X. L. Roux, and D. Pascal, "2-D taper for low-loss coupling between polarization-insensitive microwaveguides and single-mode optical fibers," Journal of Lightwave Technology, vol. 21, October 2003, pp. 1-5.

[3] V. R. Almeida, R. R. Panepucci, and M. Lipson, "Nanotaper for compact mode conversion," Optics Letters, vol. 28, August 2003, pp. 1302-1304.

[4] A. Mekis and J. D. Joannopoulos, "Tapered couplers for efficient interfacing between dielectric and photonic crystal waveguides," Journal of Lightwave Technology, vol. 19, June 2001, pp. 861-865.

[5] J. D. Joannopoulos, R. D. Meade, and J. N. Winn, Photonic Crystals: *Molding the Flow of Light*. Princeton, N.J.: Princeton University Press, 1995, ch. 2.

[6] K. Sakoda, *Optical Properties of Photonic Crystals* (Springer Verlang Berlin Heidelberg New York, 2001)

[7] S. Noda, A. Chutinan, and M. Imada, "Trapping and emission of photons by a single defect in a photonic bandgap structure," Nature, October 2000, vol. 407, pp. 608-610.

[8] D. W. Prather, J. Murakowski, S. Shi, S. Venkataraman, A. Sharkawy, C. Chen, and D. Pustai, “High-efficiency coupling structure for a single-line-defect photonic-crystal waveguide,” Optics Letters, vol. 27, September 2002, pp. 1601-1603.

[9] M. Bayindir, B. Temelkuran, and E. Ozbay, “Propagation of photons by hopping: A waveguiding mechanism through localized coupled cavities in three-dimensional photonic crystals,” Physical Review B, vol. 61, May 2000, pp. R11855-R11858.

[10] A. Yariv, Y. Xu, R. K. Lee, and A. Scherer, “Coupled resonator optical waveguide: A proposal and analysis,” Optics Letters, vol. 24, June 1999, pp. 711-713.

[11] U. Peschel, A. L. Reynolds, B. Arredondo, F. Lederer, P. J. Roberts, T. F. Krauss, and P. J. I. de Maagt, “Transmission and reflection analysis of functional coupled cavity components,” IEEE Journal of Quantum Electronics, vol. 38, July 2002, pp. 830-836.

[12] M. Banaee, A.G. Pattantyus-Abraham, and M.W. McCutcheon, “Efficient coupling of photonic crystal microcavity modes to a ridge waveguide,” Applied Physics Letters, vol. 90, May 2007, pp. 193106.1-193106.3.

[13] M. Loncar, T. Doll, J. Vuckovic, and A. Scherer, “Design and fabrication of silicon photonic crystal optical waveguides,” Journal of Lightwave Technology, vol. 18, October 2000, pp. 1402-1411.

[14] W. L. Barnes, A. Dereux, and T. W. Ebbesen, “Surface plasmon subwavelength optics,” Nature, vol. 424, August 2003, pp. 824-830.

[15] E. N. Economou, “Surface plasmons in thin films,” Physical Review, vol. 182, June 1969, pp. 539-554.

[16] R. Zia, M. D. Selker, P. B. Catrysse, and M. L. Brongersma, “Geometries and materials for subwavelength surface plasmon modes,” Journal of Optical Society of America, vol. 21, December 2004, pp. 2442-2446.

[17] L. Liu, Z. Hana, and S. Hea, “Novel surface plasmon waveguide for high integration,” Optics Express, vol. 13, August 2005, pp. 6645-6650.

[18] Wikipedia. Silver. http://en.wikipedia.org/wiki/Silver (accessed April 2009).

[19] Wikipedia. Gold. http://en.wikipedia.org/wiki/Gold (accessed April 2009).

[20] R. G. Hunsperger, *Integrated Optics: Theory and Technology*. Berlin; New York: Springer-Verlag, 2002, ch. 8.

[21] A. Yariv, “Coupled-mode theory for guided-wave optics,” IEEE Journal of Quantum Electronics, vol. QE-9, September 1973, pp. 919-933.

[22] C. Manolatou, S. G. Johnson, S. Fan, P. R. Villeneuve, H. A. Haus, and J. D. Joannopoulos, “High-density integrated optics,” Journal of Lightwave Technology, vol. 17, September 1999, pp. 1682-1692.

# Chapter 3

# Compact and Ultra-Low-Loss Planar Photonic Crystal Taper

In this chapter, we propose two novel methods to enhance the coupling efficiency between a dielectric waveguide and a planar photonic crystal [1-4]. The proposed methods are based on introducing structural imperfections to change the mode size and shape inside the taper to match that of the photonic crystal line-defect waveguide. One method is by changing both the size and position of the inner taper rods [1-3] and the other is by creating several cavities on both sides of the tapered waveguide before applying the position change method [4].

## 3.1 Introduction

The field of guiding and controlling light was enhanced since the invention of photonic band gap (PBG) [5,6]. Unlike slab waveguides that guide light by total internal reflection, PBGs guide light by trapping and localizing it (i.e., Bragg reflection). The light waves

with a certain range of frequencies cannot propagate through a photonic crystal (PC) structure due to the distributed Bragg reflection from the bulk crystals. Modes within the PBG can be introduced by perturbing the periodicity of the PC, either by introducing a point or a line defect. These mode defects are the key factor for having many applications for PBGs such as waveguides, resonators, splitters, wavelength division multiplexers, and switches.

One method that is widely utilized to make a two-dimensional (2D) PC act as a three-dimensional (3D) structure is by using a planar photonic crystal (PPC) [7]. The propagated light is localized in the in-plane direction by the distributed Bragg reflection and in the out-of-plane direction by the total internal reflection.

High coupling efficiency is required in optical integrated circuits between a dielectric waveguide (DWG) and a PPC waveguide. To achieve a high power transmission, their modes should match. There are two problems with such coupling: a difference in width and a difference in propagation mechanism, which cause both high reflection and radiation losses due to the mismatch between the propagating constants in both waveguides. The coupler that attracted attention to solve these coupling problems was a tapered waveguide that can be achieved by either tapering the DWG [8,9] or the PPC taper [10-15]. Khoo *et al.* [13] found that the coupling efficiency from a single mode fiber into a convex shape taper in vacuum is better than that into a concave or linear taper. Mittal and Sabarinathan [14] found that the coupling efficiency from unequal step tapered PC is higher than that from an equal step taper. Sanchis *et al.* [15] used both a PC tapered waveguide and two extra defects at the interface between the DWG and the PPC waveguide. They achieved over 80% coupling efficiency.

In this work, we apply two novel methods to enhance the coupling efficiency between a DWG and a PPC waveguide. The proposed methods are based on introducing structural imperfections to change the mode size and shape inside the taper to match that of the PC waveguide. Method one involves changing both the size and position of the inner taper rods [1-3], whereas method two involves creating several cavities at both ends next to the upper taper rods before applying method one [4]. In our proposed methods, each inner taper rod is treated as matching impedance that is tuned by changing its size and position until maximum coupling is reached. The rods in each layer cause partial reflection of the incident light. Total constructive interference occurs when the integer multiple of the wavelength satisfies Bragg's law. Our proposed methods involve the addition of extra defects at the interface between the DWG and PPC waveguide. The proposed methodology can be applied to PPC tapers of different lengths, widths, and lattice geometries to achieve mode matching with dielectric waveguides of different widths. In this work, we provide two examples for a compact mode-matching taper between a 3 μm wide DWG and a 1 μm long PPC taper. One example is for a triangular lattice of circular silicon pillars embedded in silica and another is for a hybrid lattice (i.e., triangular and square) of square silicon pillars embedded in silica. The size and position of each inner taper rod are optimized to achieve high coupling efficiency from a DWG into a PPC. The two proposed methods are as follows:

## 3.2 Method 1: Size and Position Change Methods

This method is based on changing both the size and position of each inner taper rod before and after the addition of extra defects at the interface between the DWG and PPC

waveguide. We applied each method (i.e., size and position) individually using the structure that is described in Figure 3.1. Then, we took the best structure (i.e., the design with the highest coupling efficiency) that resulted from each method and applied the other method to that structure.

### 3.2.1 Coupling Technique and Numerical Results

A 2D triangular PC structure of lattice constant $a$ = 0.465 μm is shown in Figure 3.1(a). The rods have a circular shape of radius 0.2$a$ and a refractive index of 3.45, which is the refractive index of silicon at a wavelength of 1.55 μm. The rods are embedded in a refractive index of 1.45, which is the index of silicon dioxide. Also, the 3 μm wide DWG has a core refractive index of 1.45. The PC single mode waveguide is introduced by removing one line from the PC periodic structure. The PC taper length and width are 2$a$ and 8.66$a$, respectively. The whole device is surrounded by air. The normalized frequency range of the photonic band gap (PBG) for transverse magnetic waves is between 0.267($a$/λ) and 0.361($a$/λ) as shown in Figure 3.1(b). The PBG is almost centered at $\lambda_o$ = 1.55 μm. The 2D finite-difference time-domain method is used to analyze all the designed couplers presented in this work. Each structure is terminated by a perfectly matched layer in order to reduce the back reflection from the waveguide ends.

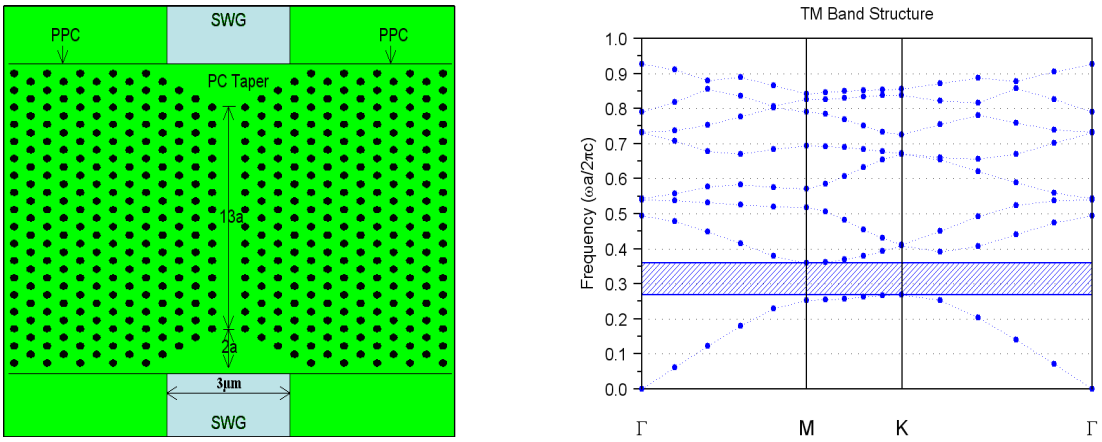


(a) (b)

Figure 3.1: Structure: (a) a two-dimensional triangular PC structure (i.e., basic structure) and (b) transverse magnetic band structure.

In order to enhance the mode coupling between the DWG and PPC waveguide, the size and position of each inner taper rod are changed until maximum coupling is reached. This perturbation of the periodicity of this subset of rods proved to be very critical in improving the coupling efficiency. A defect can be introduced in a photonic structure by changing its shape, size, or dielectric constant. By introducing a defect at least one mode can be created at a frequency that can be tuned by the defect features. Villeneuve *et al.* [16] changed the dielectric material of a unit cell by changing the size of a single rod. They found that reducing the size of the rod (i.e., removing dielectric material) created a mode closer to the lower edge of the PBG. This is similar to an acceptor atom in semiconductors. On the other hand, increasing the size of the rod (i.e., adding dielectric material) created a mode closer to the upper edge of the PBG. This is similar to a donor atom in semiconductors. In both cases, the created mode frequency can be tuned by continuing to change the size of the defect. The mode is more confined when its frequency is at the center of the PBG. Sometimes it is not possible to tune the defect mode to a frequency, which lies in the middle of the PBG due to the fact that the

electromagnetic field is no longer localized in the defect region. It will be localized in the region of the crystals surrounding the defect [17]. Jafarpour *et al.* [18,19] studied the effect of changing the size and periodicity of the air-holes that surround a line defect waveguide. They found that the effective bandwidth is reduced by changing the size of the air-holes while the bandwidth is increased when the period of the air-holes is changed. The increase in the bandwidth is at the expense of making the line defect waveguide a multimode waveguide. This mode behavior is the basic idea behind the size and position change methods. Each inner taper rod is used to tailor the mode profile so that mode matching occurs between the DWG and PPC waveguide. The mode matching is achieved by changing the size and position of each inner taper rod until maximum coupling is reached. The size method is done by changing the size of each inner taper rod from zero to twice the size of a bulk rod. The position method is done by moving each inner taper rod in twelve different directions (d1-d12) until it overlaps with another rod, as shown in Figure 3.2(a).

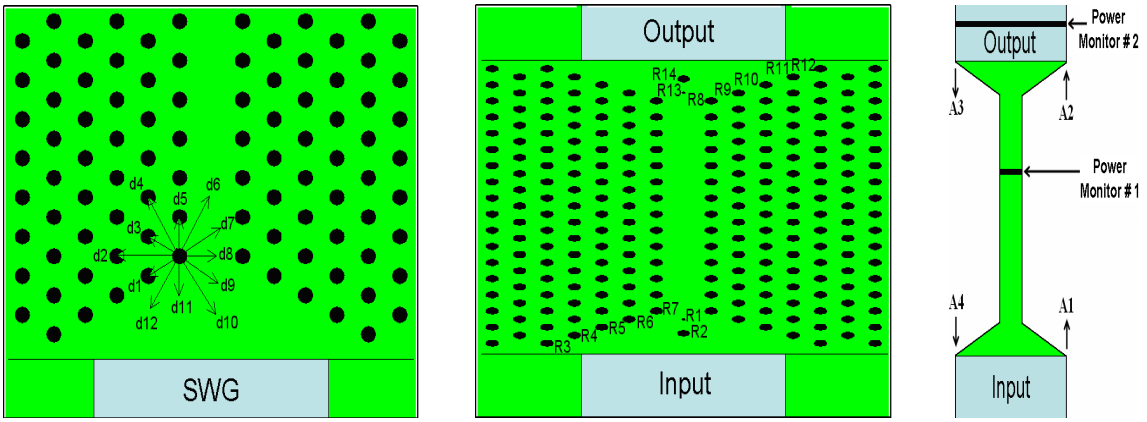


(a) (b) (c)

Figure 3.2: Measurement strategy: (a) the twelve directions that each rod can move to, (b) the symbols that are given for the inner taper rods and extra defects, and (c) the places of the two monitors that are used to measure the coupled power and the order (A1 to A4 directions) in which the size and position change methods are performed on the inner taper rods.

The PPC taper acts as a mode transformer, which enhances the mode coupling adiabatically over a slowly varying taper. Mode coupling increases significantly as the taper length is increased except in the cases where either evanescent or radiated modes exist. Theoretically, as the taper length goes to infinity, all modes couple to the fundamental mode. Practically, taper lengths are finite and in turn total coupling cannot be achieved [20]. This problem can be partially solved by adding extra defects in the middle of the taper between the DWG and PPC. As shown in Figure 3.2(b), the inner taper rods are given the symbols (R3-R7) and (R8 R12) for the input and output PC tapers respectively, while the extra two defects at the input and output are given the symbols (R1, R2, R13, and R14). Figure 3.2(c) shows the places of the two monitors that are used to measure the coupled power from the first and second PC taper, respectively. One of the monitors is placed inside the line defect and the other is placed in the second DWG. The size and position of the extra defects are investigated by moving a rod, which has the same size as that of the bulk rods, from the bottom of the taper to its top. A rod is put at each maxima of the measured power as shown in Figure 3.3(a). The radius of the R1 rod is changed from zero to 0.4$a$ while the R2 rod is held fixed. The same approach is done to find out the radius of the R2 rod after fixing the radius of the R1 rod at the value that resulted in maximum coupling. The radii of the two extra defects are shown in Figure 3.3(b). The same procedure is followed to find the location and radius of the other two extra defects at the output taper (R13 and R14).

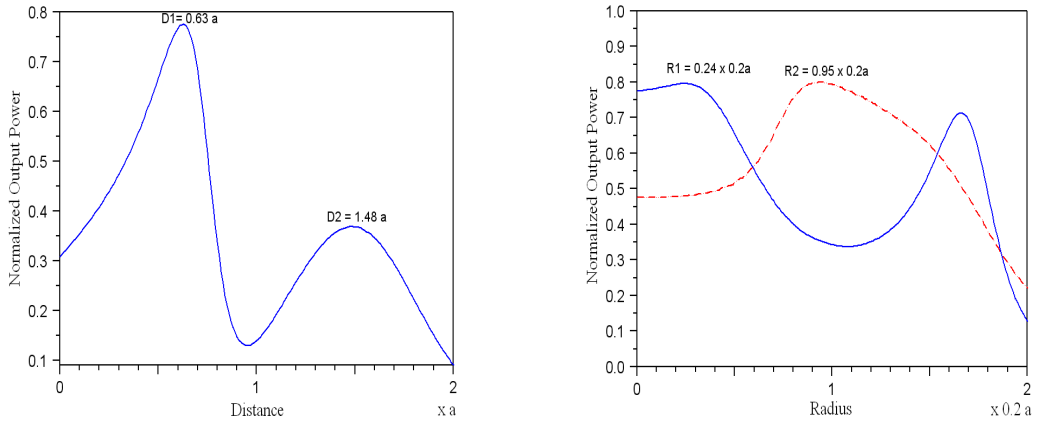


(a) (b)

Figure 3.3: Extra defects' locations and sizes: (a) the location of the two extra defects R1 and R2 for the structure shown in Figure 3.2(b) and (b) the radius of R1 (solid line) and radius of R2 (dashed line).

Wu *et al.* [21] found that the coupling efficiency into and out of a line defect waveguide in a PC structure is affected by the morphology of the input and output in addition to the crystalline orientation of the line defect waveguide. They also found that in order to achieve maximum coupling efficiency, the input and output geometries are not required to be the same. Lin and Li [22] argued that the asymmetry of the input and output geometries is due to the different scattering mechanisms that the wave faces when entering or exiting the line defect waveguide. Therefore, we expect different taper geometries based on the starting inner taper rod. The R3 to R7 rods can be changed starting from the bottom of the taper to its top (A1 direction) or from its top to its bottom (A4 direction), as shown in Figure 3.2(c). The bottom of the taper faces the DWG and the top of the taper faces the line defect waveguide. The same scenario is applied to the inner taper rods at the output (R8 to R12 rods). Based on the starting point, four possible structures can be designed: A1-A2 direction (i.e., bottom of the input taper and top of the output taper), A1-A3 direction (i.e., bottom of the input taper and bottom of the output taper), A4-A2 direction (i.e., top of the input taper and top of the output taper), and A4-A3 direction (i.e., top of the input taper and bottom of the output taper).

The output power profile changes when the sizes or positions of any two counterpart inner taper rods are changed at the same time. Figure 3.4 shows a sample of the output power profile for the size change of the two R7 rods and the position change of the two R5 rods. As shown in the figure, in order to enhance the coupling efficiency, the radii of the two R7 rods should be increased by 0.22*a* while the positions of the two R5 rods should be changed by 0.4*a* in the d5 direction.

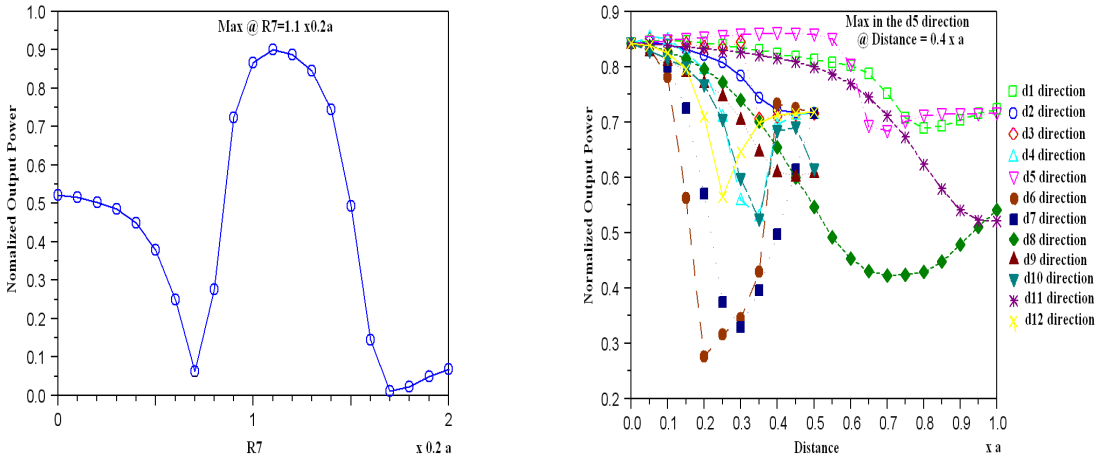


(a) (b)

Figure 3.4: The output power profile while changing: (a) the size of the two R7 crystals and (b) the position of the two R5 crystals.

Five steps are applied to design the structure that gave the highest coupling efficiency. Step 1: the size of each inner taper rod is changed from zero to 0.4*a* by following the four possible directions: A1-A2, A1-A3, A4-A2, and A4-A3. Step 2: extra defects are added at the interface for all the structures that resulted from Step 1. Step 3: extra defects are added before applying the size change method. Step 4: the other method is applied on the structure that had the highest coupling efficiency. Step 5: the previous four steps are repeated for the position change method.

### 3.2.2 Transmission Response

Figure 3.5 shows the coupling enhancement for all the couplers that are investigated in our work. The structure numbers shown in the figure are for the following situations: Structure 0 is for the situation in which neither extra defects nor size or position methods are used. Structures 1-4 are for the situation in which the size or the position change method is applied to Structure 0 in the four possible directions: A1-A2, A1-A3, A4-A2, and A4-A3 respectively. Structures 4-8 are for the situation in which extra defects are added for the Structures 1-4. Structures 9-12 are for the situation in which extra defects are added before the size or position change method is applied in the four possible directions.

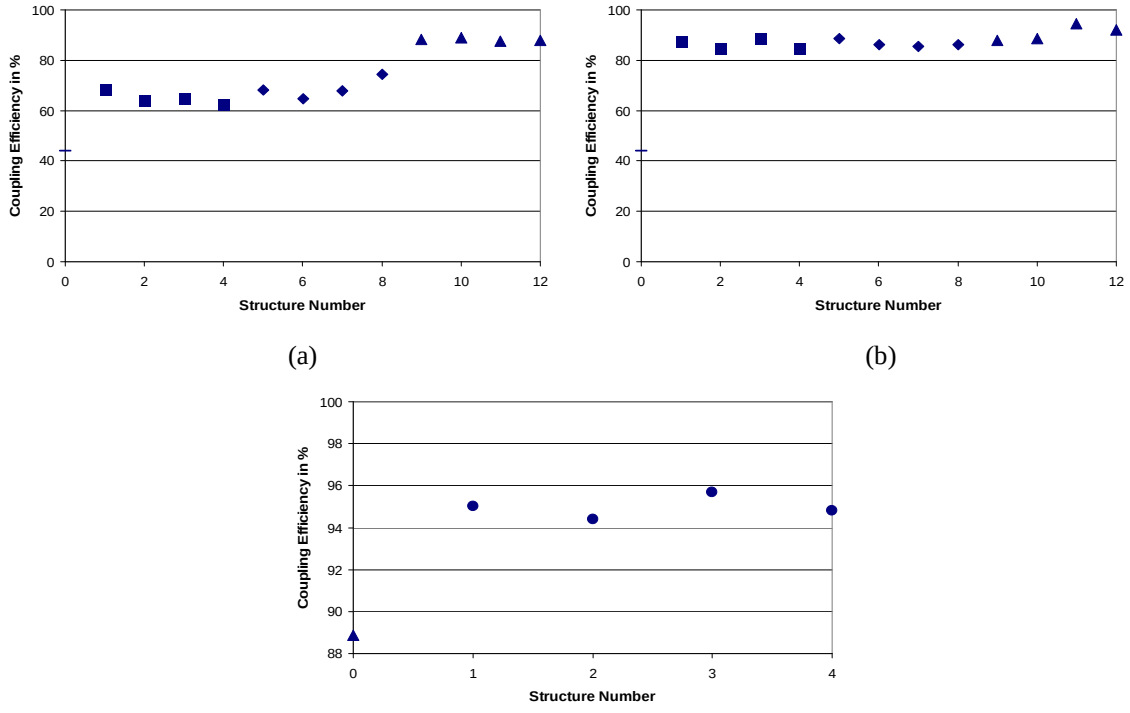


Figure 3.5: The coupling efficiency for all the investigated couplers that resulted from applying the: (a) size change method, (b) position change method, and (c) position change method to the best structure that resulted from the size change method. Each point symbol represents the result of the following PPC taper situations: – PPC taper without extra defects and without inner taper shape change (basic structure), ■ PPC taper after applying the size or position change method to the basic structure, ◆ PPC taper with extra defects added to the ■ structures, ▲ PPC taper with defects added before applying the size or position change method, and ● PPC taper for the structure shown in Figure 3.5(a) after applying the position change method.

As shown in Figure 3.5(a), the coupling efficiency is improved by changing the size of each inner taper rod. It was 44% for the basic structure and increased to 68% after changing the size of each inner taper rod for the A1-A2 direction. The efficiency further increased to 74% (A4-A3 direction) after using extra defects at the input and output tapers. More coupling was achieved by applying the size change method after adding the two extra defects at the input and output tapers. The maximum coupling efficiency was approximately 88% for the structure that has the A1-A3 direction. Much better coupling was found by applying the position change method. As shown in Figure 3.5(b), the output power increased from 44% to approximately 89% for the structure that has the A4-A2 direction after applying the position change method. Adding extra defects to the structures did not increase the coupling efficiency. All the structures remained at the same value except for the structure at the A4-A2 direction that decreased by more than 5%. Better results were achieved by applying the position change method after adding the two extra defects at the input and output tapers. The maximum coupling efficiency was above 94% for the structure that has the A4-A2 direction. Figure 3.5(c) shows the output coupling efficiency after applying the position change method to the best structure that resulted from applying the size change method. The coupling efficiency increased from 88% to 96% for the structure that has the A4-A2 direction. Applying the same strategy to the best structure resulted from the position change method, did not enhance the coupling efficiency.

The best coupler that resulted from applying the size change method is shown in Figure 3.6(a), while that based on the position change method is shown in Figure 3.6(b). Figure 3.6(c) shows the resulted coupler after applying the position change method to the

structure in Figure 3.6(a) (i.e., the coupler that resulted in the highest coupling efficiency). The input and output taper geometries are not the same. This is because light faces different scattering mechanisms when entering or exiting the line defect waveguide.

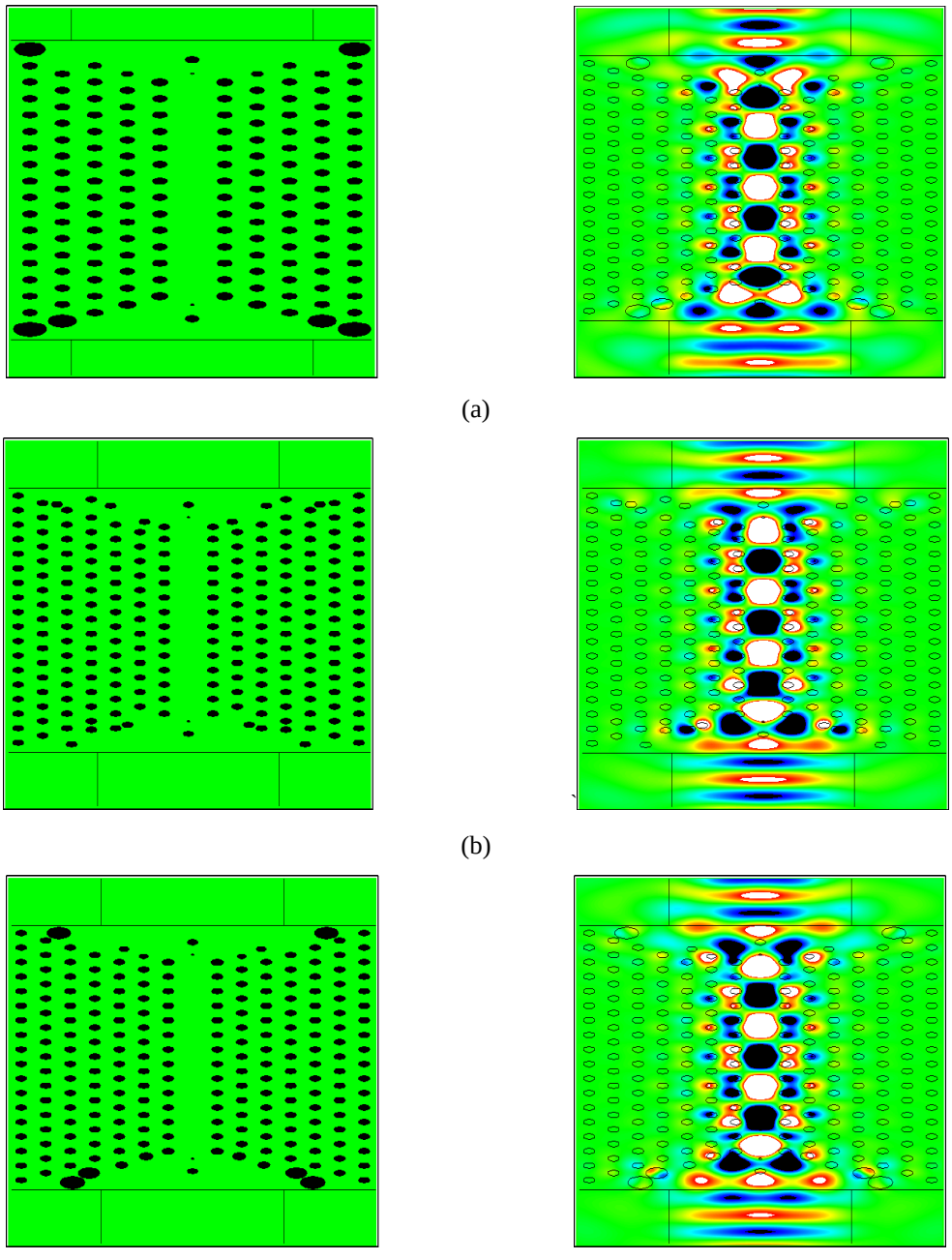

Figure 3.6: The final couplers and field distribution that resulted after: (a) adding the extra defects before applying the size change method (A1-A3 direction), (b) adding the extra defects before applying the position change method (A4-A2 direction), and (c) changing the position of each inner taper crystal of Figure 3.6(a) in the A4-A2 direction.

Figure 3.7 shows the power transmission spectrum of the couplers in Figure 3.6. The output power at the second DWG is continuously measured as the wavelength value is changed. Several peaks appeared as the wavelength increased from 1.288 μm to 1.742 μm. These peaks are similar to a Fabry-Perot cavity which are formed by the sides of the taper and the extra two defects. Increasing the taper length reduces these peaks by enabling more modes to couple adiabatically over a slowly varying taper. The maximum power in Figure 3.7(a) is 90% at 1.558 μm, which means that the field is more confined at this wavelength. In Figures 3.7(b and c), the maximum power is at 1.55 μm. The spectrum that is shown in Figure 3.7(b) is not as wide as that shown in Figure 3.7(a) due to the position change of the inner taper rods. Figure 3.7(c) is the spectrum of the coupler that resulted after applying the position method on the structure that has its spectrum in Figure 3.7(a). The spectrum shape of Figure 3.7(c) is similar to that of Figure 3.7(a), which means that the spectrum did not change due to applying the position change method. The effect it had is that it made light more confined at 1.55 μm and consequently increased the coupling efficiency from 88% to 96%.

We believe that the most efficient method to design a PC taper coupler is by adding extra defects at the input and output tapers followed by increasing the size of each inner taper rod starting from zero to 0.4*a*. Then, the rod should be moved in twelve different directions, as shown in Figure 3.2(a), until maximum coupling is achieved.

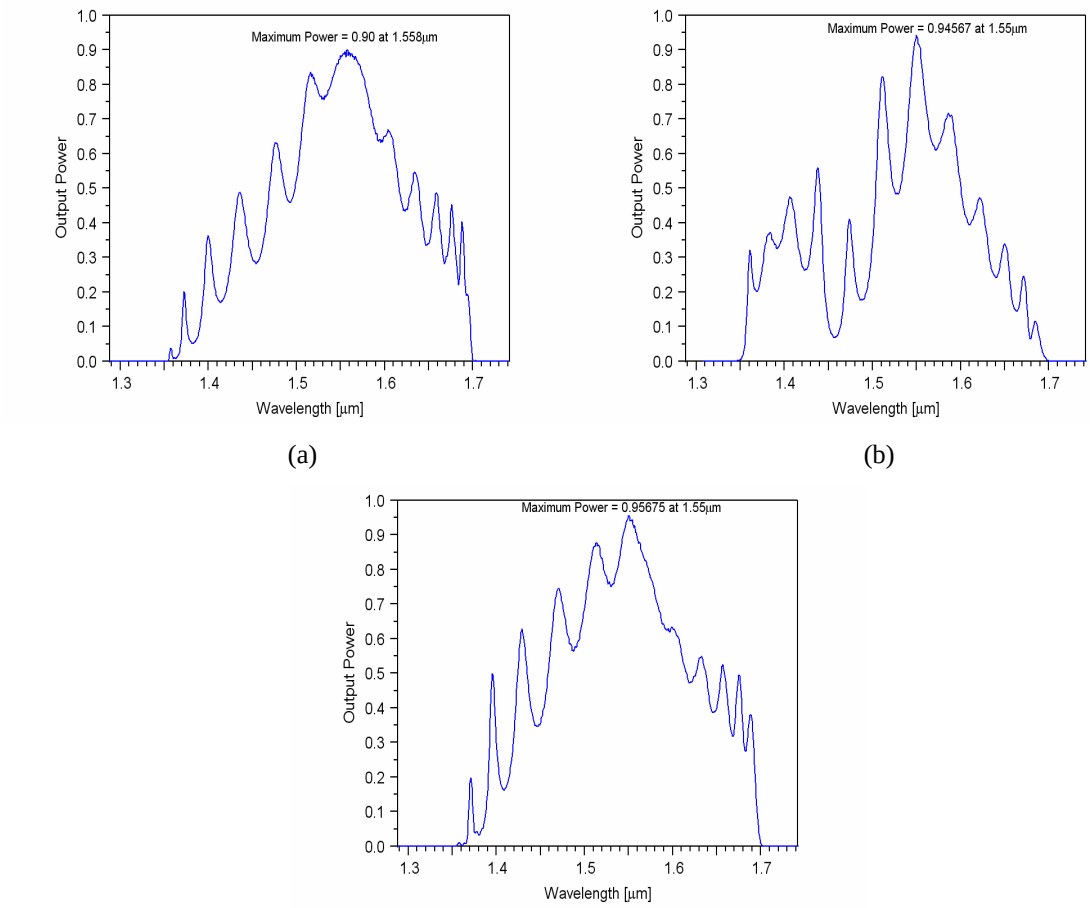


Figure 3.7: Power transmission spectrum of the couplers in Figure 3.6, respectively.

## 3.3 Method 2: Coupled Cavity Method

In this method, we used a hybrid structure that combines triangular and rectangular rod structures. A series of cavities were created on both sides of the tapered waveguide. Light from the taper is coupled into the introduced cavities before it is coupled into the line defect waveguide. The coupling efficiency was further improved by changing the position of the inner taper rods.

### 3.3.1 Coupling Technique and Numerical Results

The coupler between the DWG and PPC waveguide presented here is the same as that described in Section 3.2.1 except that the rod has a square shape of dimensions 0.4*a*. In order to increase the coupling efficiency between the two waveguides, several cavities were introduced at both ends next to the upper taper rods, which are located at 2*a*. The cavities were introduced by shifting the whole rods of alternating columns, as shown in Figure 3.8(a). The PC tapered part of the waveguide was kept as a triangular array. The measured output power as a function of the translation rod columns Z is shown in Figure 3.8(b). The measurements were taken inside the line defect waveguide. The output power started at 44% of the input power and gradually increased until Z ≅ 0.22*a* and then it rapidly increased to reach a peak of 86% at Z = 0.35*a*.

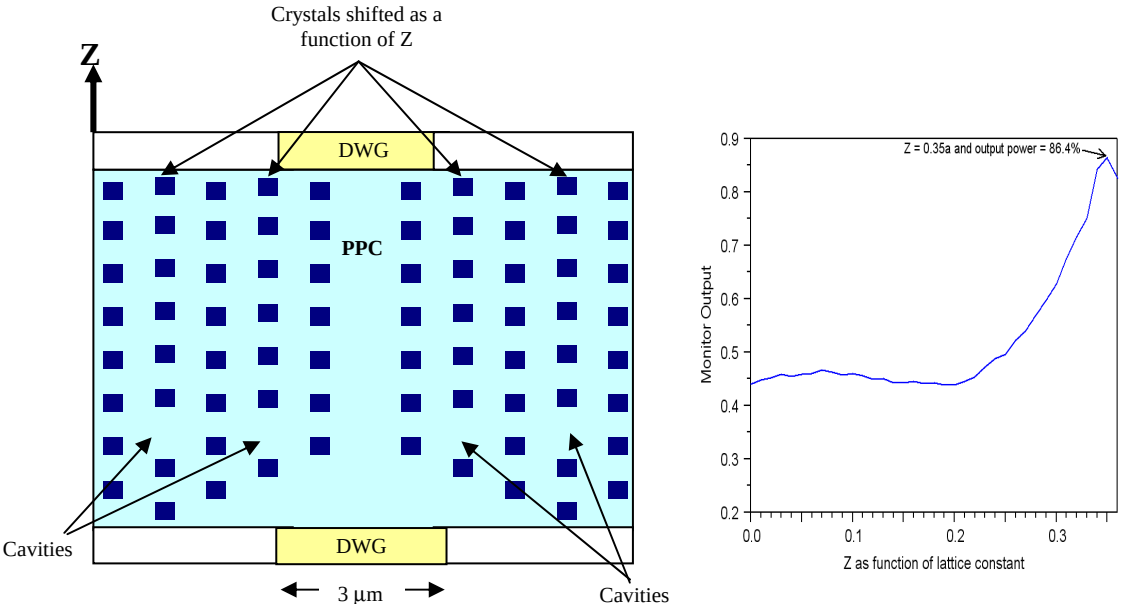


(a) (b)

Figure 3.8: (a) Schematics of the PC structure with the cavities and (b) the output power as a function of Z.

The coupling efficiency is further increased by using extra defects at the interface between DWG and PPC to approximately 96%. We followed the same procedure described in Section 3.2.1 to add the two extra defects. A defect was put at each maxima of the measured power, as shown in Figure 3.9(a). The positions of the two extra defects were at 0.8*a* ($d_{external}$) and 2.9*a* ($d_{internal}$) measured from the bottom of the PC taper. The dimensions of those two extra defects were 1.1*a* and 0.7*a*, respectively (as shown in Figure 3.9(b)). The position of the defect at 2.9*a* did not block light because it acted as a cavity with the other extra defect at 0.8*a*. Applying the position change method increased the coupling efficiency by 2%. The same procedure was also carried out for the 2nd taper inner rods. This resulted in the coupling efficiency of approximately 94% between the two silica waveguides. The schematic of the final coupler is shown in Figure 3.10.

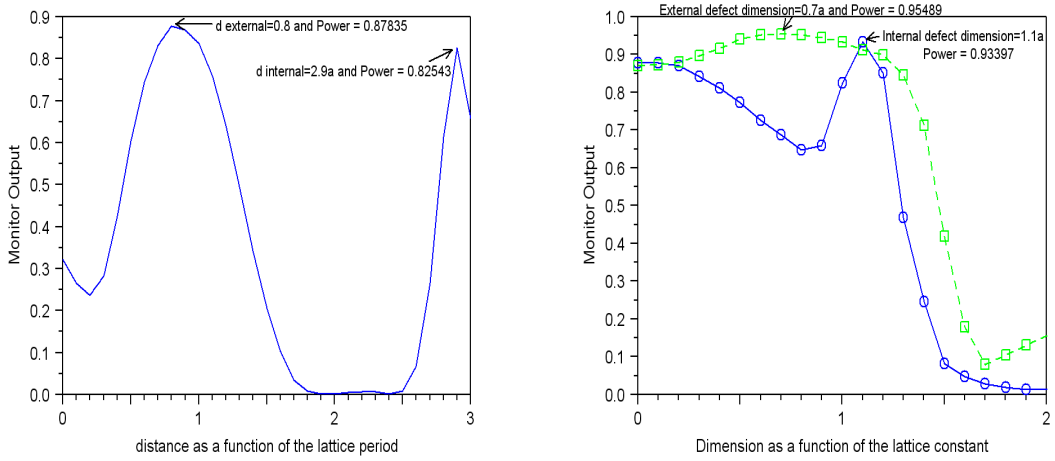


(a) (b)

Figure 3.9: (a) Extra defects' positions and (b) dimensions.

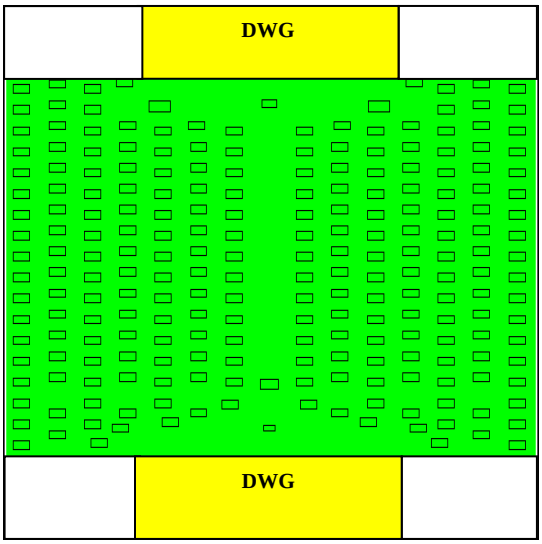


Figure 3.10: Schematic of the final designed hybrid coupler.

### 3.3.2 Transmission Response

Figure 3.11 shows the power transmission spectrum of the coupler in Figure 3.10. The output power at the second DWG is continuously measured as the wavelength value is changed from 1.288 μm to 1.742 μm. Several peaks appeared as the wavelength is increased. These peaks are similar to a Fabry-Perot cavity which are formed by the sides of the taper, the extra two defects, and the introduced cavities. The maximum power is 94% at 1.55 μm, which means that the field is more confined at this wavelength. The spectrum that is shown in Figure 3.11 is smaller than that shown in Figure 3.7(b) due to the introduced cavities. Maximum coupling into the line defect waveguide occurs when the forward light and the coupled light in the cavities interfere constructively. The most effective cavity is the one that is next to the top taper. The coupled power decreases as the light couples into more than two cavities. The input and output taper geometries are not the same. This is because light faces different scattering mechanisms when entering or exiting the line defect waveguide.

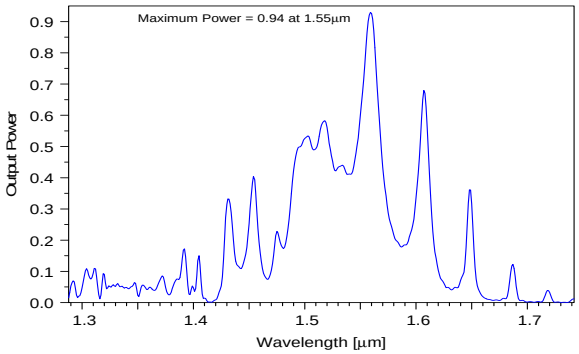


Figure 3.11: Power transmission spectrum of the hybrid coupler in Figure 3.10.

## 3.4 Summary

In this chapter, we showed that changing the size and position of the inner taper rods did increase the coupling efficiency between a dielectric waveguide and a planar photonic crystal from 44% to 96%. We also showed that creating a series of cavities next to the upper taper rods' position increases the coupling efficiency to 86%. The coupling efficiency was further improved to 94% after applying the position change method.

## References

[1] M. A. G. Abushagur and R. A. Wahsheh, "Radii changing effect on the coupling efficiency between a silica waveguide and a planar photonic crystal, Proceedings of SPIE - The International Society for Optical Engineering, vol. 5510, October 2004, pp. 71-77.

[2] R. A. Wahsheh and M. A. G. Abushagur, "The effect of changing the position of the inner taper crystals on the coupling efficiency between a silica waveguide and a planar photonic crystal," International Symposium on High Capacity Optical Networks and Enabling Technologies, HONET, November 2007, pp. 1-5.

[3] R. A. Wahsheh and M. A. G. Abushagur, “Compact and ultra-low-loss planar photonic crystal taper,” Microwave and Optical Technology Letters, vol. 52, March 2010, pp. 1454-1459.

[4] M. A. G. Abushagur and R. A. Wahsheh, “Highly efficient optical coupler using hybrid photonic crystal structures,” Proceedings of SPIE - The International Society for Optical Engineering, vol. 5510, October 2004, pp. 68-70.

[5] E. Yablonovitch, “Inhibited spontaneous emission in solid-state physics and electronics,” Physical Review Letters, vol. 58, May 1987, pp. 2059-2062.

[6] S. John, “Strong localization of photons in certain disordered dielectric superlattices, Physical Review Letters, vol. 58, June 1987, pp. 2486-2489.

[7] M. Loncar, T. Doll, J. Vuckovic, and A. Scherer, “Design and fabrication of silicon photonic crystal optical waveguides, Journal of Lightwave Technology, vol. 18, October 2000, pp. 1402-1411.

[8] A. Mekis and J. D. Joannopoulos, “Tapered couplers for efficient interfacing between dielectric and photonic crystal waveguides, Journal of Lightwave Technology, vol. 19, June 2001, pp. 861-865.

[9] M. Banaee, A.G. Pattantyus-Abraham, and M.W. McCutcheon, “Efficient coupling of photonic crystal microcavity modes to a ridge waveguide, Applied Physics Letters, vol. 90, May 2007, pp. 193106.1-193106.3.

[10] A. Talneau, Ph. Lalanne, M. Agio, and C. M. Soukoulis, “Low-reflection photonic-crystal taper for efficient coupling between guide sections of arbitrary widths, Optics Letters, vol. 27, September 2002, pp. 1522-1524.

[11] T. D. Happ, M. Kamp, and A. Forchel, “Photonic crystal tapers for ultracompact mode conversion, Optics Letters, vol. 26, July 2001, pp. 1102-1104.

[12] P. Sanchis, J. Marti, A. Garcia, A. Martinez, and J. Blasco, “High efficiency coupling technique for planar photonic crystal waveguides, Electronics Letters, vol. 38, August 2002, pp. 961-962.

[13] E. H. Khoo, A. Q. Liu, and J. H. Wu, “Nonuniform photonic crystal taper for high-efficiency mode coupling, Optics Express, vol. 13, October 2005, pp. 7748-7759.

[14] S. Mittal and J. Sabarinathan, “Optimization of coupling and transmission through finite height SOI photonic crystal slab waveguides, Proceedings of SPIE - The International Society for Optical Engineering, vol. 5971, October 2005, pp. 59711J.1-59711J.8.

[15] P. Sanchis, J. Marti, J. Blasco, A. Martinez, and A. Garcia, “Mode matching technique for highly efficient coupling between dielectric waveguides and planar photonic crystal circuits, Optics Express, vol. 10, December 2002, pp. 1391-1397.

[16] P. R. Villeneuve, S. Fan, and J. D. Joannopoulos, “Microcavities in photonic crystals: Mode symmetry, tunability, and coupling efficiency, Physical Review B, vol. 54, September 1996, pp. 7837-7842.

[17] C.-S. Kee, J.-E. Kim, H. Y. Park, and K. J. Chang, “Defect modes in a two-dimensional square lattice of square rods, Physical Review E, vol. 58, December 1998, pp. 7908-7912.

[18] A. Jafarpour, E. Chow, C. M. Reinke, J. Huang, A. Adibi, A. Grot, L. W. Mirkarimi, G. Girolami, R. K. Lee, and Y. Xu, “Large-bandwidth ultra-low-loss guiding in

bi-periodic photonic crystal waveguides, Applied Physics B, vol. 79, September 2004, pp. 409-414.

[19] A. Jafarpour, J. Huang, M. Soltani, M. Askari, E. S. Hosseini, and A. Adibi, “Theoretical and experimental studies of mode dispersion in biperiodic photonic crystal structures, Proceedings of SPIE - The International Society for Optical Engineering, vol. 6128, March 2006, pp. 61280Q.1-61280Q.11.

[20] S. G. Johnson, P. Bienstman, M. A. Skorobogatiy, M. Ibanescu, E. Lidorikis, and J. D. Joannopoulos, “Adiabatic theorem and continuous coupled-mode theory for efficient taper transitions in photonic crystals, Physical Review E, vol. 66, December 2002, pp. 066608.1-066608.15.

[21] Y. Wu, X. Chen, Y. Zeng, and W. Lu, “Light coupling for single-mode photonic crystal waveguides, Physica E, vol. 35, August 2006, pp. 93-98.

[22] L.-L. Lin and Z.-Y. Li, “Sensitivity to termination morphology of light coupling in photonic-crystal waveguides, Physical Review B, vol. 69, May 2004, pp. 193103.1-193103.4.

# Chapter 4

# Low Crosstalk in Crossed Strip Waveguides Using a Photonic Crystal Cavity

In this chapter, we propose a method to achieve ultra-low crosstalk using a resonant cavity at the intersection between two waveguides formed in a square lattice photonic crystal structure [1-5]. Three photonic crystal couplers are studied: one consists of cylindrical silicon-rods in air, another consists of cubic silicon-rods in air, and the other consists of cubic air-holes in silicon. The rod-structure supports a transverse magnetic mode and the hole-structure supports a transverse electric mode. The quality-factor of the cavity is changed by increasing the number of rods (or holes) that form the cavity and by decreasing the spacing between the waveguide and the cavity. The optimized photonic crystal structures were fabricated on a silicon-on-insulator platform. Experimental results are shown for the cubic air-holes in silicon.

## 4.1 Introduction

When waveguides are crossed, the guided waves suddenly expand due to the lack of confinement in the lateral direction. This results in coupling into the intersecting waveguides in addition to radiation and scattering losses. Ultra-low crosstalk between intersecting waveguides is required in optical integrated circuits in order to minimize the required area to produce multiple optical devices on the same chip. Low crosstalk is also beneficial for improving bit rate in optical communications systems. Recent work has shown that crosstalk between photonic devices can be reduced to a much smaller degree than that between their electronic counterparts [6]. However, the low crosstalk essentially relies on designing innovative photonic structures. More recently, a number of structures have been proposed and investigated to eliminate crosstalk [7-11]. One method that attracts great attention is based on cavity coupling that can achieve low crosstalk over a wide spectrum [8-11]. The key idea is to excite modes orthogonal to each other at the intersection area. Johnson *et al.* [8] proposed a resonant cavity that supported two orthogonal modes at the intersection area of two line-defect waveguides in a two dimensional (2D) square lattice photonic crystal (PC) structure, which was composed of periodic cylindrical rods in air. In the work of Johnson *et al.* [8], as the quality factor (Q-factor) of the cavity increased by adding more rods next to the defect rod, crosstalk could be reduced. As a result of the Q-factor change, both the output bandwidth spectrum and crosstalk are controlled. Based on a similar structure, Liu *et al.* [9] reported crosstalk reduction by using two single mode coupled resonator optical waveguides that had nonoverlapping photonic band gap (PBG). Their results are very attractive and promising. Furthermore, all-optical transistors can potentially be achieved based on the

PC cross-waveguide geometry [12]. However, in both works of Johnson *et al.* [8] and Liu *et al.* [9] the structures had an infinite thickness and light was guided in air, or void PBG waveguides, instead of dielectric waveguides. As a result, the structures are only ideal 2D models that cannot be experimentally realized.

In order to experimentally demonstrate the structure proposed by Johnson *et al.* [8], Roh *et al.* [10] used two aluminum metal plates to insure confinement in the out-of-plane direction. One plate was placed on the top, and the other was placed at the bottom of the cylindrical alumina rods in air. Crosstalk reduction as large as −30 dB was experimentally achieved at the resonant frequency. However, this metallic-cladding structure cannot be scaled down for telecom wavelengths. To work for the telecom wavelengths, Teo *et al.* [11] fabricated a structure that was composed of 13 μm high silicon rods in air, which are too high to provide effective out-of-plane field confinement. For practical applications, a widely used way is to convert a 2D structure into a planar structure. Unfortunately, in a planar structure light cannot be confined in void PBG waveguides without out-of-plane confinement on light propagation.

Herein, we replace the air-line defect waveguides with strip waveguides to achieve out-of-plane confinement by total internal reflection. To illustrate the effectiveness of our design, we performed a series of simulations. First, the width of the strip waveguide was fixed at the value that resulted in high throughput and low crosstalk. Then, the Q-factor of the cavity was increased by adding more rods next to the defect rod. Subsequently, a comparison of simulation results between the structures with and without the strip waveguides was made. Next, the effect of reducing the spacing between the strip waveguide and cavity on the coupling efficiency and crosstalk was analyzed. Then, a

comparison of simulation results between the structures with and without the intersecting waveguide was made. Next, we analyzed the effect of replacing the cylindrical rods with cubic ones. Finally, we analyzed the image reversal of the cubic rods (i.e., cubic air-holes in silicon). We fabricated the optimized structures using silicon-on-insulator (SOI). The fabrication details and experimental results are described here.

## 4.2 Cylindrical Silicon-Rods in Air

Figure 4.1 shows 2D square lattice PC structures composed of cylindrical rods of radius 0.2$a$ ($a$ is the lattice constant of the PCs) with a dielectric constant of 11.56 surrounded by air. The transverse magnetic (TM) PBG of the structures is between 0.286($a/\lambda$) and 0.421($a/\lambda$). Two intersecting single mode line-defect waveguides are created by replacing a row and a column of rods with a dielectric strip waveguide. The strip waveguides have a width of 0.3$a$ and a dielectric constant as that of the bulk crystals. The resonant cavity at the center of the intersection is introduced by creating a defect rod of radius 0.3$a$ that has a resonant frequency of 0.362($a/\lambda$). The Q-factor of the cavity is increased by increasing the number of rods next to the defect. The following names are given to the structures that are shown in Figure 4.1 to denote the number of rods that form the cavity: “5 × 5”, “3 × 3”, and “1 × 1” for the structures that have five rods, three rods, and one rod at the intersection area, respectively [6].

The 2D finite-difference time-domain method is used to analyze all the designed structures presented in this chapter. Each structure is terminated by a perfectly matched layer in order to reduce the back reflection from the waveguide ends. A broadband TM Gaussian pulse is used as a light source. The pulse center is at a wavelength of 2.76$a$.

Two detectors are used to measure the forward (i.e., throughput) and crosstalk coupling powers. One is located at *W2* and the other at *W4*, as shown in Figure 4.1. The measured power is plotted as a function of frequency. A linear scale is used for the forward power measurement while a dB scale is used for the crosstalk measurement. In this chapter, the measured values of the throughput and crosstalk are taken at the resonance frequency. In addition, the (+) and (-) signs are used to denote gain and loss, respectively.

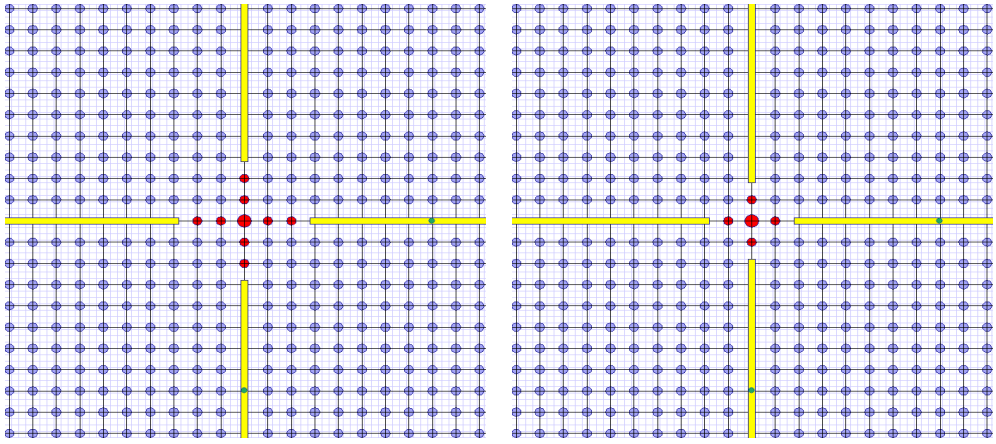

(a) (b)

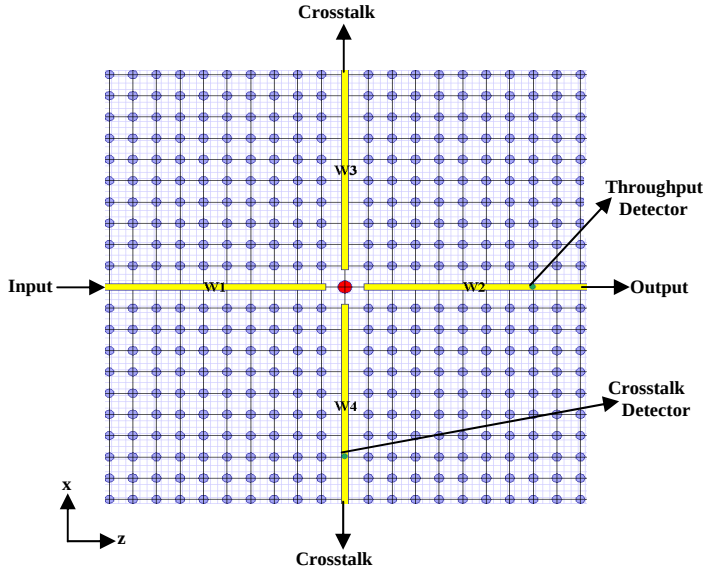


(c)

Figure 4.1: Two dimensional photonic crystal structures of circular rods in air for the following cavity sizes: (a) “5 × 5”, (b) “3 × 3”, and (c) “1 × 1”.

Four steps were followed in our work to investigate how the configuration parameters affect the performance of the structure:

Step 1: the width of the strip waveguide was determined by changing the width of the waveguide from 0.1*a* to 0.4*a* in steps of 0.1*a*. At each step, the throughput and crosstalk were measured. In all the proposed structures, the throughput decreased as the width of the waveguide changed from 0.4*a* to 0.1*a*. Whereas, the crosstalk decreased when the width of the waveguide changed from 0.4*a* to 0.3*a*, it then increased as the width decreased. For example, Figure 4.2 shows the throughput and crosstalk results for the "3 × 3" structure. The optimum width for the "3 × 3" structure and for the other structures was at 0.3*a*, which had the minimum crosstalk and a throughput value that was close to the maximum throughput value that is achieved by the 0.4*a* case.

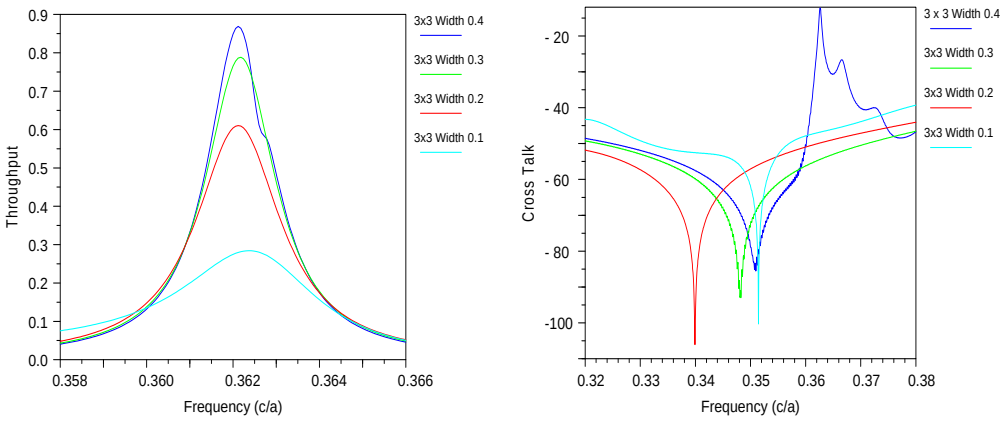


(a) (b)

Figure 4.2: (a) Throughput and (b) crosstalk of the "3 × 3" structure after changing the strip waveguide width from 0.4*a* to 0.1*a* in steps of 0.1*a*.

Step 2: after fixing the strip waveguide width, the cavity size was changed from "5 × 5" to "3 × 3" and from "3 × 3" to "1 × 1". At each cavity size, the throughput and crosstalk were measured. Figure 4.3 shows a comparison of the throughput and crosstalk of the structures with and without the strip waveguides. The measured crosstalk value for the "3 × 3" structure was about 21 dB lower than the value achieved without using the

strip waveguides, whereas the “1 × 1” and “5 × 5” structures showed an increase in the crosstalk. The addition of the strip waveguides caused the Q-factor of the cavity to increase for all the designed structures. The Q-factor for the “5 × 5”, “3 × 3”, and “1 × 1” structures changed from 900 to 1800, from 70 to 180, and from 6 to 13, respectively.

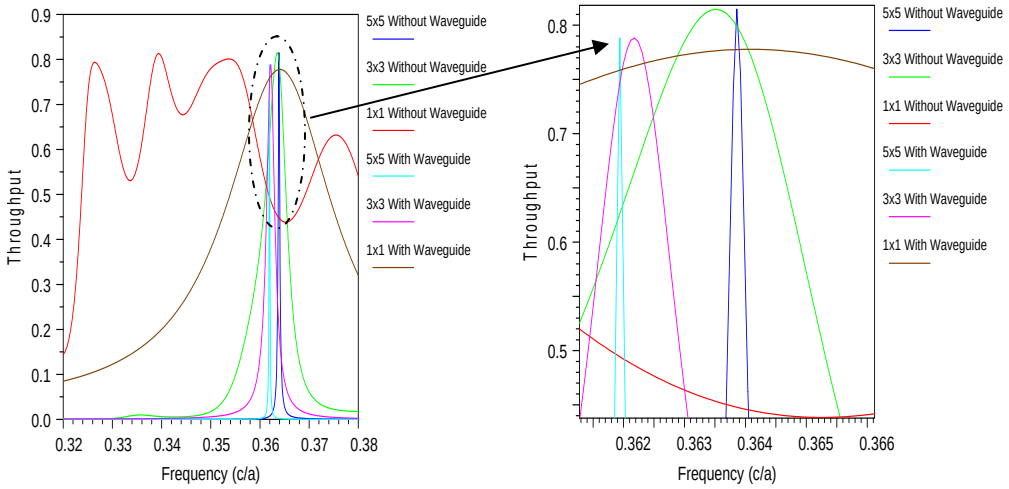


(a)

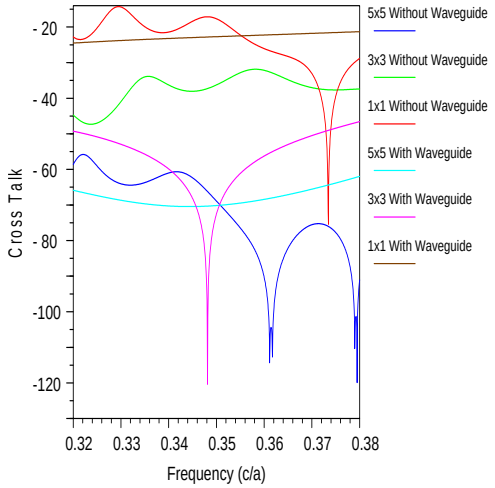


(c)

Figure 4.3: (a) Throughput (with its magnified view of the peak values) and (b) crosstalk for the structures shown in Figure 4.1 with and without the strip waveguides.

Step 3: the spacing between the strip waveguide and the closest rod of the cavity was changed in steps of 0.05*a* to reduce the Q-factor of the cavity. The edge to edge spacing between the waveguide and the closest rod is 0.6*a* for the “5 × 5” and “3 × 3” structures

and 0.5*a* for the "1 × 1" structure. As shown in Figure 4.4, the spacing values that resulted in less crosstalk were found at 0.4*a*, 0.5*a* and 0.15*a* for the "5 × 5", "3 × 3", and "1 × 1" structures, respectively. At these positions, we found that the measured throughput values for each structure (compared to the measured values without applying the space reduction method) changed by -0.80%, +0.07%, and +4.40%, while the measured crosstalk values changed by -23 dB, -22 dB, and -22 dB for the "5 × 5", "3 × 3", and "1 × 1" structures, respectively. The measured crosstalk values for the "3 × 3", and "1 × 1" structures are two times lower (in dB) than those reported in the literature. Applying the space reduction method caused a decrease in the Q-factor of the cavity for all the designed structures. The Q-factor for the "5 × 5", "3 × 3", and "1 × 1" structures changed from 1800 to 1340, from 180 to 160, and from 13 to 5, respectively.

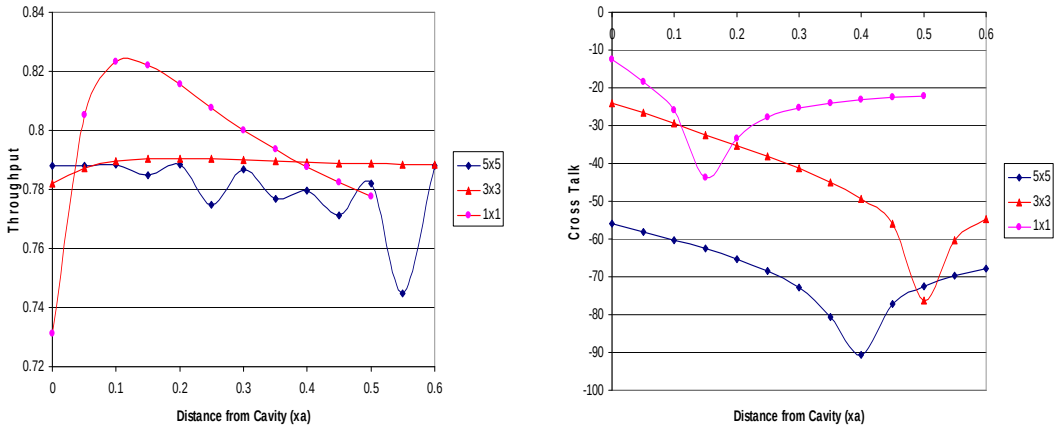


(a) (b)

Figure 4.4: (a) Throughput and (b) crosstalk for the "5 × 5", "3 × 3", and "1 × 1" structures while reducing the spacing between the waveguide and cavity in steps of 0.05*a*.

Step 4: to illustrate the effect of the intersecting waveguide on the coupling between the input and output waveguides, a comparison of throughput simulation results of the designed structures, with and without the intersecting waveguide, was made. As shown in Figure 4.5, the intersecting waveguide had a negligible influence on the coupling

efficiency. The measured throughput values after the addition of the intersecting waveguide changed by -0.025%, +0.003%, and -0.150% for the “5 × 5”, “3 × 3”, and “1 × 1” structures, respectively. The resonance frequency was the same after the addition of the intersecting waveguide for all structures except for the “1 × 1” structure in which the resonance frequency shifted slightly by 0.0016($a/\lambda$).

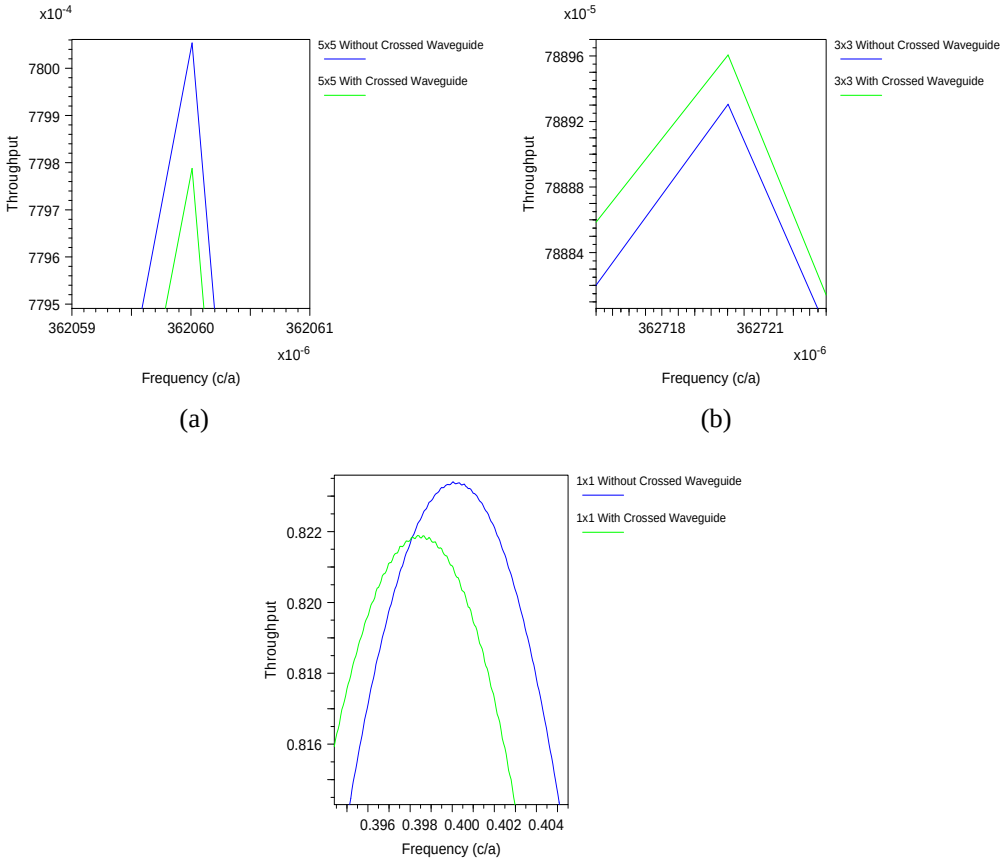


Figure 4.5: A comparison of throughput simulation results with and without the intersecting waveguide for the following cavity sizes (a) “5 × 5”, (b) “3 × 3”, and (c) “1 × 1”.

## 4.3 Cubic Silicon-Rods in Air

In our research work, we discovered that cubic rods offer better performance than cylindrical ones. This is due to the fact that the cubic rods have higher filling factor than that of cylindrical rods. However, this comes at the expense of reducing the PBG by 13%

(TM PBG between 0.268($a$/λ) and 0.385($a$/λ)). A broadband TM Gaussian pulse is used as a light source at a wavelength of 3.00$a$. To achieve better coupling into the cavity, the width of the strip waveguides was increased to 0.4$a$. As shown in Figure 4.6, the measured throughput values after using the cubic rods are changed by +5.70%, -3.55%, and -3.50% for the "5 × 5", "3 × 3", and "1 × 1" structures respectively, while the measured crosstalk values changed by -1 dB, -8 dB, and -1 dB. The Q-factor of the cavity was decreased after replacing the cylindrical rods by cubic rods. The Q-factor for the "5 × 5", "3 × 3", and "1 × 1" structures changed from 1800 to 1370, from 180 to 135, and from 13 to 11, respectively.

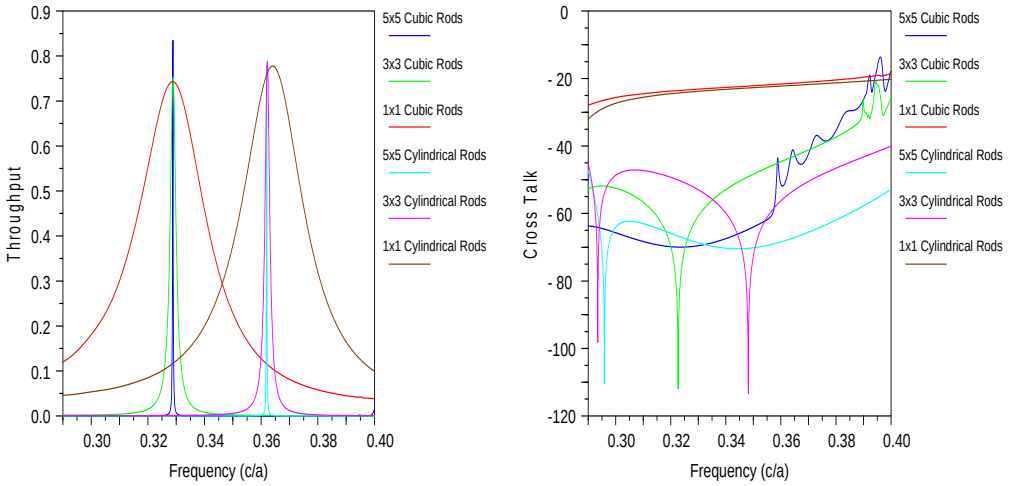


(a) (b)

Figure 4.6: A comparison of the (a) throughput and (b) crosstalk for the "5 × 5", "3 × 3", and "1 × 1" structures of cylindrical and cubic rods.

The spacing between the strip waveguide and the closest rod of the cavity was changed in steps of 0.05$a$. The edge to edge spacing between the waveguide and the closest cubic rod is 0.6$a$ for the "5 × 5" and "3 × 3" structures and 0.5$a$ for the "1 × 1" structure. The throughput and crosstalk were measured for each step. As shown in Figure 4.7, the spacing values that resulted in less crosstalk were found at 0.35$a$, 0.55$a$ and 0.2$a$ for the "5 × 5", "3 × 3", and "1 × 1" structures, respectively. At these positions, we found

that the measured throughput values for each structure (compared to the measured values without applying the space reduction method) changed by +2.5%, -0.02%, and +3.8%, while the measured crosstalk values changed by -36 dB, -28 dB, and -20 dB for the "5 × 5", "3 × 3", and "1 × 1" structures, respectively. The measured crosstalk values for all the structures are almost 14 dB lower than that of the cylindrical rods except for the "1 × 1" structure in which the same crosstalk is measured. Applying the space reduction method caused a decrease in the Q-factor of the cavity for all the designed structures. The Q-factor for the "5 × 5", "3 × 3", and "1 × 1" structures changed from 1370 to 780, from 135 to 120, and from 11 to 3.50, respectively.

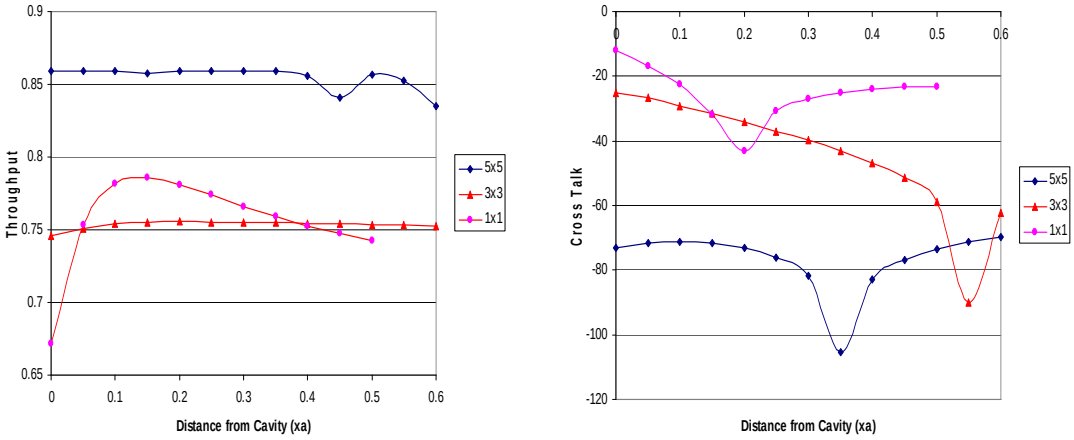


(a) (b)

Figure 4.7: (a) Throughput and (b) crosstalk for the "5 × 5", "3 × 3", and "1 × 1" structures while reducing the spacing between the waveguide and cavity in steps of 0.05*a*.

## 4.4 Cubic Air-Holes in Silicon

In order to achieve low crosstalk for transverse electric (TE) modes, we propose a 2D square lattice PC structure composed of square air-holes in silicon of a width of 0.8*a*. The PBG of the structure for TE modes is between 0.30(*a*/λ) and 0.39(*a*/λ). Two intersecting line-defect waveguides are created by replacing a row and a column of air-holes with a

dielectric strip waveguide. The strip waveguides have the same width as that of the bulk air-holes. The resonant cavity at the center of the intersection is introduced by creating a defect air-hole of a width of 0.6*a*. The cavity size is changed by increasing the number of air-holes that form the cavity. Similar levels of low crosstalk can be achieved in this configuration as shown in Figure 4.8. The Q-factor for the "7 × 7", "3 × 3", and "1 × 1" structures are 250, 30, and 5, while the crosstalk values are -40 dB, -22 dB, and -10 dB respectively.

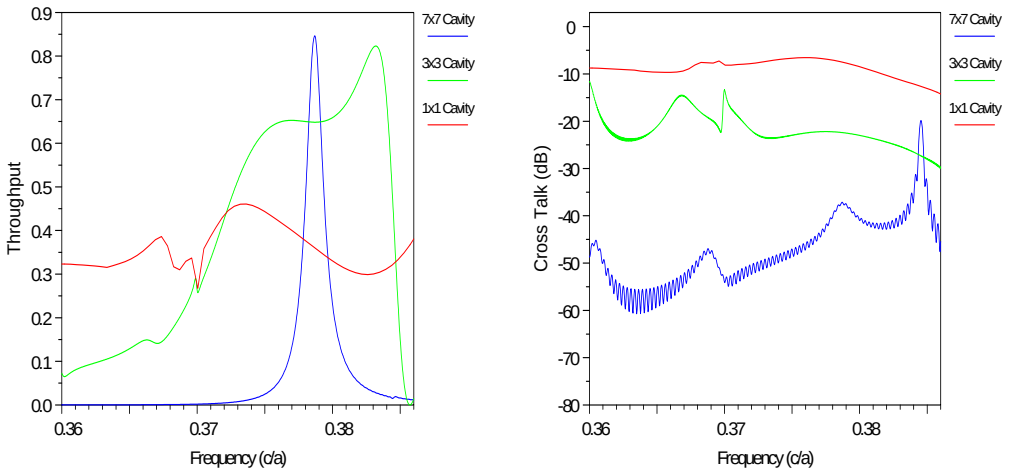


(a) (b)

Figure 4.8: (a) Throughput and (b) crosstalk for the "7 × 7", "3 × 3", and "1 × 1" structures of cubic air-holes in silicon.

## 4.5 Fabrication of the PC Structures

We fabricated the cylindrical silicon-rods and the cubic air-holes structures on SOI using electron-beam lithography. The scanning electron microscope (SEM) images of the structures are shown in Figure 4.9. According to 3D simulations, we found that in order to have a PBG centered at 1550 nm, the height of the silicon rods should be 2.25*a* (1035 nm) and the lattice period of the structure should be 460 nm. In addition, the whole structure must be buried in silicon oxide in order to maximize the PBG and provide index

guiding in the vertical direction. On the other hand, the height of the air-hole should be 250 nm and the lattice constant should be 560 nm. To maximize the PBG, the buried oxide is etched using a buffered oxide etchant solution for 10 minutes.

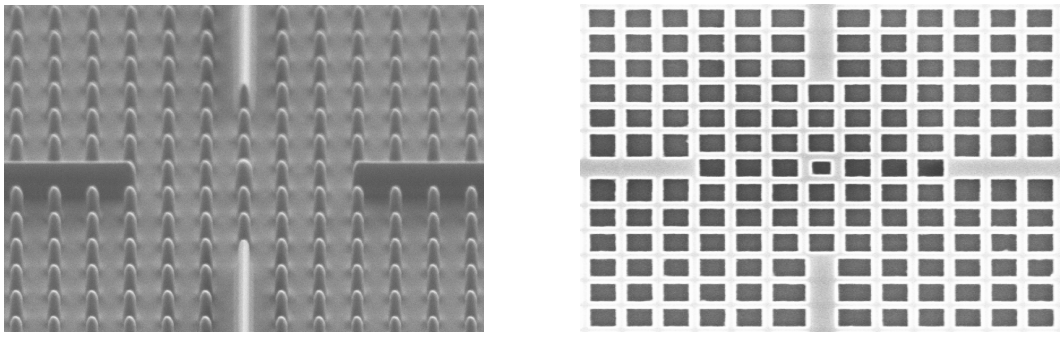

(a) (b)

Figure 4.9: Fabricated photonic crystal structures of (a) circular rods in air and (b) air-holes in silicon.

The optimized PC structures were fabricated on an SOI platform. The SOI wafer has a buried silicon oxide layer of a width of 4000 nm. The SOI wafer was spun coated with a negative resist (XR-1541). Then, the electron-beam was used to transfer the pattern on the negative resist. Next, the unexposed areas of the resist were removed by developing the wafer in AZ® 300 metal-ion-free developer for four minutes. The exposed resist acted as a mask during the etching process. Chlorine plasma, which consists of $Cl_2$ and $BCl_3$, was used to etch the unprotected silicon. The mask was not removed after etching silicon because it acted as silicon oxide. Finally, the cylindrical rods structure was buried in silicon oxide of a thickness of 3000 nm, while the buried oxide under the air-holes was etched using a buffered oxide etchant solution for 10 minutes.

## 4.6 Experimental Results

We tested the fabricated “7 × 7” and “3 × 3” TE devices. The experimental measurement set up was as follows: the light from a tunable laser with spectral range from 1260 nm to

1520 nm propagated through a polarization controller to allow TE-like modes to couple into a 10 µm silicon waveguide. Coupling into and out of the silicon waveguides was achieved using tapered micro-lens fibers with a spot diameter of 2.5±0.5 micron. A J-coupler (see Figure 4.10(a)) [13] was fabricated and used to couple light from the 10 µm silicon waveguide into the 448 nm PC line-defect waveguide. Translational stages were used to align the input and output fibers to the device being tested. An infrared camera mounted on a microscope was used to capture the vertically scattered light from the waveguides. The output power was measured using an infrared detector and recorded using a power meter. A microscopic image of a cavity at resonance is shown in Figure 4.10(b).

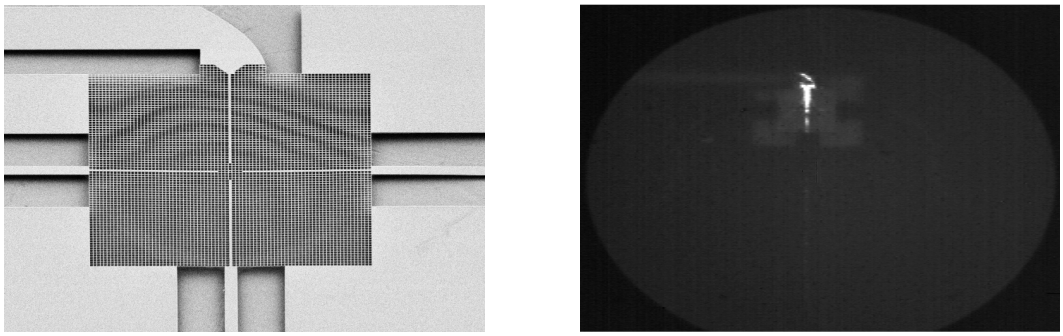

(a) (b)

Figure 4.10: Microscopic image of the (a) fabricated TE structure and (b) cavity at resonance.

A comparison between the experimental and simulation results of the "7 × 7" and "3 × 3" structures are shown in Figure 4.11. The Fabry Perot oscillations are formed by the reflection from the end-facets of the waveguides and the cavity. In our simulations, the light source, the output detector, and the crosstalk detector are all placed inside the PC line-defect waveguides. In our experiment, the light source and detector are out of the SOI chip. To be able to compare the simulation with the experiment, both results should be normalized to one. Also, the resonant frequency in both results should match. As

expected from simulation and theory, as the size of the cavity increases, the Q-factor and the crosstalk decreases. The Q-factor and crosstalk value for the fabricated "7 × 7" structure (see Figures 4.11(a and c)) is 168 and -20 dB and that of the "3 × 3" structure (see Figures 4.11(b and c)) is 54 and -10 dB. The measured Q-factors and crosstalk values are slightly different from that resulted from the numerical simulations. This is due to fabrication errors. From the plots in Figure 4.11, it is clear that the resonance frequency is shifted for the experimental results from that predicted by the simulation results. Based on the 2D simulation results, to get a shift in the resonance frequency from 1480 nm to 1345 nm requires that the widths of the fabricated square air-holes and defect be wider than that used in the simulation by about 5% (i.e., lattice constant is still the same (i.e., $a$ = 560 nm), square air-holes of a width of 0.842$a$, and a defect air-hole of a width of 0.642$a$). However, based on the measured values using the SEM for the tested "7 × 7" device (see Figure 4.11(d)), the measured widths of the bulk square air-holes and cavity defect are wider than that predicted by simulation by about 5% (i.e., lattice constant is still the same (i.e., $a$ = 560 nm), square air-holes of a width of 0.884$a$, and a defect air-hole of a width of 0.688$a$). The difference between the simulation and the measured values is because we performed a 2D simulation which does not take into consideration the out-of-plane effect. The measured spectrum of the throughput for the "7 × 7" cavity matches very well the simulation data, taking into account the shift of the resonance frequency, as shown in Figure 4.11(a). The measured spectrum of the throughput for the "3 × 3" cavity has the bandpass in the same range of frequencies but exhibited a narrower spectrum, a higher Q-factor (as shown in Figure 4.11(b)). This is very well expected because of the sensitivity of the devices due to any fabrication

tolerance. However, the fabrication error is not the same for both the defect air-hole and the bulk air-holes. As a result of that, the Q-factor of the fabricated "3 × 3" is higher than that of simulation which is evident in its wider spectrum. Practically speaking the throughputs of the devices were quite close to the simulation predictions. The crosstalk experimental curves show consistently that the "7 × 7" cavity has lower crosstalk values than that of the "3 × 3" as predicted by the simulation data. The crosstalk simulation results show stronger wavelength dependence than the experimental results, Figure 4.11(c), which is might be due in the major part to the low sensitivity and narrow dynamic range of the photodetector used in the experiment.

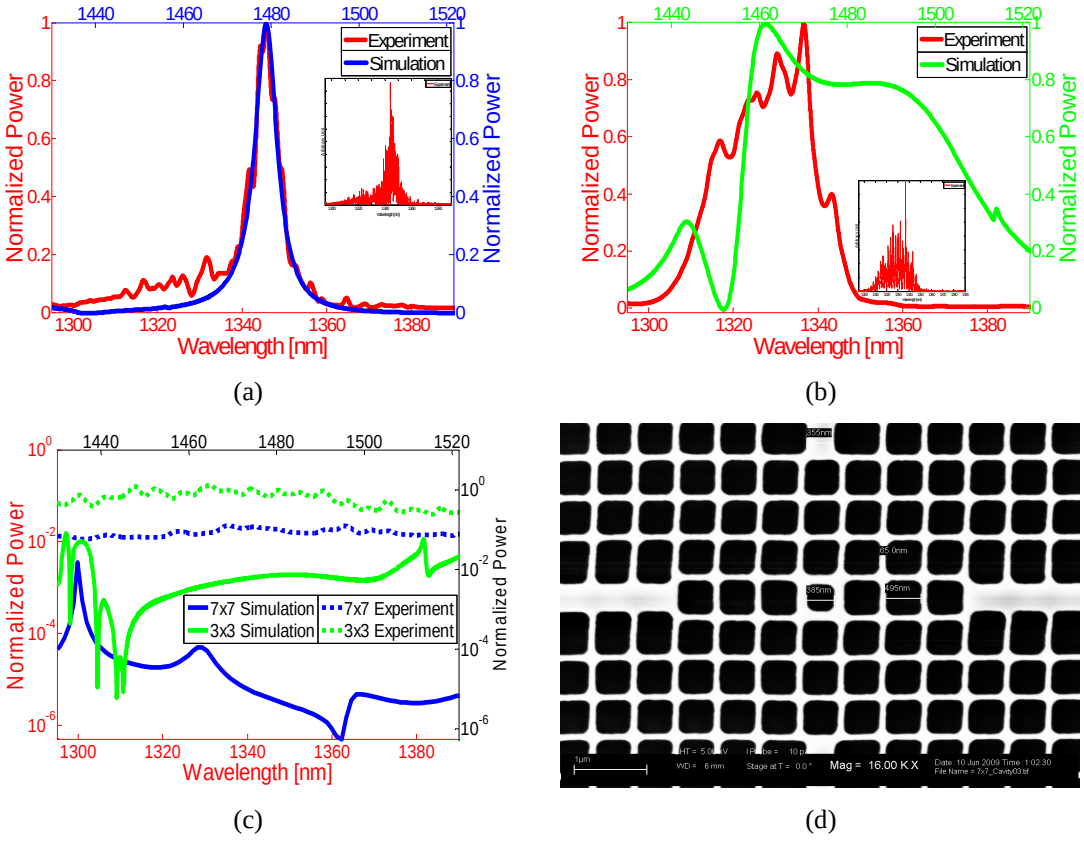


Figure 4.11: Comparison of experimental results with simulation results of (a) throughput "7 × 7" structure, (b) throughput "3 × 3" structure (the inset shows the unfiltered transmission measurements), (c) crosstalk for the "7 × 7" and "3 × 3" structures, and (d) SEM image of the tested "7 × 7" structure that shows the measured widths of the bulk and defect air-holes.

## 4.7 Summary

In this chapter, we demonstrated theoretically and experimentally that low crosstalk between two crossed line-defect waveguides formed in a square lattice photonic crystal (PC) structure can be achieved using a resonant cavity at the intersection area. The PC resonator consists of cubic air-holes in silicon. The quality-value of the cavity can be changed by increasing the number of holes that form the cavity. The theoretical and experimental crosstalk results are approximately -40 dB and -20 dB, respectively.

## References


[1] R. A. Wahsheh, M. A. G. Abushagur, and Z. Lu, “A method for cross talk reduction in crossed strip waveguides,” International Symposium on High Capacity Optical Networks and Enabling Technologies, HONET, November 2007, pp. 1-4.

[2] R. A. Wahsheh, M. A. G. Abushagur, Z. Lu, and S. F. Preble, “Cross talk reduction of nanophotonic crossed waveguides using a resonant cavity,” International Nanotechnology Conference, Jeddah, Saudi Arabia, November 2008.

[3] R. A. Wahsheh, Z. Lu, M. A. G. Abushagur, and S. F. Preble, “Ultra low cross talk in crossed strip waveguides with the assistance of a photonic crystal cavity,” Proceedings of SPIE - The International Society for Optical Engineering, vol. 7056, August 2008, pp. 70560E.1-70560E.8.

[4] R. A. Wahsheh, Z. Lu, S. F. Preble, and M. A. Abushagur, "Cross talk reduction by photonic crystal cavities", in Frontiers in Optics, OSA Technical Digest (CD) (Optical Society of America), October 2008, pp. FThK3.
http://www.opticsinfobase.org/abstract.cfm?URI=FiO-2008-FThK3

[5] R. A. Wahsheh, Z. Lu, and M. A. G. Abushagur, “Cross talk reduction in square cavities,” IEEE Photonics Journal, vol. 1, September 2009, pp. 191-196.

[6] R. G. Hunsperger, *Integrated Optics: Theory and Technology*. Berlin; New York: Springer-Verlag, 2002, ch. 7.

[7] W. Bogaerts, P. Dumon, D. V. Thourhout, and R. Baets, “Low-loss, low-cross-talk crossings for silicon-on-insulator nanophotonic waveguides,” Optics Letters, vol. 32, August 2007, pp. 2801-2803.

[8] S. G. Johnson, C. Manolatou, S. Fan, P. R. Villeneuve, J. D. Joannopoulos, and H. A. Haus, “Elimination of cross talk in waveguide intersections,” Optics Letters, vol. 23, December 1998, pp. 1855-1857.

[9] T. Liu, M. Fallahi, M. Mansuripur, A. R. Zakharian, and J. V. Moloney, “Intersection of nonidentical optical waveguides based on photonic crystals,” Optics Letters, vol. 30, September 2005, pp. 2409-2411.

[10] Y. G. Roh, S. Yoon, H. Jeon, S. H. Han, and Q. H. Park, “Experimental verification of cross talk reduction in photonic crystal waveguide crossings,” Applied Physics Letters, vol. 85, October 2004, pp. 3351-3353.

[11] S. H. G. Teo, A. Q. Liu, J. B. Zhang, and M. H. Hong, “Induced free carrier modulation of photonic crystal optical intersection via localized optical absorption effect,” Applied Physics Letters, vol. 89, August 2006, pp. 091910.1-091910.3.

[12] M. F. Yanik, S. Fan, M. Soljačić, and J. D. Joannopoulos, “All-optical transistor action with bistable switching in a photonic crystal cross-waveguide geometry,” Optics Letters, vol. 28, December 2003, pp. 2506-2508.

[13] D. W. Prather, J. Murakowski, S. Shi, S. Venkataraman, A. Sharkawy, C. Chen, and D. Pustai, “High-efficiency coupling structure for a single-line-defect photonic-crystal waveguide,” Optics Letters, vol. 27, September 2002, pp. 1601-1603.

[14] C. Manolatou, S. G. Johnson, S. Fan, P. R. Villeneuve, H. A. Haus, and J. D. Joannopoulos, “High-density integrated optics,” Journal of Lightwave Technology, vol. 17, September 1999, pp. 1682-1692.

# Chapter 5

# Silicon Microring Vertical Coupler

In this chapter, we propose a silicon microring coupler to couple light from a single mode fiber into a silicon-on-insulator waveguide. We also show the fabrication procedure and the experimental results for the optimized structure.

## 5.1 Introduction

Silicon-on-insulator (SOI) is one of the promising technologies suitable for monolithically integration of both electronic and optical circuits using conventional microelectronics patterning and fabrication techniques. In addition, this technology offers a high index contrast for strong light confinement in small dimensions and enables the miniaturization of functional integrated optical devices. On the other hand, the thickness of silicon guiding layer of a single mode SOI waveguide often shrinks to 100~200 nm for telecommunication wavelengths, whereas the diameter of a single mode fiber is about 10 μm. So there is huge mismatch between the mode size of a single mode fiber and that

of an SOI waveguide, resulting in a big challenge in efficiently coupling light into SOI waveguides and other semiconductor waveguides. Direct coupling, including end-fire coupling and butt coupling, has been shown to have a coupling efficiency approximately proportional to the mode dimension ratio [3,4]. Due to the diffraction limit of conventional optics, focusing a near infrared light beam to 100~200 nm is impractical or impossible and hence very low efficiency, 1~2%, is achievable. Other approaches, including grating coupling, prism coupling, and vertical tapering, were shown to be either difficult in fabrication or with poor efficiency. Taillaert *et al.* reported a 90° grating coupler for fiber-to-waveguide coupling [5]. The coupling efficiency was simulated to be 74% and experimentally measured to be 19%. Prism couplers and vertical tapers [6,7] were also reported, but they either require complex fabrication process or are difficult for integration. However, fiber-to-waveguide coupling is a basic issue to realize photonic chip-to-chip interconnection, especially for silicon photonic integration, where light emission is not easy to realize and optical signal and power often rely on the source from another chip through optical fiber. Inefficient fiber-to-waveguide coupling has greatly hampered the development and applications of photonic integrated circuits. Recently, some other novel couplers were also reported, including a tapered graded index structure [8], 45°-micromirrors [9], gray scaled parabolic mirror [10], dual-grating assisted directional coupler [11], and laser-induced fiber gratings [12]. However, none of the approaches provided efficiency high enough for practical fiber-to-SOI interconnection.

When light is coupled into an SOI waveguide, the coupling efficiency is essentially determined by how the profile of the input mode matches that of the SOI mode. In most cases, the mode match is very poor, resulting in a very low coupling efficiency in a single

coupling attempt. However, coupling efficiency can be improved if the coupler repeatedly feeds the uncoupled light into the waveguide-or makes “multiple attempts”. Recently, Lu proposed a coupler based on the vertical leakage from a microring, where light power is first fed into a microring—an “endless loop”, and the gradual leakage from the microring constitutes steady vertical coupling into the SOI slab [13]. In this coupler, gradual leakage forms numerous coupling attempts. Thus, very high coupling efficiency can be achieved. In addition, the coupler has the advantages of broad bandwidth, small dimensions, and easy integration. However, in order to achieve high efficiency, the refractive index of the microring has to be carefully controlled to match the effective index of the SOI waveguide mode. This may require growing exotic materials on the top of SOI. Herein, we propose an alternative structure where light can be coupled into SOI waveguides through a silicon microring [14]. In this structure, the effective index of a SOI waveguide mode is matched not by the refractive index of the microring but by the oblique incidence of light beam into the silicon microring. We also show the fabrication procedure and experimental results.

## 5.2 Silicon Microring Vertical Couplers

Figure 5.1(a) illustrates the principle of the coupler. The essential part of the coupler is a σ-shaped silicon microring on the top of an SOI slab. Once light is fed into the microring through the straight waveguide, it will circulate in an endless-loop until either scattered into the surrounding or coupled into the SOI slab at the bottom. The height of the microring waveguide, *H*, can be several microns while its width, *W*, needs to be controlled within 2~3 μm to excite long lateral evanescent tails. However, the straight

waveguide can be laterally tapered to several microns for matching the diameter of a single mode fiber. A buffer layer with thickness 50~100 nm is allowed (for fabrication consideration) between the microring and the SOI slab. As shown in Figure 5.1(b), the theory of operation is based on evanescent leakage, which requires the horizontal component of the wave vector in the microring matching that of the guided mode in the SOI slab, i.e., $K_{\text{ring}} \sin\Theta_{\text{ring}} = \beta_{\text{SOI}}$. Note that the refractive index of the microring and the SOI guiding layer is the same. Thus, the propagation angle inside the microring needs to be equal to the SOI waveguide mode angle, $\Theta_{\text{ring}} \approx \Theta_{\text{mode}}$. In practice, $\Theta_{\text{ring}}$ should be slightly larger than $\Theta_{\text{mode}}$. For example, the mode angle of a 300-nm-SOI slab at $\lambda_o$ = 1550 nm is $\Theta_{\text{mode}}$(TE) = 61° for the TE mode and $\Theta_{\text{mode}}$(TM) = 48° for the TM mode. So in order to efficiently couple light (at $\lambda_o$ = 1550 nm) from the microring into the SOI slab, $\Theta_{\text{ring}}$ should be slightly larger than 61° and 48° for TE and TM modes, respectively. There are two approaches to excite the desired propagation direction inside the microring: oblique incidence as inset 1 and parallel incidence as inset 2 of Figure 5.1(a). In these two cases, the input port should be polished with different slope angles: $\alpha_1 = \Theta_{\text{mode}}$ and $\alpha_2 = \tan^{-1}\left[(\sin\Theta_{\text{mode}} - n_{\text{fiber}}/n_{\text{ring}})/\cos\Theta_{\text{mode}}\right]$ (about 43° for 1550 nm-TE mode coupling), where $n_{\text{fiber}}$ and $n_{\text{ring}}$ are the refractive indices of the optical fiber and silicon, respectively.

In the simulation, we used the second approach with the slope angle $\alpha_2$ = 47° (slightly larger than $\tan^{-1}\left[(\sin\Theta_{\text{mode}} - n_{\text{fiber}}/n_{\text{ring}})/\cos\Theta_{\text{mode}}\right]$) for TE-mode coupling. For simplicity, the profile of the fiber is assumed to be rectangular to match that of the input port waveguide. The thickness of the silicon guiding layer is 300 nm with a 50-nm thick $SiO_2$ buffer layer

on the top. The microring is formed by a silicon waveguide ($n_{ring} = 3.5$) with width $W = 2.0$ μm and height $H = 2.5$ μm. The diameter of the microring measured from the center of the waveguide is $R = 5.0$ μm. The thickness of the SOI substrate ($SiO_2$) and the air layer on the top of the microring is assumed to be infinite, but taken 0.5 μm in the simulation. The whole structure is surrounded by the perfectly-matched-layer. A monochromatic source with Gaussian beam profile and size 1.5 μm × 1.8 μm is placed at the center of the optical fiber. The index of refraction of the fiber is assumed to be $n_{fiber} = 1.5$. The electric field component of the source is along the y-direction, and magnetic field along the z-direction, i.e., $\mathbf{E} = E_y\hat{\mathbf{y}}$ and $\mathbf{H} = H_z\hat{\mathbf{z}}$.

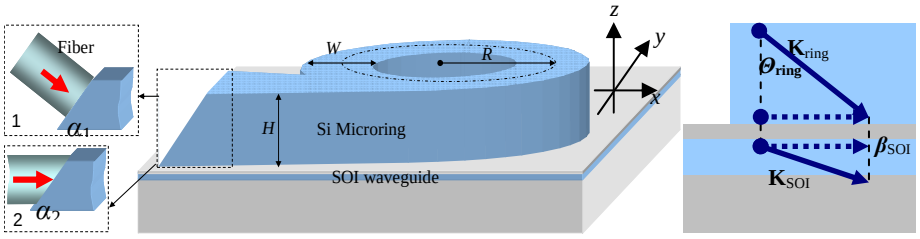


(a) (b)

Figure 5.1: (a) The illustration of the silicon microring vertical coupler. (b) The illustration of the theory of operation.

Figure 5.2 shows the simulated field distribution for the amplitude of the main component, $H_z$, using the 3D finite-difference time-domain (FDTD) method [15]. The top surfaces in Figure 5.2(a and b) go through the half height of the microring, while Figure 5.2(c and d) shows the light emission through the surfaces of the simulated cube. As can be seen, there is no obvious guiding route for the fed power propagate out of the microring but to leak into the SOI guiding layer or to be radiated into the surrounding media, and most of the power is coupled into the SOI guiding layer. Note the straight waveguide section contains a joint of the optical fiber and silicon waveguide as shown in

the inset 2 of Figure 5.1(a). According to the simulation, small amount of power is reflected at the interface between the optical fiber and the input port. Theoretically, the ratio runs up to 21%, which can be greatly decreased by integrating a suitable anti-reflection coating.

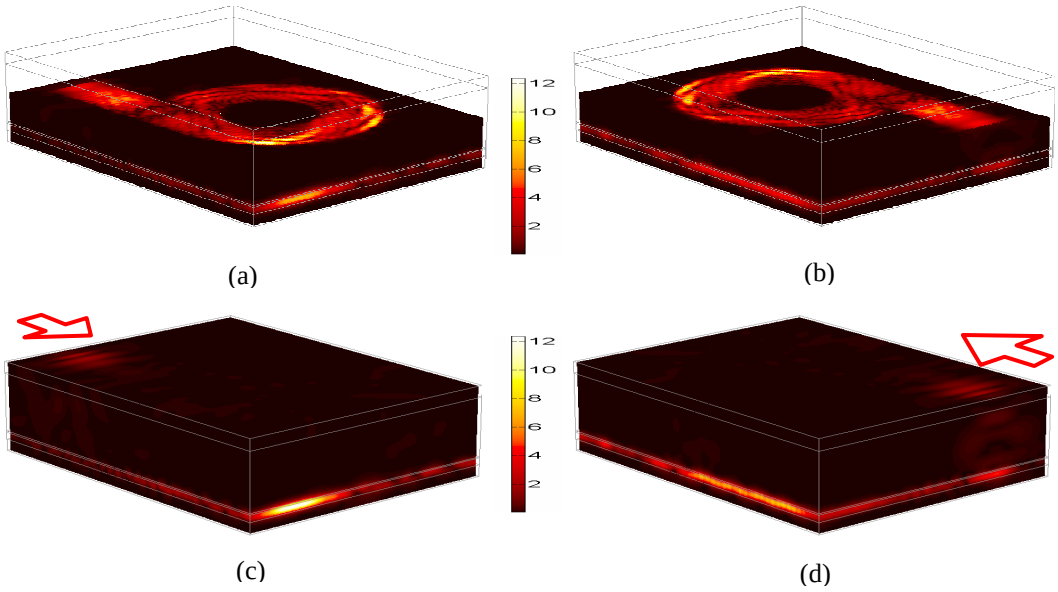


Figure 5.2: The simulated field distribution ($H_z$) for different perspectives. The arrow in each panel indicates the input light propagation direction.

The ratio between the power propagating out from the guiding layer and the total power sent out from the cubic boundaries is calculated to be 72%. The guided power confined in the substrate and cladding layer as evanescent waves is estimated from the theoretical mode profile. Excluding the reflection between the optical fiber and the input port, the coupling efficiency is calculated to be 91% at $\lambda_o$ = 1550 nm. Note there is still a mode profile mismatch at the interface between the optical fiber and the input port. The coupling efficiency can be further improved. The bandwidth was simulated to be huge in [13]. This can be explained by the small modification in the effective index of the SOI slab with different working wavelengths.

As partially discussed in [13], the coupling efficiency is determined by the comparison of the coupling time and photon lifetime in the microring. As shown in the inset 1 of Figure 5.3(a), the index profile in the vertical direction across the waveguide shows the coupling system is essentially a 3D dielectric waveguide overlapping a 3D loaded SOI waveguide. The shadowed part has a larger effective index due to the upper dielectric loading and thus the light coupled from the dielectric waveguide can be confined in the SOI waveguide. However, the lateral confinement in the SOI waveguide is very poor because the index contrast due to the upper dielectric loading is very small. When both the dielectric waveguide and SOI waveguide are curved to form two overlapped microrings, the SOI waveguide looses power much faster than the dielectric waveguide. This can be understood through the confinement width $X_r = [(n_{\text{eff}} / n_{\text{sur}}) - 1]R$, beyond which light is radiated into the surrounding medium [16]. The attenuation coefficient due to radiation loss takes the form $\alpha \propto C_1 \exp(-2\gamma X_r)$, where $\gamma$ is the extinct factor of a guided mode, and $C_1$ is a constant related to the mode profile. The SOI waveguide has smaller extinct factor $\gamma$ and smaller confinement width $X_r$ than the dielectric waveguide. As a result, the leakage through the loaded SOI waveguide dominates. Due to the tiny effective index difference, most leakage becomes the guided light in the SOI slab. However, this analysis is based on the assumption that propagating mode can be excited in the 3D SOI waveguide. When the bulk index of the dielectric waveguide or $\Theta_{\text{ring}}$ is too small or too large, only evanescent waves can be excited in the 3D loaded SOI waveguide and light cannot be coupled into the SOI slab.

## 5.3 Light Propagation Direction Control in the SOI Waveguide

The lateral mode size conversion in the SOI waveguide can be realized using a tapered waveguide or a parabolic surface [17]. In [13], Lu demonstrated a complementary SOI microring with overall coupling efficiency of 72%. The coupling efficiency can be further improved and the semi-disk structure as illustrated in Figure 5.3(a) is such an example. One end of the SOI waveguide is first fabricated as a semi-disk, as shown in the inset 2 of Figure 5.3(a), and the input port of the microring coupler is aligned to the disk part of the waveguide. The confinement imposed by the semi-disk allows the coupled waveguide only propagating forwards. To validate the design, the simulation is repeated by applying the SOI semi-disk in the guiding layer. As shown in Figure 5.3(b), most of light power is coupled into the SOI waveguide, and the coupling efficiency is calculated to be 87%, which is slightly lower than the efficiency, 91%, for coupling into a blank SOI slab. The output of the semi-disk is essentially broad guided modes and there are mature techniques available to taper them into a single mode.

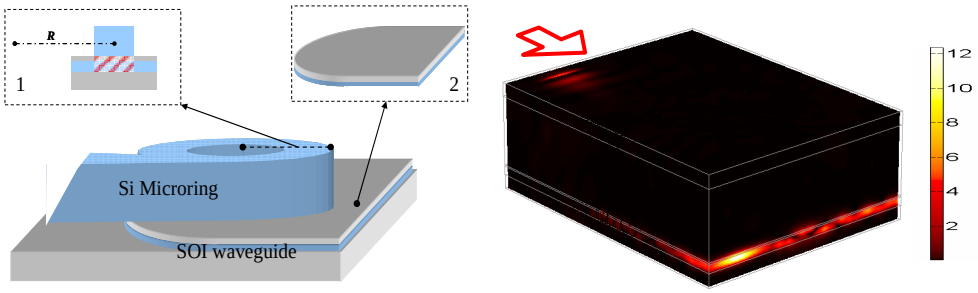


(a) (b)

Figure 5.3: (a) The illustration of the device to control the coupling direction. (b) The simulation of light propagation direction in the SOI waveguide. The arrow indicates the input light propagation direction.

## 5.4 Fabrication Process

Two electron-beam lithography steps were required to fabricate the structure shown in Figure 5.1. One lithography step was done to define the top Si waveguide and another one to define the lower SOI waveguide. Three fabrication challenges were involved: one was to use the negative electron-beam resist (XR-1541 22%) as a mask to define the top waveguide, another was to use the negative electron-beam resist (XR-1541 6%) as a mask to define the bottom waveguide, and the third was to align the bottom waveguide with respect to the top waveguide. We were able to overcome all of these challenges. To define the top waveguide, the silicon layer should be lower than 2 μm so that the exposed XR-1541 22% can protect the underneath structure during the etching process. We also post baked the resist for four minutes before immersing it in the MIF developer to harden the exposed resist. To define the SOI waveguide, the thickness of the XR-1541 6% should be about 150 nm to protect both the top waveguides and the SOI waveguides during the etching process. The alignment tolerance between the ring coupler and the SOI waveguide was ±3 μm.

To fabricate the vertical ring coupler, a buffered oxide layer of a height of 80 nm was deposited on top of the SOI wafer. Then Si layer of a height of 1650 nm was deposited. The wafer was spun coated with a negative resist (XR-1541 HSQ 22%) to fabricate the Si waveguide. The electron-beam was used to transfer the pattern on the negative resist. The exposed resist acted as a mask during the etching process. Chlorine plasma was used to etch the unprotected silicon. The remaining mask was not removed after etching silicon because it is still needed to protect the top fabricated waveguide while etching the bottom SOI-waveguides. To fabricate the SOI waveguide, the wafer was spun coated with a

negative resist (XR-1541 HSQ 6%). The electron-beam was used to transfer the pattern on the negative resist. Next, the unexposed areas of the resist were removed by developing the wafer in MIF developer for four minutes. Chlorine plasma was used to etch the unprotected silicon. Figure 5.4 shows the microscopic image of the microring coupler after the first and second electron-beam lithography steps.

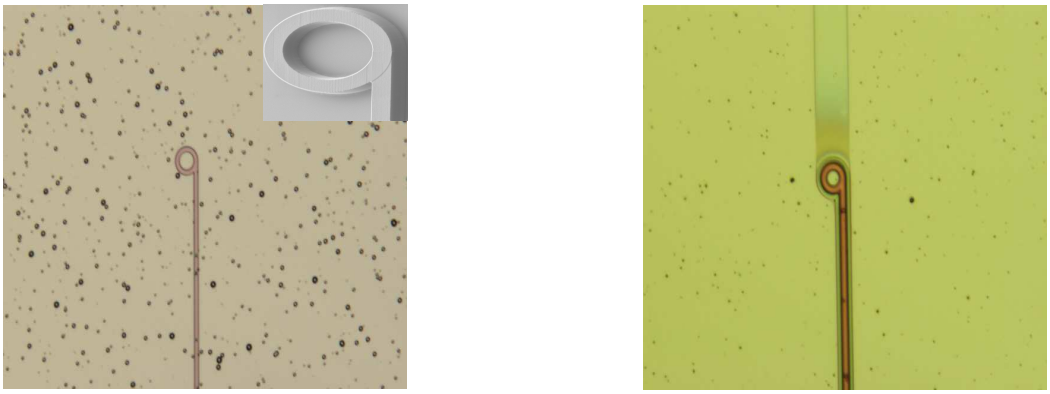

(a) (b)

Figure 5.4: Microscopic image of the microring coupler after the (a) first and (b) second electron-beam lithography steps.

## 5.5 Experimental Results

We tested the fabricated microring structures (see Figure 5.5(a)). The experimental measurement set up was as follows: the light from a tunable laser with spectral range from 1520 nm to 1620 nm propagated through a polarization controller to allow TM-like modes to couple into a 2 µm silicon waveguide. Coupling into and out of the silicon waveguides was achieved using tapered micro-lens fibers with a spot diameter of 2.5±0.5 micron. Translational stages were used to align the input and output fibers to the device being tested. An infrared camera mounted on a microscope was used to capture the vertically scattered light from the waveguides. The output power was measured using an infrared detector and recorded using a power meter. A microscopic image of the

scattered light from the microring coupler and the SOI waveguide is shown in Figure 5.5(b). Our reference waveguide was a straight SOI waveguide of a width of 2 µm. The measured spectrum of the fabricated vertical microring coupler has a trend similar to that of the reference waveguide, but it exhibited a narrower spectrum (see Figure 5.5(c)). It was about 40 nm for the coupler and 70 nm for the reference waveguide (measured within the spectral range understudy). This is very well expected because of the sensitivity of the devices due to any fabrication tolerance. We designed the coupler to have an alignment tolerance of ±3 µm between the top waveguide (i.e., microring coupler) and the bottom waveguide (i.e., SOI waveguide). Consequently, the width of the SOI waveguide under the microring coupler was about 18 µm. The 18 µm SOI waveguide was tapered down to 2 µm over a length of about 3 mm, which caused propagation losses higher than that in the reference waveguide. Also, the thickness of the oxide layer between the microring coupler and the SOI waveguide is somewhat thick (80 nm). This prevented more light from coupling into the SOI waveguide. The coupling efficiency of the vertical coupler can be increased by fabricating the structure in which the following conditions are met: the width of the SOI waveguide is reduced at the overlap area to about 13 µm (i.e., alignment tolerance is ±0.5 µm), the tapering length of the SOI waveguide is about 1 mm, and the thickness of the deposited oxide is reduced to about 50 nm.

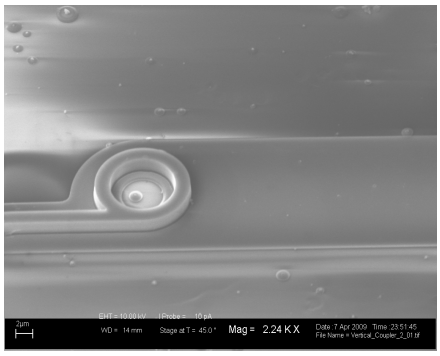

(a)

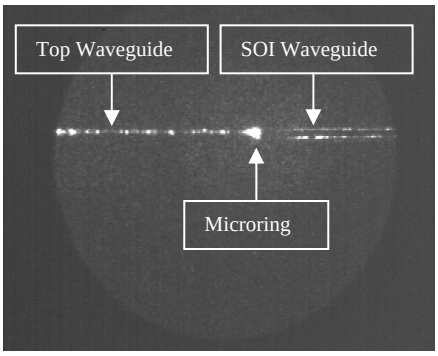


(b)

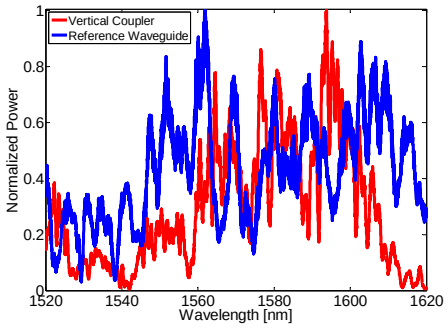


(c)

Figure 5.5: Coupling measurement between the microring coupler and SOI waveguide: (a) SEM image of the fabricated coupler, (b) a microscopic image of the scattered light from the coupler, and (c) coupling efficiency as a function of wavelength for TM polarization.

## 5.6 Summary

In this chapter, we showed theoretically and experimentally that a vertical microring coupler can be used to increase the coupling efficiency between a conventional optical waveguide and silicon-on-insulator waveguide.

## References

[1] H. Rong, R. Jones, A. Liu, O. Cohen, D. Hak, A. Fang, and M. Paniccia, “A continuous-wave Raman silicon laser,” Nature, vol. 433, February 2005, pp. 725-728.

[2] A. W. Fang, H. Park, O. Cohen, R. Jones, M. J. Paniccia, and J. E. Bowers, "Electrically pumped hybrid AlGaInAs-silicon evanescent laser," Optics Express, vol. 14, October 2006, pp. 9203-9210.

[3] A. Yariv, "Coupled-mode theory for guided-wave optics," IEEE Journal of Quantum Electronics, vol. 9, September 1973, pp. 919-933.

[4] R. G. Hunsperge, A. Yariv, and A. Lee, "Parallel end-butt coupling for optical integrated circuits," Applied Optics, vol. 16, April 1977, pp. 1026-1032.

[5] D. Taillaert, W. Bogaerts, P. Bienstman, T. F. Krauss, P. Van Daele, I. Moerman, S. Verstuyft, K. De Mesel, and R. Baets, "An out-of-plane grating coupler for efficient butt-coupling between compact planar waveguides and single-mode fibers," IEEE Journal of Quantum Electronics, vol. 38, July 2002, pp. 949-955.

[6] Z. Lu and D. W. Prather, "Total internal reflection-evanescent coupler for fiber-to-waveguide integration of planar optoelectronic devices," Optics Letters, vol. 29, August 2004, pp. 1748-1750.

[7] A. Sure, T. Dillon, J. Murakowski, C. Lin, D. Pustai, and D. W. Prather, "Fabrication and characterization of three-dimensional silicon tapers," Optics Express, vol. 11, December 2003, pp. 3555-3561.

[8] S. Janz, B. Lamontagne, A. Delage, A. Bogdanov, D-X. Xu, and K. P Xu, "Single layer a-Si GRIN waveguide coupler with lithographically defined facets," 2nd IEEE International Conference on Group IV Photonics, September 2005, pp 129-131.

[9] C. Choi, Y. Liu, L. Lin, L. Wang, J. Choi, D. Haas, J. Magera, and R.T. Chen, "Flexible optical waveguide film with 45-degree micromirror couplers for hybrid

E/O integration or parallel optical interconnection," Proceedings of SPIE - The International Society for Optical Engineering, vol. 5358, July 2004, pp. 122-126.

[10] T. Dillon, C. Chen, J. Murakowski, and D. Prather, "Efficient fiber to waveguide coupling structure for optical systems integration using grayscale lithography," Proceedings of SPIE - The International Society for Optical Engineering, vol. 6478, February 2007, pp. 64780O.1-64780O.9.

[11] G. Z. Masanovic, G. T. Reed, W. Headley, B. Timotijevic, V. M. N. Passaro, R. Atta, G. Ensell, and A. G. R. Evans, "A high efficiency input/output coupler for small silicon photonic devices," Optics Express, vol. 13, September 2005, pp. 7374-7379.

[12] A. L. Bachim, O. O. Ogunsola, and T. K. Gaylord, "Optical-fiber-to-waveguide coupling using carbon-dioxide-laser-induced long-period fiber gratings," Optics Letters, vol. 30, August 2005, pp. 2080-2082.

[13] Z. Lu, "Efficient fiber-to-waveguide coupling through the vertical leakage from a microring," Optics Letters, vol. 32, October 2007, pp. 2861-2863.

[14] R. A. Wahsheh, Z. Lu, Jun Yang, and M. A. G. Abushagur, "Silicon microring vertical coupler," International Symposium on High Capacity Optical Networks and Enabling Technologies, HONET, December 2009, pp. 280-283.

[15] A. Taflove and S. C. Hagness, *Computational Electrodynamics: the Finite-Difference Time-Domain Method*. Massachusetts: Artech House Inc., 2000.

[16] R. G. Hunsperger, *Integrated Optics: Theory and Technology*. Berlin; New York: Springer-Verlag, 2002, ch. 8.

[17] D. W. Prather, J. Murakowski, S. Shi, S. Venkataraman, A. Sharkawy, C. Chen, and D. Pustai, “High-efficiency coupling structure for a single-line-defect photonic-crystal waveguide,” Optics Letters, vol. 27, pp. 1601-1603, September 2002.

# Chapter 6

# Nanoplasmonic Photonic Devices

In this chapter, we introduce a novel design and analysis of an ultra-compact coupler, a 1 × 2 splitter, a directional coupler, and a Mach-Zehnder interferometer from silicon waveguides into plasmonic waveguides with high coupling efficiency, flexible splitting ratios, and broad bandwidth [1-5]. The fabrication procedure and the experimental results for a coupler and a 1 × 2 splitter are shown.

## 6.1 Introduction

Recent interest arises in plasmonic waveguides, which promise to play an important role in minimizing the footprint required to integrate multiple optoelectronic devices on the same chip. In particular, plasmonic waveguides formed by metal-dielectric-metal (MDM) structures can tightly confine light in the dielectric region on deep sub-wavelength scales [6,7] which is not possible using conventional dielectric waveguides due to diffraction limit [8]. However, the smaller the modal size in the dielectric region of the MDM, the larger the propagation loss due to the metallic losses. The tradeoff between mode

confinement and propagation loss can be addressed by integrating both dielectric waveguides and plasmonic waveguides in the same system. To this end, efficient coupling between dielectric waveguides and plasmonic waveguides is of great significance.

It is necessary to use dielectric waveguides to connect the plasmonic devices to the light source and detector so that the propagation losses due to the metallic interaction are dramatically reduced. To achieve that, several different coupling methods have been proposed to increase the coupling efficiency from a dielectric waveguide into a plasmonic waveguide, such as direct coupling [9], multi-section taper [9], λ/4 coupler [10], adiabatic tapered coupler [11], and nonadiabatic tapered coupler [11,12]. Also several different optical circuit elements and devices such as: T- and Y-shape splitters [13-17], directional couplers [18-21], and Mach-Zehnder interferometers (MZIs) [18,19] have been proposed. Our proposed optical circuit elements are compact and efficient in which we were able to overcome many of the problems that were reported in the literature that made the reported optical elements have large sizes. In Y-junctions, the radius of curvature plays an important role in reducing radiation losses and increasing the size of the fabricated devices [13,14]. In T-junctions, the intersection area should be designed to increase the coupling efficiency and reduce back reflection. Coupling efficiency can be increased using a resonant cavity at the intersection area [15], using photonic crystal waveguides [16], or using plasmonic waveguides [17]. Directional couplers are used in many applications such as splitters [18-20], switches [19], and wavelength sorters [21]. The size of the directional coupler depends on the separation distance between the two adjacent waveguides, widths of the waveguides, the refractive index of the waveguides,

the refractive index of metal, and the operating wavelength. Zia *et al.* [22] found that negligible crosstalk between adjacent two MDM waveguides occurs when the separation distance between the two waveguides is greater than 150 nm at the free space wavelength $\lambda_o = 1.55$ μm. Traditional dielectric directional couplers are used as splitters in which there is a $90^o$ phase shift between the two split beams. A different phase behavior occurs in MDM directional couplers in which the phase difference between the two split beams is lower than $90^o$ [18]. Wang and his co-worker [18] attribute this phase behavior to the interaction of the field with the complex refractive index of metal. Unlike the traditional dielectric directional couplers, the plasmonic directional couplers have wavelength coupling dependence [20,21] because the real part of the complex refractive index of metal changes as wavelength changes. Connecting two splitters or two directional couplers back-to-back results in a MZI [18,19]. Connecting two splitters resulted in back reflection in [18], while connecting two directional couplers resulted in a compact structure in [18] and long MZI in [19].

A recent numerical simulation demonstrated a coupling efficiency of 68% by directly coupling light from a 300 nm wide silicon waveguide into a 40 nm silver-air-silver plasmonic waveguide [9]. Coupling efficiency was further improved to 93% by using a multi-section taper of a length of 400 nm, which was designed by a genetic global optimization algorithm and analyzed with a finite-difference frequency-domain methodology. In this work, we propose a direct yet efficient short plasmonic coupler of a length of 33 nm to increase the coupling efficiency between a silicon waveguide and a silver-air-silver plasmonic waveguide. Based on the coupler, we also propose a splitter that delivers light from a silicon waveguide into two plasmonic waveguides. To the best

of our knowledge, this is the first time that one reports a 1 × 2 splitter from a silicon waveguide into two MDM plasmonic waveguides. Then, two potential applications of the coupler and splitter are presented. One is a directional coupler and the other one is a MZI. First, we designed a coupler at the interface between the silicon and plasmonic waveguide. Then, we described how a 3-dB splitter, a directional coupler, and a MZI could be designed. The coupling efficiency and the spectrum response of all devices are investigated using the finite-difference time-domain method with a uniform mesh size of 1 nm to accurately capture the change of the field at the interface between the dielectric waveguide and the plasmonic waveguide. The fundamental transverse magnetic mode is excited in the single-mode dielectric waveguide and the transmitted power is measured by a power monitor that is placed close to the interface with the plasmonic waveguide [9]. Then, the coupling efficiency is calculated by normalizing the transmitted power with respect to the input power. The perfectly matched layer is used to attenuate the field within its region without back reflection. The metal losses are included in our simulations and the relative permittivity of the silver at the free-space wavelength $\lambda_o = 1.55$ μm using the commercial software FullWAVE from RSOFT is -103.7+8.1j.

## 6.2 Design and Numerical Results

In order to validate our results, we started by simulating the coupler proposed by Veronis and Fan [9] and obtained the same coupling efficiency (68%) by directly coupling light from a 300 nm wide silicon waveguide into a 40 nm silver-air-silver plasmonic waveguide. By analyzing the numerical results, it is obvious that the light wave from the dielectric waveguide excites surface plasmon polaritons (SPPs) along the dielectric-

plasmonic boundaries and the SPPs will be “funneled” into the MDM plasmonic waveguides. This funneling process can conceptually explain why light can be efficiently coupled from a large (300 nm) dielectric waveguide into a tiny (40 nm) dielectric slot MDM waveguide. We found that the coupling efficiency can be greatly improved simply by incorporating a rectangular air-gap (i.e., slot waveguide) and hence preventing transverse “funneling leakage” at the interface between the dielectric waveguide and the MDM plasmonic waveguide [1-3]. Herein, we present the design steps and numerical results for the proposed air-gap couplers (AGC) and nanoplasmonic devices.

### 6.2.1 Air-Gap Coupler Design

First, we consider an ultra-short matching rectangular AGC inside the plasmonic waveguide at the interface with silicon, as shown in Figure 6.1(a). In the two dimensional (2D) simulation, we varied the dimensions of the coupler and measured the corresponding coupling efficiency. The dependence of the coupling efficiency on the coupler’s width $W$ and length $L$ is shown in Figure 6.1(b). We found that coupling efficiency had a maximum value when $W$ matches the width of the silicon waveguide. In particular, the coupling efficiency is above 87.7% for 30 nm < $L$ < 40 nm and is maximized for $L$ = 33 nm (coupling efficiency = 88.1%). Tapering the edges of the rectangular AGC can further increase the coupling efficiency to 90% [1], but doing so will also increase the fabrication complexity. In this work, we only consider the rectangular AGC and optimize its length as 40 nm to match that of the width of the plasmonic waveguide. The field distribution of the coupled light for the rectangular AGC is shown in Figure 6.1(c).

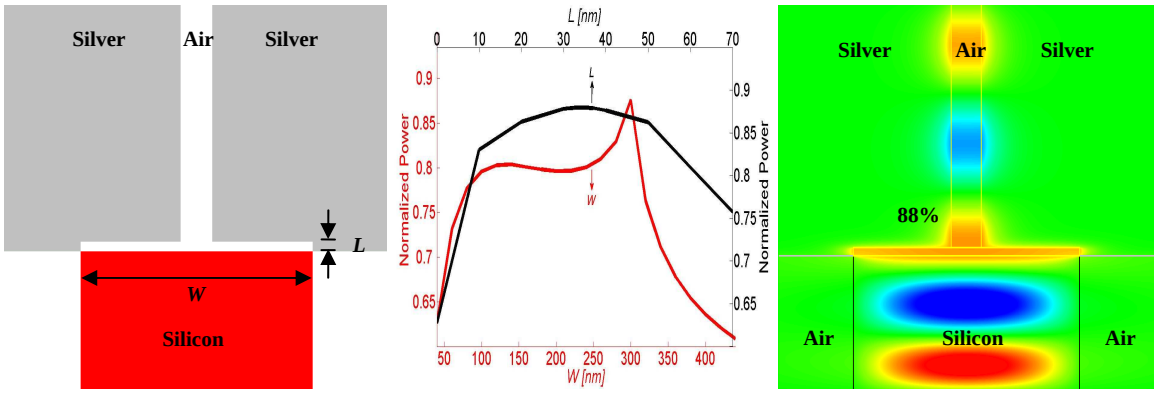


(a) (b) (c)

Figure 6.1: (a) Schematic of the basic proposed coupler. (b) Coupling efficiency as a function of the coupler's width *W* and length *L*. (c) Field distribution of the coupled light at $\lambda_o$ = 1.55 µm for the air-gap coupler.

Veronis and Fan [9] found that to maximize the coupling efficiency between the dielectric waveguide and the plasmonic waveguide, there is an optimal width of the dielectric waveguide for a given width of the plasmonic waveguide. As shown in Figure 6.2, the optimal width of the dielectric waveguide is 300 nm when the width of the plasmonic waveguide is 40 nm. We found that this dependency is broadened when using our proposed AGC. Increasing the size of the dielectric waveguide from 300 nm to 500 nm resulted in a decrease in the coupling efficiency by about 15% as opposed to 45% for the case without using the AGC.

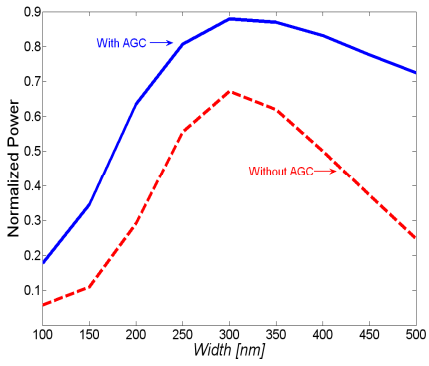


Figure 6.2: Coupling efficiency for the basic structure (Figure 6.1(c)) as a function of the dielectric waveguide's width.

Moreover, our coupler allows for considerable alignment tolerance, which is necessary for practical applications since accurately aligning the silicon waveguide to the plasmonic waveguide is a difficult task. To evaluate the effect of the misalignment, two configurations are examined. One is for the misalignment of both the MDM waveguide and the AGC with respect to the silicon waveguide as a function of the displacement $d_1$ (as shown in Figure 6.3(a)). Another is for the misalignment of the MDM waveguide with respect to both AGC and silicon waveguide as a function of the displacement $d_2$ (as shown in Figure 6.4(a)). The misalignment in both cases is exaggerated in order to show the effect of using the AGC. Figures 6.3(b) and 6.4(b) show the coupling efficiency with and without using the AGC as a function of the displacement $d_1$ and $d_2$, respectively. We found that the misalignment tolerance is much higher for both cases when using the AGC. For example, if the plasmonic waveguide center is at the edge of the silicon waveguide (i.e., $d_1$ = 150 nm) as shown in Figure 6.3(a), the coupling efficiency is 1% without using the AGC and 26% when the AGC is used. In another example, if the MDM waveguide is placed next to the AGC (i.e., $d_2$ = 170 nm) as shown in Figure 6.4(c), then coupling efficiency is negligible without using the AGC and 41% when the AGC is used. Note that there is almost no alignment overlap between the dielectric waveguide and the MDM plasmonic waveguide. From this analysis, it is obvious that in order to achieve high coupling efficiency, the AGC's edges should be aligned to the silicon waveguide edges and the MDM waveguide should be placed at the center of the silicon waveguide.

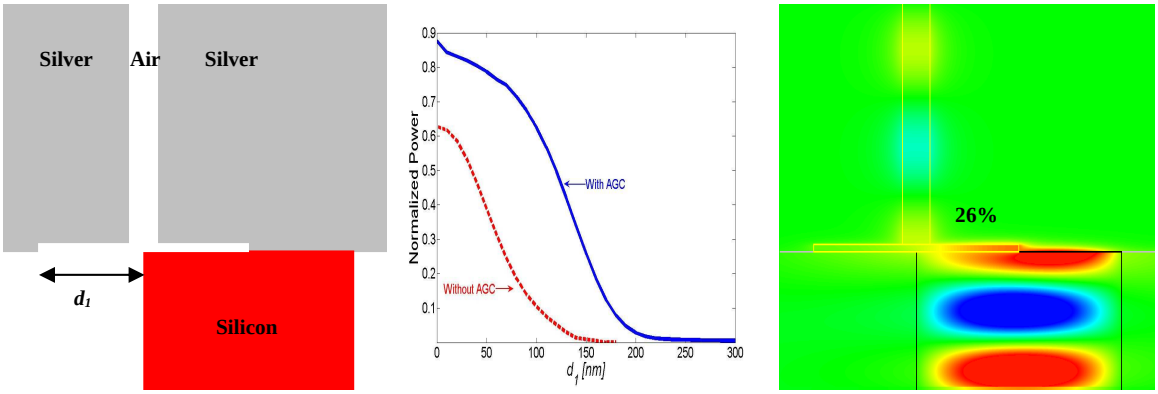


(a) (b) (c)

Figure 6.3: (a) Schematic of the position misalignment $d_1$ between the silicon waveguide and the plasmonic waveguide with the AGC connected to it. (b) Coupling efficiency as a function of $d_1$. (c) Field distribution for the structure shown in Figure 6.3(a) when $d_1$ = 150 nm.

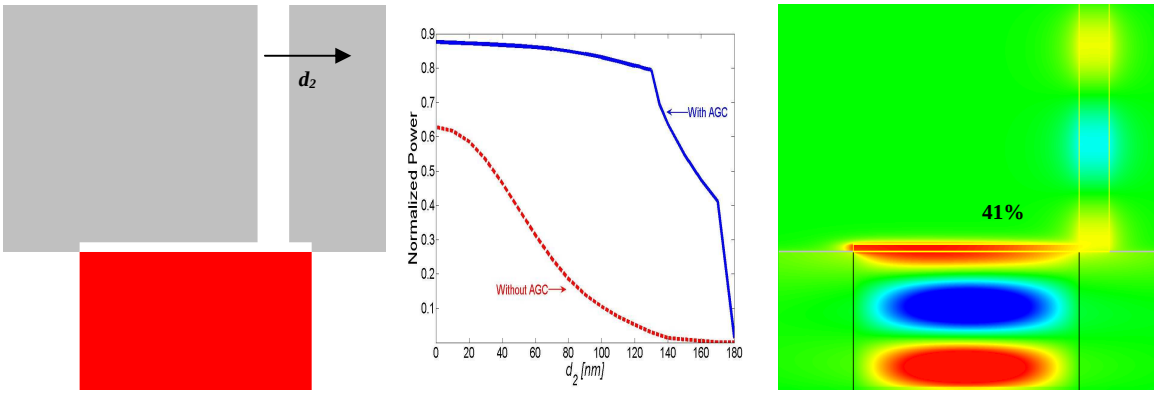


(a) (b) (c)

Figure 6.4: (a) Schematic of the position misalignment $d_2$ between the silicon waveguide with the AGC connected to it and the plasmonic waveguide. (b) Coupling efficiency as a function of $d_2$. (c) Field distribution for the structure shown in Figure 6.4(a) when $d_2$ = 170 nm.

In our couplers, the rectangular air-gap plays an important role in increasing both the coupling efficiency (as shown in Figure 6.1) and improving the alignment tolerance of the plasmonic waveguide with respect to the dielectric waveguide (as shown in Figures 6.3 and 6.4). To verify this, we made several additional simulations and found that without using the AGC the plasmonic mode was excited at the interface between metal and silicon that had a different mode size than that of the MDM waveguide. After using the AGC, the plasmonic mode size matched that of the MDM waveguide because the AGC formed a cavity between the metal and silicon, which enabled more power to

couple into the MDM waveguide. When the AGC does not have the same width as that of the silicon waveguide, the SPP excitation starts from the area that is not covered with the AGC. Then the SPP is coupled inside the AGC and propagates towards the MDM waveguide and couples into MDM waveguide, as shown in Figure 6.5(a). When the AGC covers the whole silicon area and the MDM waveguide is at the center, as shown in Figure 6.5(b), the SPP excitation starts at an equal distance from the MDM waveguide and then is coupled into the MDM waveguide. When the MDM waveguide is not at the center, SPP excitation starts away from the MDM waveguide before it is coupled into the MDM waveguide (Figure 6.5(c)). This proves that the MDM waveguide introduces transverse metal boundaries that prevent the transverse leakage of SPPs and consequently increases the coupling efficiency.

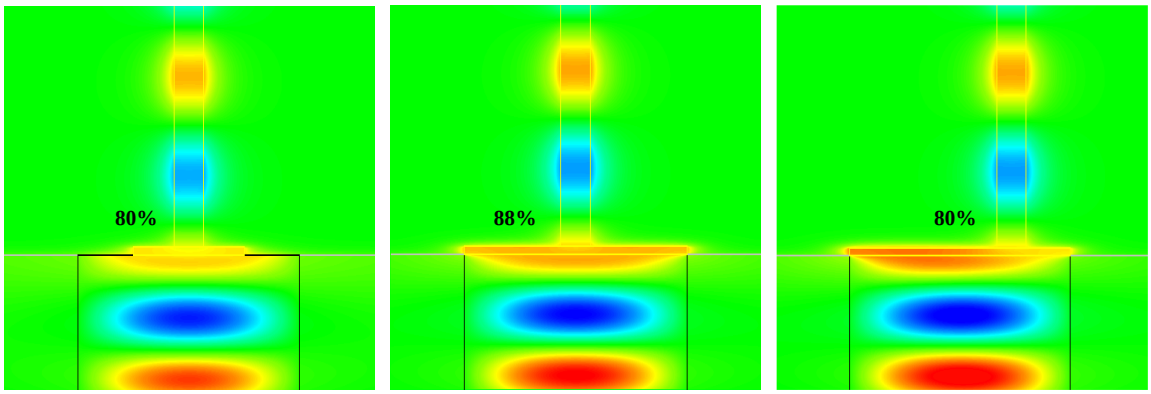


(a) (b) (c)

Figure 6.5: The electric field distribution when (a) the width of the AGC does not match that of the silicon waveguide, (b) the width of the AGC matches that of the silicon waveguide and the MDM waveguide is at the center, and (c) the width of the AGC matches that of silicon waveguide and the MDM waveguide is not at the center.

We can further explain why one structure has higher coupling efficiency than another. For example, the coupling efficiency for the structure shown in Figure 6.1(c) has the highest coupling efficiency (about 88%) because the SPP excitation starts at equidistance from both sides of the centered MDM waveguide and are “funneled” into the MDM

waveguide. In another example, the coupling efficiency for the structure shown in Figure 6.5(a) is lower than that for the structure shown in Figure 6.1(c) because part of the excited SPP propagates away from the AGC and also the excited SPP mode at the interface between silicon and metal travels towards the AGC, which has a different dielectric material (i.e., air). On the other hand, when the width of the AGC is higher than that of the silicon waveguide, the AGC does not act as a cavity because the bottom of the extra length is terminated by air and not by silicon. Thus, the coupling efficiency dropped dramatically.

### 6.2.2 Splitter Design

Ultra compact splitters are required in nanophotonic circuits in order to minimize the required area to produce multiple photonic devices on the same chip. The coupler introduced in Section 6.2.1 can be easily used to design splitters. In this section, two methods were used to design splitters: one method by using the AGC and the other one without using the AGC.

In the first method, we designed a 3-dB splitter by increasing the separation distance $g_1$ between the two MDM waveguides (as shown in Figure 6.6(a)) until maximum coupling is achieved. We found that the maximum coupling efficiency is about 37% for each branch when $g_1$ = 160 nm, as shown in Figures 6(b and c). This configuration has the advantage in easy fabrication.

The efficiency can be further increased using our AGC. In the second method, we designed a 3-dB splitter by increasing the separation distance $g_2$ between the two MDM waveguides (as shown in Figure 6.7(a)) until maximum coupling is achieved. The increase in $g_2$ was done after the addition of the rectangular AGC. We found that the

maximum coupling efficiency is about 45% for each branch for $g_2$ = 260 nm, as shown in Figures 6.7(b and c). Over 90% of power in total can be delivered into two MDM plasmonic waveguides.

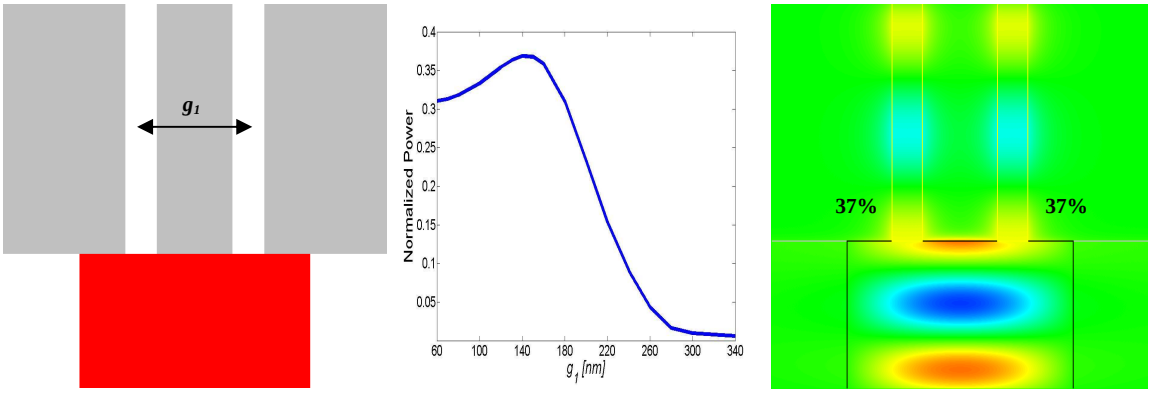


(a) (b) (c)

Figure 6.6: (a) Schematic of the splitter structure without the air-gap coupler. (b) Coupling efficiency as a function of the separation distance $g_1$. (c) Field distribution for the structure shown in Figure 6.6(a) for $g_1$ = 160 nm.

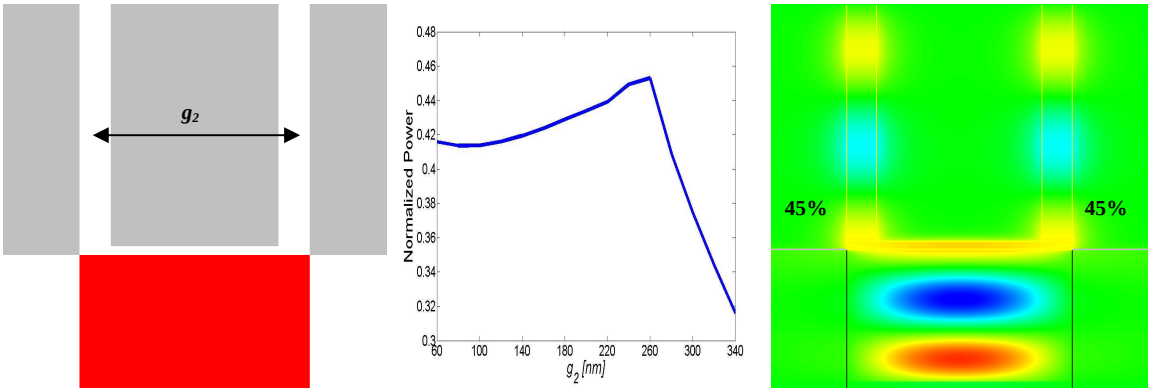


(a) (b) (c)

Figure 6.7: (a) Schematic of the splitter structure with the air-gap coupler. (b) Coupling efficiency as a function of the separation distance $g_2$. (c) Field distribution for the structure shown in Figure 6.7(a) for $g_2$ = 260 nm.

The splitting ratio can be easily controlled by the position of the MDM waveguides $W_R$ and $W_L$, as shown in Figure 6.8(a). Before shifting $W_L$, the displacement between the two waveguides was 260 nm, which resulted in a coupling efficiency of 45%. As expected, we found that as $D_2$ increases, coupling efficiency into the shifted waveguide decreases and coupling efficiency into the fixed waveguide increases (as shown in

Figure 6.8(b)). Figure 6.8(c) shows the coupling efficiency ratio between $W_L$ and $W_R$ for $D_2$ = 150 nm. Even when there is no overlap between the shifted MDM waveguide and silicon waveguide, the coupled power is 10% in $W_L$.

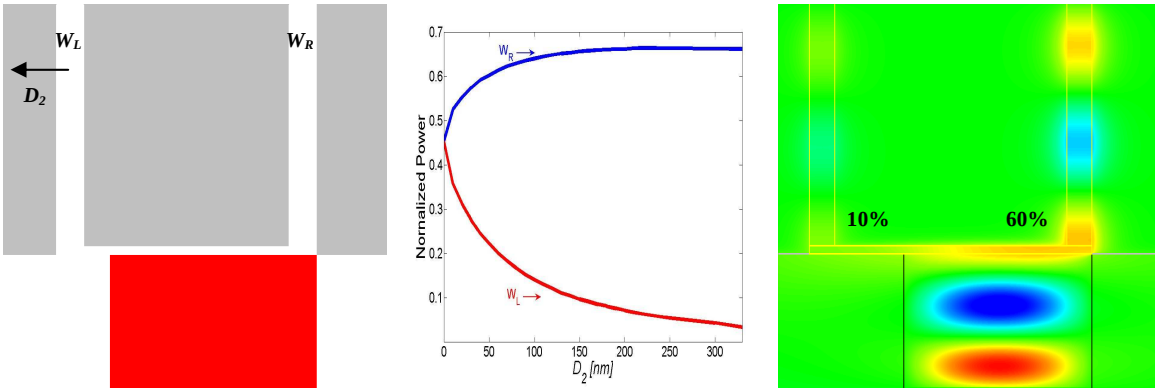


(a) (b) (c)

Figure 6.8: (a) Schematic of the asymmetric splitter structure. (b) Coupling efficiency as a function of the displacement $D_2$. (c) Field distribution for $D_2$ = 150 nm.

Another way to control the splitting ratio is by varying the width of the MDM waveguides $W_1$ and $W_2$, as shown in Figure 6.9(a). We found that as the width of $W_2$ increases from 40 nm to 100 nm, the coupling efficiency in $W_2$ increases slightly from 45% to 47%, while the coupling efficiency in a 40 nm wide $W_1$ decreases from 45% to 28% (as shown in Figure 6.9(b)). The field distribution for $W_2$ = 100 nm and $W_1$ = 40 nm is shown in Figure 6.9(c).

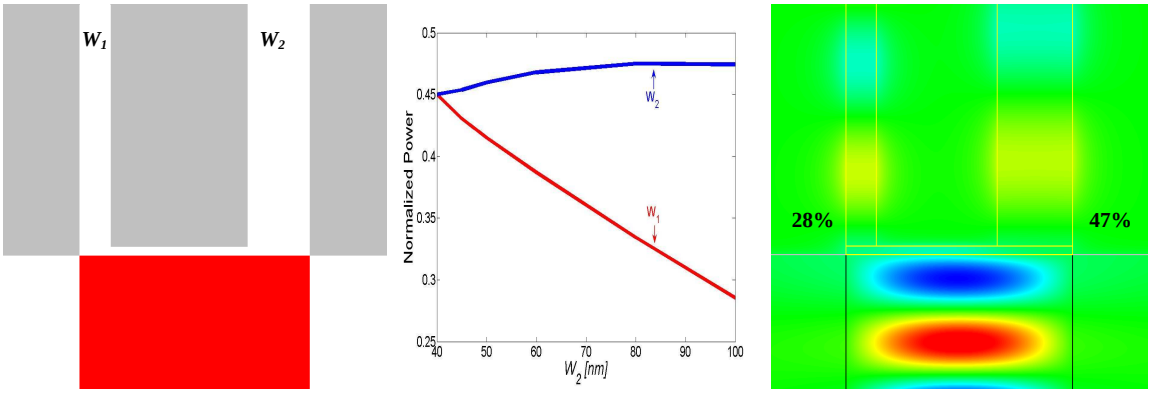


(a) (b) (c)

Figure 6.9: (a) Schematic of the asymmetric splitter structure. (b) Coupling efficiency as a function of $W_2$. (c) Field distribution for $W_2$ = 100 nm and $W_1$ = 40 nm.

The proposed couplers and splitters can also operate at a broad frequency range. To show that, we varied the wavelength of the light source and measured the corresponding coupling efficiency. The coupling efficiency with respect to wavelength for the structures shown in Figures 6.1(c) (with and without AGC), 6.5(c), and 6.6(c) is shown in Figure 6.10. Using the AGC broadens the spectrum range around the communication wavelength 1.55 µm for all structures. Using two plasmonic waveguides in addition to the AGC broadens the spectrum over longer range. The wavelength dependent of the permittivity of metal is not very clear because the coupling efficiency is measured close to the interface with silicon. If the coupling efficiency is measured far away from the interface, then it will be obvious that the losses of the metal increase significantly as the wavelength decreases.

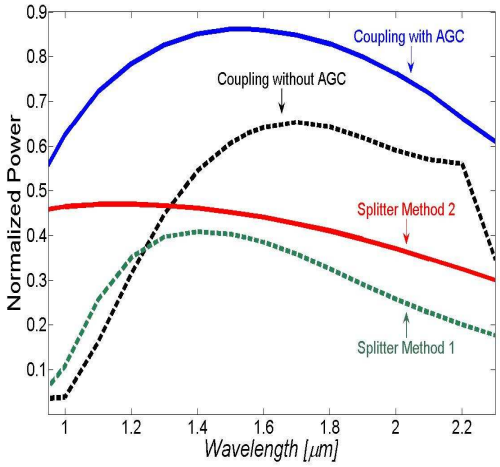


Figure 6.10: Spectrum of the structures shown in Figure 6.1(c) (with and without AGC) and Figures 6.5(c) and 6.6(c).

### 6.2.3 Directional Coupler Design

Figure 6.11(a) shows the schematic of the proposed plasmonic directional coupler. It consists of two MDM waveguides, $W_1$ and $W_2$. $W_1$ was kept connected to the AGC while $W_2$ had a separation distance of 80 nm from the top of the AGC. We studied the effect of

changing the separation distance between the two MDM waveguides, $D_3$, on the coupling efficiency into $W_2$. Figure 6.11(b) shows the coupling efficiency as a function of the overlapped propagation length, $L$, for two cases when $D_3$ = 10 nm and 220 nm. As expected, as $D_3$ increases, the crosstalk between the two MDM waveguides decreases and the coupling length increases. The coupling length, $L_c$, is defined as the propagation length needed to completely transfer light from $W_1$ to $W_2$. The attenuation of the coupled power as $L$ increases is due to the metallic losses. Our simulation results show that $L_c$ increased from 870 nm (Figure 6.11(c)) to about 1700 nm (Figure 6.11(d)) as $D_3$ increased from 10 nm to 20 nm, respectively. Also, our simulation results show that the crosstalk between the two MDM waveguides is negligible when $D_3$ is larger than 150 nm. The coupling length at which the maximum value of the transferred power occurs is slightly off from that of the minimum value of the other waveguide. Zhao *et al.* [22] attributed the position offset to the interaction of the field with the complex refractive index of metal.

An efficient and compact directional coupler can be made when $D_3$ = 10 nm. The power is continuously coupled from one MDM waveguide to another along the propagation direction (Figure 6.11(c)). Total power transfer occurs when the propagation length is equal to about 870 nm. A 3-dB coupler (~40% in each branch) can be made when the propagation length is equal to 453 nm.

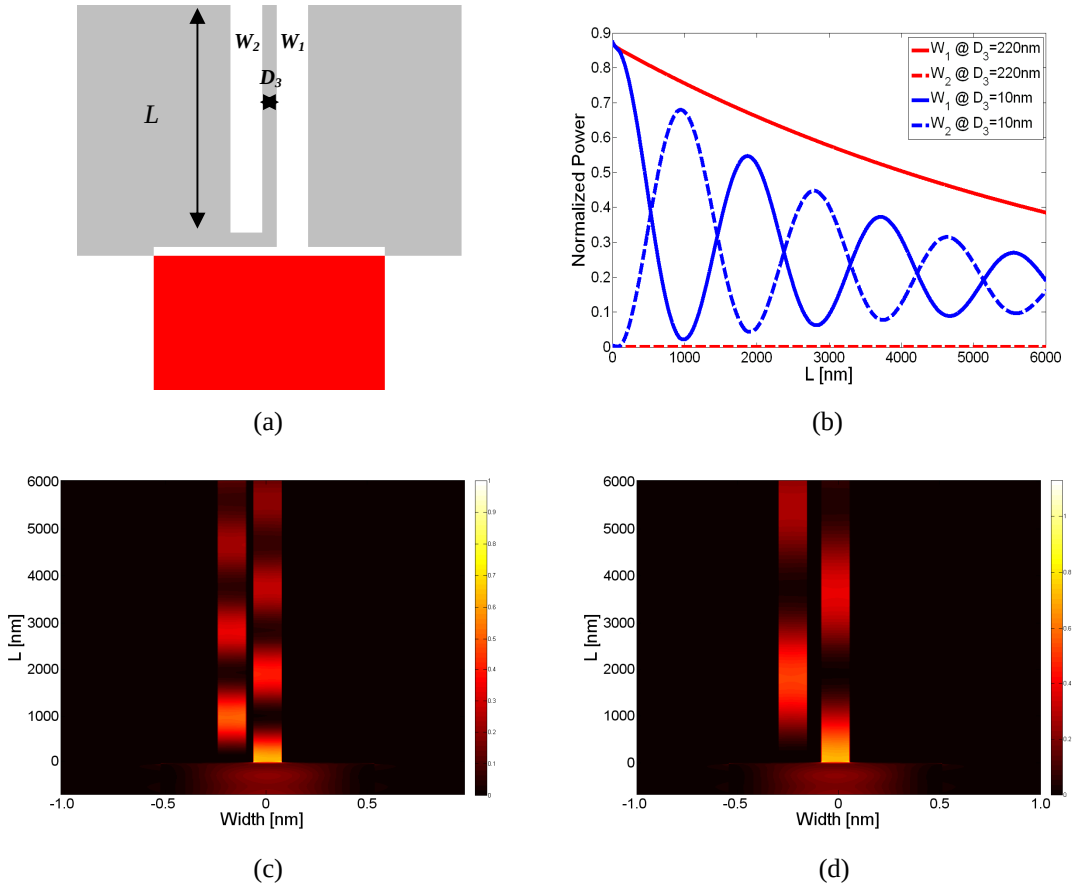


Figure 6.11: (a) Schematic of the directional coupler structure. (b) Coupling efficiency as a function of the overlapped propagation length, $L$, at different values of $D_3$. (c and d) Power density profile for $D_3$ = 10 nm and 20 nm, respectively.

Figure 6.12 shows a 2 × 2 directional coupler switch in which light propagates through port 1 and exits through port 4 when total coupling occurs. The spacing between the two input- (or output-) ports is 320 nm and that between the s-shaped bends is 380 nm. The spacing ensures no crosstalk between the waveguides. The s-shaped bends did not start from the center of the AGC to reduce the size of the switch and the propagation losses. The trade-off is that 4% of the coupling efficiency is lost at each interface, as shown in Figure 6.4(b). The width of the two MDM waveguides is 40 nm, whereas the separation distance between them within the coupling region is 10 nm. Figure 6.12(b) shows the coupling efficiency into ports 3 and 4 as a function of the

coupling length, $L_D$. As $L_D$ increases the power is periodically transferred between the two ports. The interaction length required to achieve total power transfer is equal to 910 nm (see Figure 6.12(c)). The excess loss is -16 dB (coupling efficiency inside port 4 is 37%), while the isolation is -23 dB (crosstalk in port 3). A 3-dB beam splitter can be achieved when $L_D$ is equal to 440 nm.

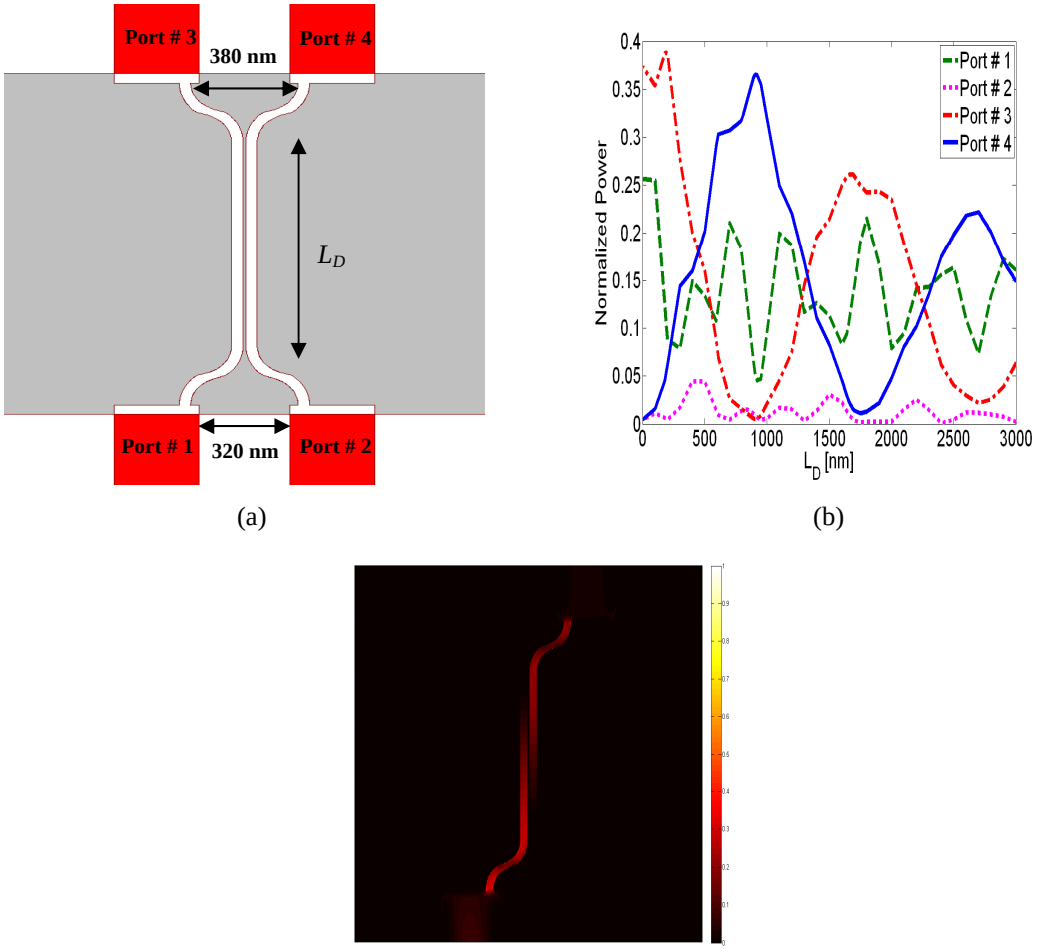


Figure 6.12: (a) Schematic of the switch structure. (b) Coupled power into each port as a function of $L_D$. (c) Power density profile for the proposed switch when $L_D$ = 910 nm.

### 6.2.4 Mach-Zehnder Interferometer Design

Coupling light in and out of the plasmonic waveguide can be achieved by using one of the Fabry-Perot cavity structures that are shown in Figures 6.13(a and b). One structure

(Figure 6.13(a)) consists of a 40 nm-wide MDM waveguide embedded between two silicon waveguides. The other structure (Figure 6.13(b)) consists of a 40 nm-wide MDM waveguide and two AGCs embedded between two silicon waveguides. The coupling efficiency into the output silicon waveguide as a function of the MDM waveguide length, *L*, for both structures is shown in Figure 6.13(c). Efficiency decreases as *L* increases because of the propagation losses due to the metallic absorption. The oscillation in the measured coupling efficiency was dramatically reduced by using the two AGCs. Also, higher coupling efficiency was achieved by using the two AGCs.

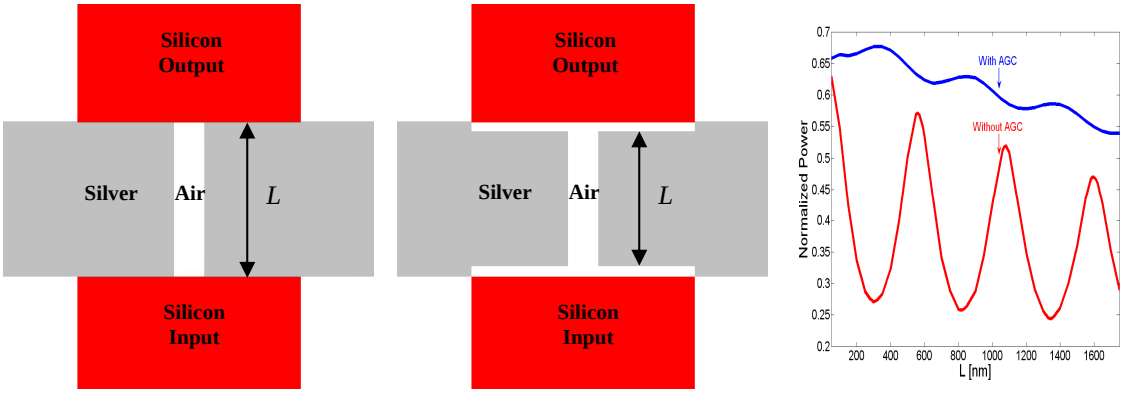


(a) (b) (c)

Figure 6.13: (a and b) Schematic of the Fabry-Perot cavity structures with and without the AGC, respectively. (c) Efficiency as a function of the MDM waveguide length, *L*.

Based on our proposed 3-dB splitter, we propose two designs for a MZI using air-silver-air geometry. The first design is achieved by connecting two splitters back to back, as shown in Figure 6.14(a). In this configuration, the input light is equally split into each MDM waveguide and then recombines at the output silicon waveguide. The two MDM waveguides form the Mach-Zehnder propagation arms. The separation between the MDM waveguides is 220 nm. The output power was measured at the output silicon waveguide as a function of the Mach-Zehnder arm length, *L*, (Figure 6.14(b)). The oscillation in the measured coupling efficiency is due to the Fabry-Perot cavity response

that is caused by the reflection of the plasmon mode from each dielectric waveguide. Efficiency decreases as $L$ increases because of the propagation losses due to the metallic absorption. Figures 6.14(c and d) show the electric field intensity and the power density profile for the proposed structure. It is clear that the input light is equally split into the two MDM waveguides arms and recombines at the output dielectric waveguide. A potential application of this structure is in integrated optical sensors, where the electromagnetic field in the gap between the two MDM waveguides is strongly confined that can be easily disturbed by an external effect.

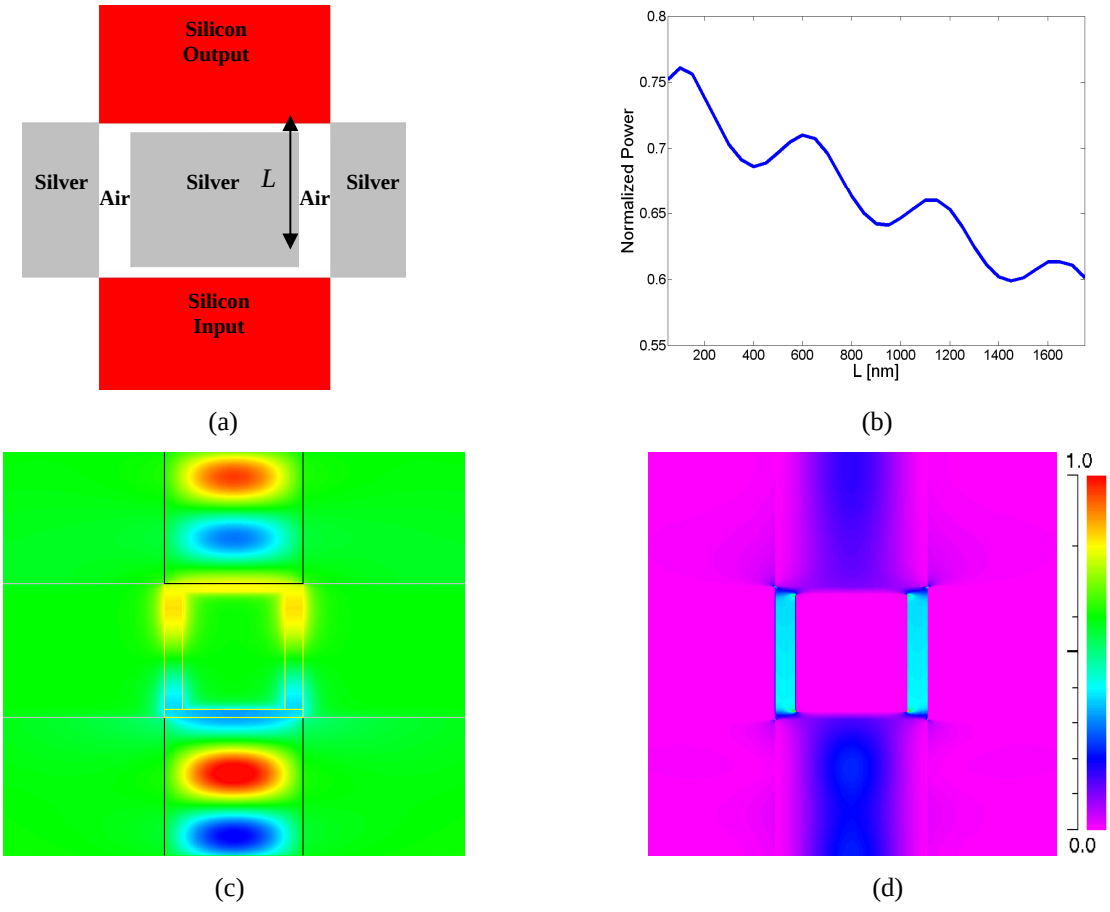


Figure 6.14: (a) Schematic of the proposed silver-air-silver Mach-Zehnder interferometer. (b) Output power as a function of Mach-Zehnder arm length, $L$. (c and d) Field distribution and power density profile for $L$ = 600 nm, respectively.

We propose another MZI structure that consists of a splitter and a directional coupler (a three-waveguide coupler structure), as shown in Figure 6.15(a). The input light is equally split into the two MDM waveguides and recombines at the middle MDM waveguide before it couples into the output dielectric waveguide. The field is highly localized at the end of the middle MZI arm (Figure 6.15(b)). The coupling efficiency is about 53% when the interaction length is equal to 703 nm and the width of the metal between the three MDM waveguides is 10 nm. The length of the MZI structure can slightly be reduced by placing the central MDM waveguide between the two s-shaped plasmonic waveguides.

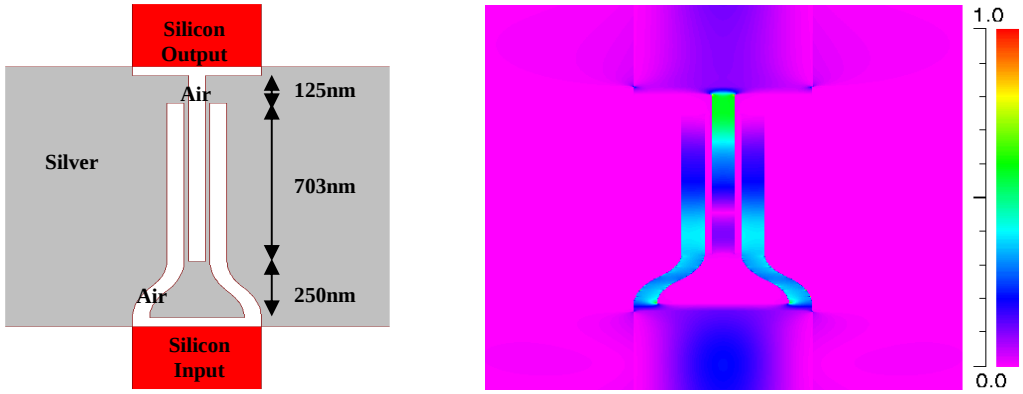


(a) (b)

Figure 6.15: (a) Schematic of the proposed three-waveguide silver-air-silver Mach-Zehnder interferometer. (b) Power field distribution for the proposed structure.

## 6.3 Fabrication

We fabricated the plasmonic air-slot coupler and splitter that are shown in Figures 6.16(a and c). First, the electron-beam is used to define the alignment marks followed by a gold deposition to make the alignment marks detectable using the scanning electron microscope (SEM) of the electron-beam tool at 100 KV. Then, the alignment marks are used to place the dielectric waveguides at a specific location from the marks.

Finally, the alignment marks are reused to define the regions where gold is to be deposited to form the plasmonic slot waveguides. The focused ion beam (FIB) is used to define the slot waveguides. We also deposited a platinum layer on top of the gold layer using the FIB tool before defining the slot waveguides. This is done to get a rectangular shape slot waveguide (i.e., the top of the slot waveguide has the same width as its bottom), or otherwise the slot waveguide will look like a triangular opening (i.e., the top of the slot waveguide is wider than its bottom).

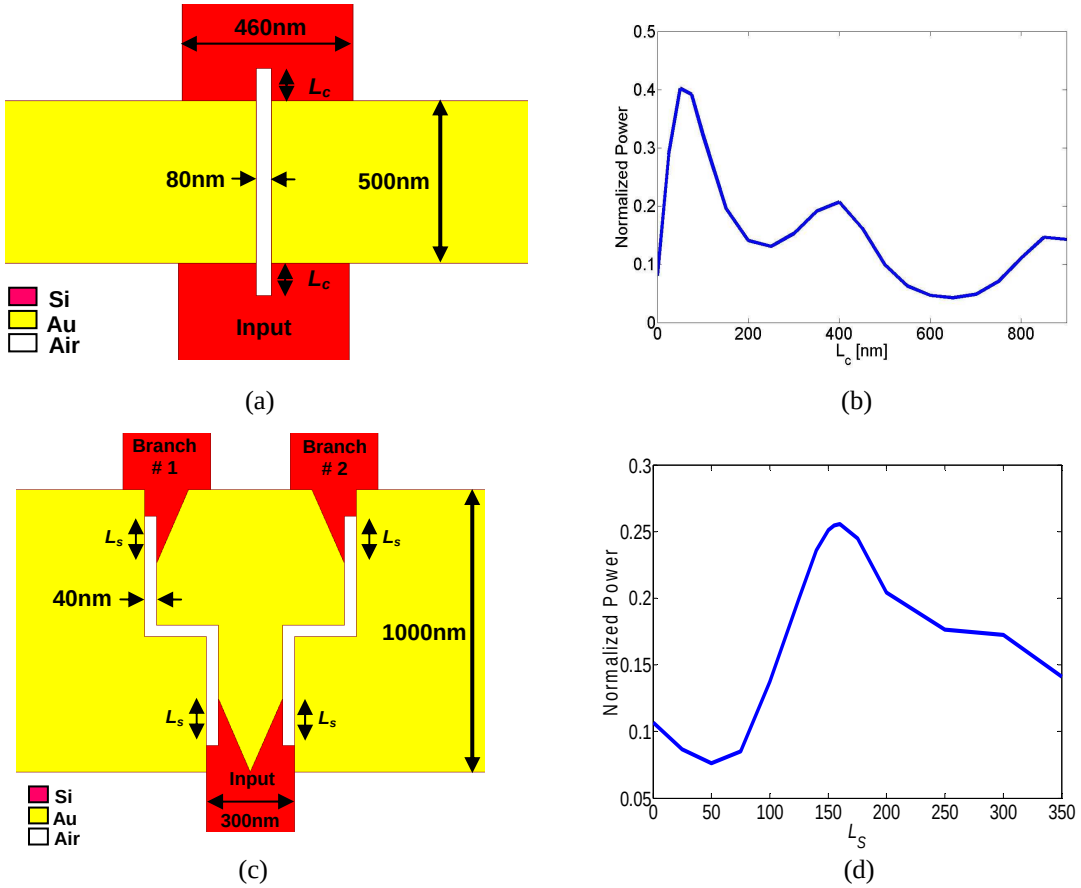


Figure 6.16: (a) Schematic of the plasmonic air-slot coupler. (b) Coupling efficiency as a function of the silicon air-slot waveguide's length, $L_c$. (c) Schematic of the plasmonic splitter device. (b) Coupling efficiency in branch # 1 as a function of the silicon air-slot waveguide's length, $L_s$.

To have a large fabrication tolerance and enhance the coupling efficiency between the silicon waveguide and the plasmonic air-slot waveguide, part of the silicon waveguide at

each end of the plasmonic air-slot waveguide is milled (as shown in Figures 6.16(a and c)). By doing that, light couples from the silicon waveguide into the silicon air-slot waveguide before it couples into the plasmonic air-slot waveguide. The coupling is expected to increase because the field inside the plasmonic air-slot waveguide matches that of the silicon air-slot waveguide [24]. In the simulation, we varied the length of the air-slot waveguide inside the silicon waveguides and measured the corresponding coupling efficiency, as shown in Figures 6.16 (b and d). The length of the air-slot waveguide inside the silicon waveguide is denoted by $L_c$ and $L_s$ for the plasmonic air-slot coupler and splitter, respectively. We found that the coupling efficiency of the coupler increased from 8% to 40% when $L_c$ = 50 nm (see Figure 6.16(b)). The oscillation in the measured coupling efficiency is due to the Fabry-Perot cavity response that is caused by the reflection of the mode from each dielectric waveguide. The coupling efficiency also increased in each branch of the splitter from 11% to 26% when $L_s$ = 160 nm (see Figure 6.16(c)). SEM images of the fabricated devices are shown in Figure 6.17.

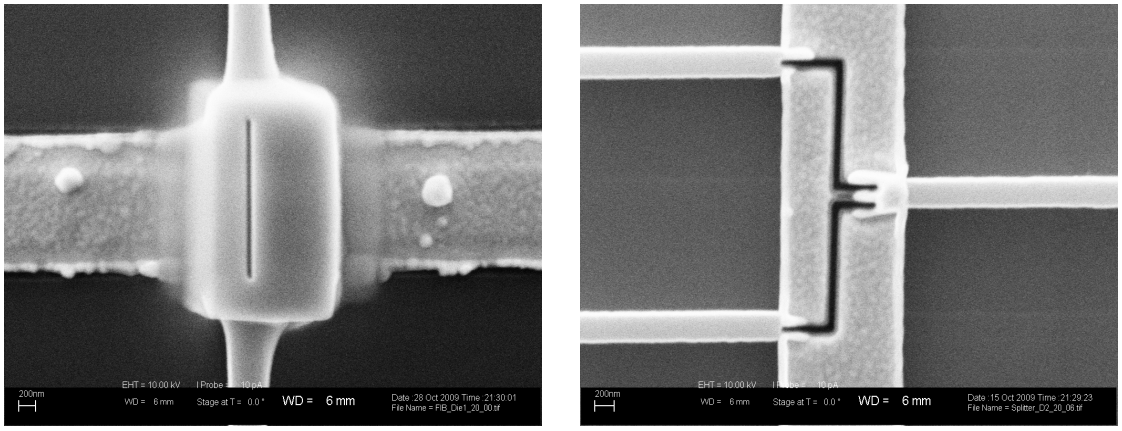


(a) (b)

Figure 6.17: Scanning electron microscope image of the fabricated (a) plasmonic air-slot coupler and (b) plasmonic splitter.

## 6.4 Experimental Results

The plasmonic air-slot coupler and splitter introduced in the previous sections were fabricated and tested. The experimental measurement set up was as follows: the light from a tunable laser with spectral range from 1260 nm to 1620 nm propagated through a polarization controller to allow TM-like modes to couple into the silicon waveguide. Coupling into and out of the silicon waveguides was achieved using tapered micro-lens fibers with a spot diameter of 2.5±0.5 micron. Translational stages were used to align the input and output fibers to the device being tested. The output power was measured using an infrared detector and recorded using a power meter. The experimental results of the plasmonic air-slot coupler and splitter are reported in the following sections.

### 6.4.1 Plasmonic Air-Slot Coupler Results

The output light power was measured as the wavelength of a tunable laser source was scanned from 1260 to 1620 nm. The coupler output measurements were taken every 5 nm along the specified range. The normalized output power of the plasmonic air-slot coupler was plotted as a function of wavelength (see Figure 6.18). It is not possible to determine the peak of the spectrum of the device because of the limitation of the tunable laser source since it does not operate beyond 1620 nm. The measured spectrum of the fabricated plasmonic coupler has a trend similar to that of the simulation except that it is shifted by 110 nm (see Figure 6.18). This was expected because of the sensitivity of the devices to fabrication errors such as a change in the e-beam current or the time used to develop the phororesist. These errors resulted in fabricating waveguides of widths different than the targeted values for the width of the silicon and plasmonic waveguides,

which were 460 nm and 80 nm, respectively. The measured value for the former one is 500 nm and that for the latter one is 75 nm (see Figure 6.19).

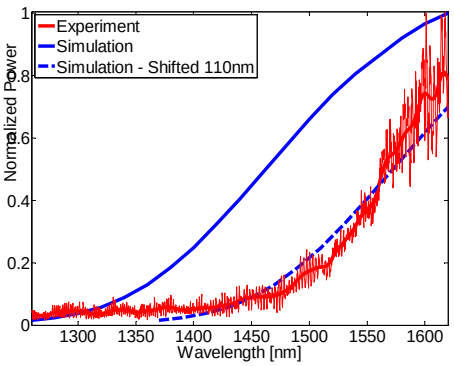


Figure 6.18: Comparison of the experimental and simulation results of the plasmonic air-slot coupler.

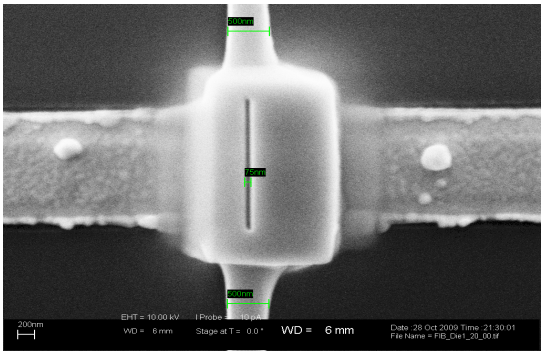


Figure 6.19: SEM image of the fabricated plasmonic coupler that shows the width of the silicon and plasmonic waveguides.

In order to show the sensitivity of our plasmonic slot coupler to fabrication errors, we investigated through numerical simulations the effect of changing various parameters on the spectrum response of our device. The parameters that we changed were: the length of the air-slot waveguide inside the silicon waveguide $L_c$, the width of the silicon waveguide $W_{Si}$, the width of the plasmonic slot waveguide $W_{Slot}$, the misalignment between the plasmonic slot waveguide and the silicon waveguide $S$, and the propagation length $L_p$. The optimum values that we used for $L_c$, $W_{Si}$, $W_{Slot}$, $S$, and $L_p$ were 50 nm, 460 nm, 80 nm, 0 nm, and 500 nm, respectively. We studied the effect of changing one parameter on the spectrum response while keeping the remaining parameters at their optimum

values. We found that changing $L_c$ from 0 nm to 400 nm resulted in a change in the spectrum response shape mainly due to the Fabry-Perot cavity-like effect in addition to the impedance mismatch between the silicon and slot waveguides which is a function of wavelength (see Figure 6.16(b)). We also found that the cut-off wavelength can be controlled by changing the dimension of $W_{Si}$ (see Figure 6.20(c)) or $W_{Slot}$ (see Figure 6.20(d)). Changing $W_{Si}$ from 420 nm to 500 nm, resulted in shifting the cut-off wavelength from about 1150 nm to 1400 nm (i.e., right shift). Whereas, changing $W_{Slot}$ from 40 nm to 120 nm, resulted in shifting the cut-off wavelength from about 1400 nm to 1250 nm (i.e., left shift). This shift occurs because, as the waveguide's width changes, the mode size changes and consequently the impedance mismatch between the silicon and slot waveguide changes. In Figure 6.18, the experimental curve was shifted by 110 nm because either the width of the silicon waveguide was increased by about 40 nm (i.e., $W_{Si}$ = 500 nm) or the width of the slot waveguide was decreased by 40 nm (i.e., $W_{Slot}$ = 40 nm) or a combination of both. We measured $W_{Si}$ and $W_{Slot}$ using SEM, and found them equal to 500 nm and 75 nm, respectively (see Figure 6.19). In addition, we observed that changing $S$ from 0 nm to 80 nm resulted in a reduction in the coupled power into the plasmonic slot waveguide due to the reduction in the overlapped area between the mode supported by the slot waveguide and the silicon waveguide (see Figure 6.20(e)). For example, at a wavelength of 1800 nm, the coupled power dropped by a factor of 10 (i.e., 70% to 7%), when the slot waveguide is shifted by 80 nm. Finally, we found that changing $L_p$ from 500 nm to 2000 nm resulted in a reduction in the transmitted power into the output silicon waveguide mainly due to the propagation loss of the metal (see Figure 6.20(f)). For instance, the coupled power dropped by about 0.8 dB (i.e., 69%

to 57%), at a wavelength of 1800 nm by increasing $L_p$ from 500 nm to 2000 nm. From these simulation results, it is obvious that the spectrum response of the plasmonic coupler is strongly dependent on $L_c$ and $S$, and less dependent on $W_{Si}$, $W_{Slot}$, and $L_p$.

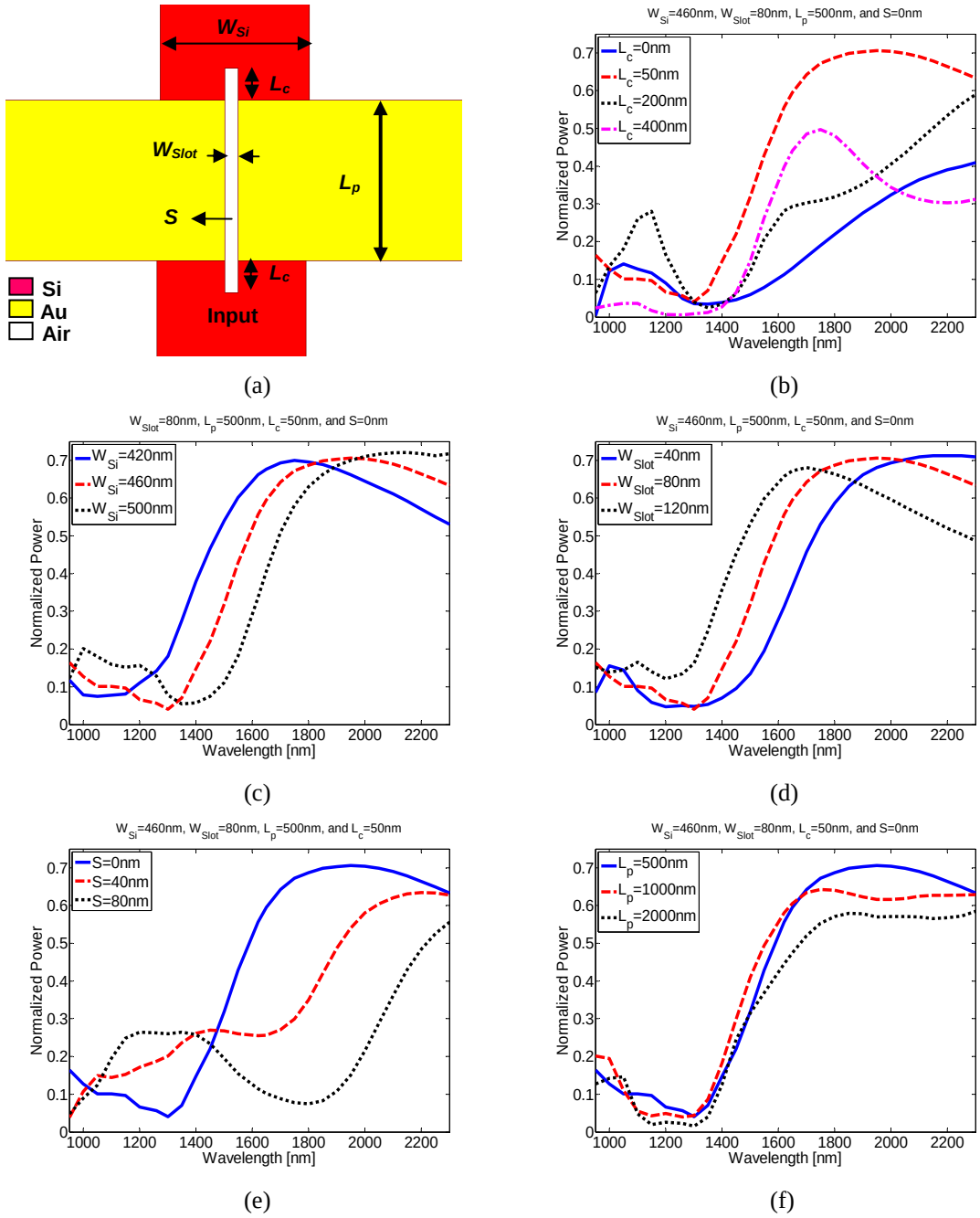


Figure 6.20: (a) Schematic of the plasmonic slot coupler. (b-f) Dependence of the spectrum response of the plasmonic slot coupler on the length of the air-slot waveguide inside silicon $L_c$, the width of the silicon waveguide $W_{Si}$, the width of the plasmonic slot waveguide $W_{Slot}$, the misalignment between the plasmonic slot waveguide and the silicon waveguide $S$, and the propagation length $L_p$, respectively.

We fabricated two plasmonic couplers of different lengths to investigate the effect of changing the propagation length on the spectrum response of the coupler. One coupler had a length of 500 nm and the other had a length of 2000 nm. The experimental results in Figure 6.21 show that changing $L_p$ from 500 nm to 2000 nm resulted in a reduction in the transmitted power into the output silicon waveguide by about 3 dB (measured within the spectral range understudy). This measurement cannot be used to calculate the propagation loss of the plasmonic waveguide because the two couplers are not identical due to fabrication errors. The propagation loss can be lowered by reducing the time that the waveguides face the gallium ions when using the FIB tool and by fabricating the air-slot waveguide at the optimum length and width that resulted in high coupling efficiency (see Figure 6.16(b)).

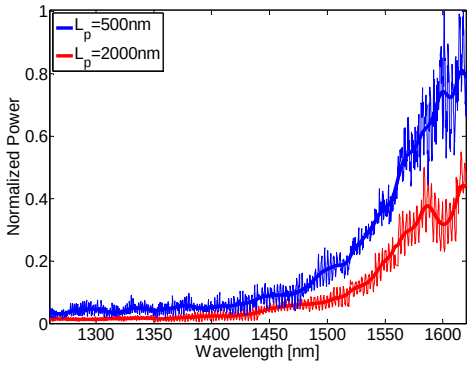


Figure 6.21: Experimental results of two plasmonic air-slot couplers: one had a length of 500 nm and the other had a length of 2000 nm.

### 6.4.2 Plasmonic Splitter Results

A comparison between the experimental and simulation results of the plasmonic splitter is shown in Figure 6.22. The measured spectrum of the fabricated plasmonic splitter is narrower than that in the simulation. This met expectations because of the sensitivity of the devices to fabrication errors. As shown in Figure 6.16 (c), the designed plasmonic slot

waveguide is terminated by tapered silicon waveguides, whereas the fabricated plasmonic slot waveguide is not. This is mainly due to using the FIB. Figure 6.23 shows the SEM image of the plasmonic splitter before and after using the FIB. The absence of the tapered silicon waveguide and the misalignment between the plasmonic slot waveguide and the silicon waveguide (see Figure 6.24 (e)) resulted in a narrowing of the measured spectrum due to the reduction of the overlapped area between the mode size supported by the slot waveguide and the silicon waveguide.

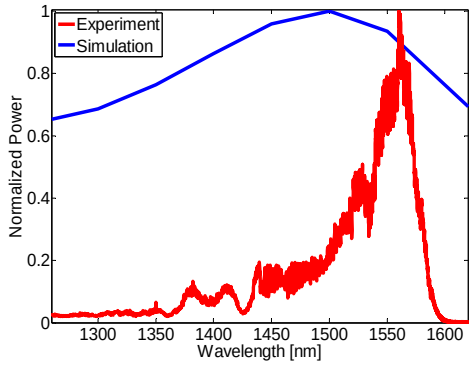


Figure 6.22: Comparison of the experimental and simulation results of the plasmonic splitter.

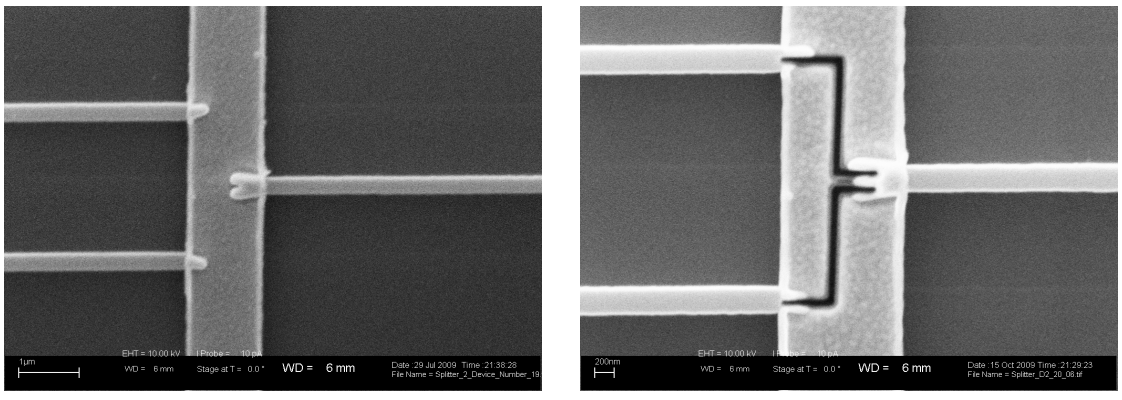


(a) (b)

Figure 6.23: SEM image of the plasmonic splitter (a) before using the FIB and (b) after using the FIB.

Numerically, we investigated the effect of changing various parameters on the spectrum response of the plasmonic splitter. The parameters that we changed were: the length of the air-slot waveguide inside the silicon waveguide $L_s$, the width of the silicon

waveguide $W_{Si}$, the width of the plasmonic slot waveguide $W_{Slot}$, the misalignment between the plasmonic slot waveguide and the silicon waveguide $S$, and the propagation length $L_p$. The optimum values that we used for $L_s$, $W_{Si}$, $W_{Slot}$, $S$, and $L_p$ were 50 nm, 300 nm, 40 nm, 0 nm, and 500 nm, respectively. We studied the effect of changing one parameter on the spectrum response while keeping the remaining parameters at their optimum values. Changing $L_s$ from 120 nm to 200 nm (see Figure 6.24(b)) resulted in a change in the spectrum response shape mainly due to the Fabry-Perot cavity-like effect (see Figure 6.16(d)) in addition to the impedance mismatch between the silicon and slot waveguides which is a function of wavelength. Additionally, the spectrum could be broadened by changing the dimension of $W_{Si}$, (see Figure 6.24(c)) and $W_{Slot}$ (see Figure 6.24(d)). Changing $W_{Si}$ from 300 nm to 400 nm, resulted in a narrowing of the spectrum's width by approximately 600 nm. Whereas, changing $W_{Slot}$ from 40 nm to 120 nm, resulted in a narrowing of the spectrum width by approximately 300 nm. This is because, as the waveguide's width changes, the mode size changes and consequently the impedance mismatch between the silicon and slot waveguide changes. Further, we observed that changing $S$ from 0 nm to 80 nm resulted in a narrowing of the spectrum response of the splitter by approximately 600 nm due to the reduction in the overlapped area between the mode size supported by the slot waveguide and the silicon waveguide (see Figure 6.24(e)). Finally, we found that changing $L_p$ from 500 nm to 2000 nm resulted in a reduction in the transmitted power into the output silicon waveguide mainly due to the propagation loss of the metal and the Fabry-Perot effect (see Figure 6.24(f)). From these simulation results, it is obvious that the spectrum response of the plasmonic splitter is strongly dependent on $W_{Si}$, $W_{Slot}$, and $S$ and less dependent on $L_s$ *and* $L_p$.

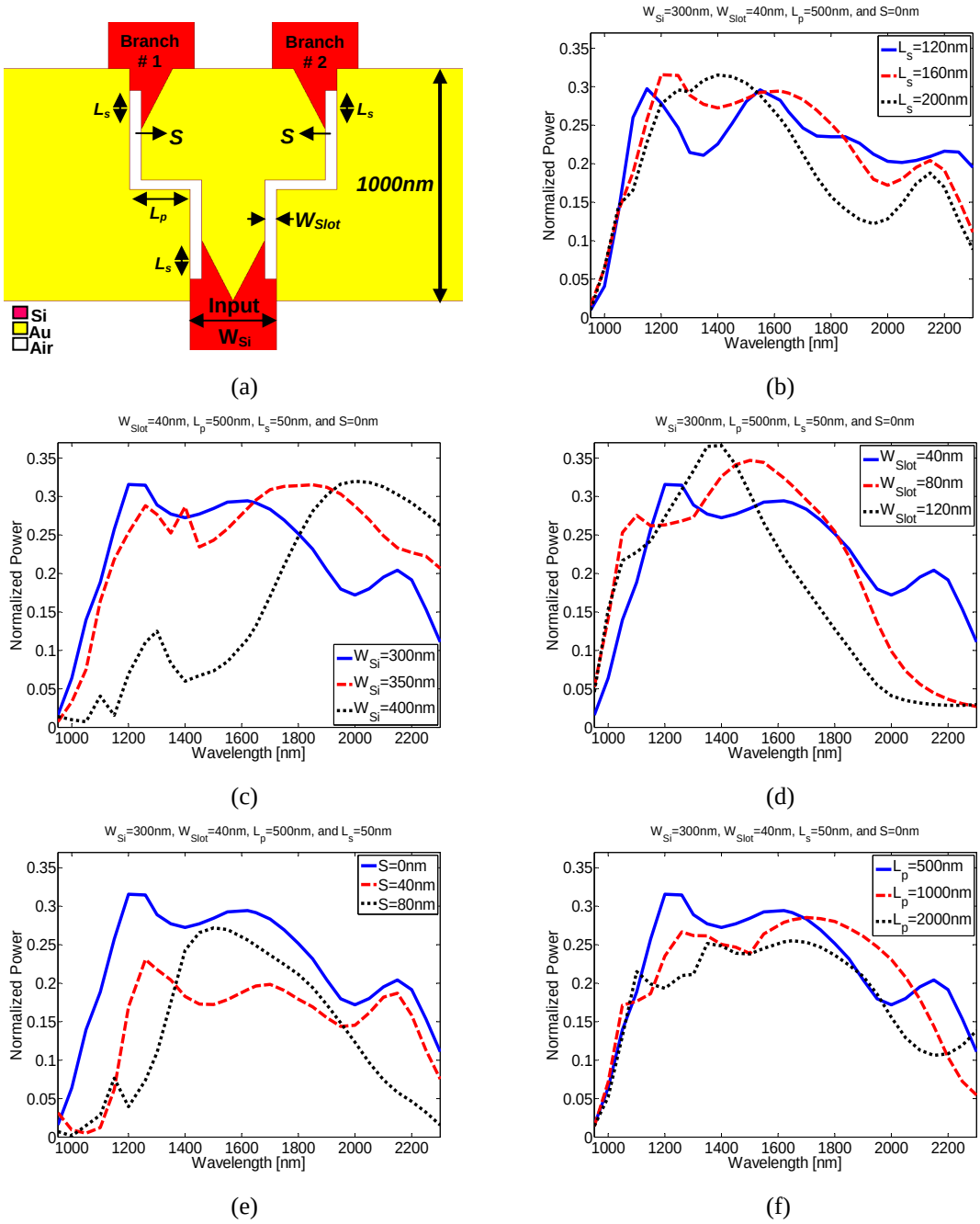


Figure 6.24: (a) Schematic of the plasmonic splitter. (b-f) Dependence of the spectrum response of the plasmonic splitter on the length of the air-slot waveguide inside silicon $L_s$, width of the silicon waveguide $W_{Si}$, width of the plasmonic slot waveguide $W_{Slot}$, misalignment between the plasmonic slot waveguide and the silicon waveguide $S$, and propagation length $L_p$, respectively.

We compared the measured spectrum of a Y-shaped silicon splitter of a radius of 10 μm (see Figure 6.25(a)) with that of a straight silicon waveguide. We found that the coupling efficiency of each branch of the Y-shaped silicon splitter is approximately 40%

of that achieved by the straight silicon waveguide (see Figure 6.25(b)). We also compared the measured spectrum of the Y-shaped silicon splitter with that of our fabricated plasmonic splitter. We found that the coupling efficiency of our device is between 7% and 35% of that achieved by the Y-shaped silicon splitter over a wavelength of 1540 nm to 1570 nm (see Figure 6.25(c)). To investigate the effect of the propagation length on the spectrum response of the plasmonic splitter, we fabricated two splitter devices of different lengths. One plasmonic splitter had a length of 1250 nm and the other had a length of 2250 nm. The experimental results (see Figure 6.25(d)) show that changing the propagation length from 1250 nm to 2250 nm resulted in a reduction in the transmitted power into the output silicon waveguide by about 6 dB. However, this propagation loss is not directly related to the longer propagation length because the two plasmonic splitters are not identical. It is almost impossible to fabricate two plasmonic splitters that are identical due to fabrication errors. It is even impossible to get the same coupling efficiency from each branch of a plasmonic splitter due to the asymmetry between the two plasmonic waveguides (see Figure 6.25(e)). The propagation loss can be minimized by reducing the time that the waveguides face the gallium ions when using the FIB tool and by fabricating the length of the silicon air-slot waveguide at the optimum length that results in high coupling efficiency. Also, preventing the gold from covering the silicon waveguides near the splitter area will increase the coupling efficiency. As shown in Figure 6.17(b), the gold film covered part of the input silicon waveguide which reduced the coupled power into each branch of the splitter. The experimental results show that the waveguides caused a wavelength cut-off around 1600 nm (see Figure 6.25(f)). This happened because the fabricated silicon waveguides are slightly lower than 300 nm

which caused a cut-off at about 1600 nm. The targeted width of the silicon waveguides was 300 nm which supports the minimum TM mode size.

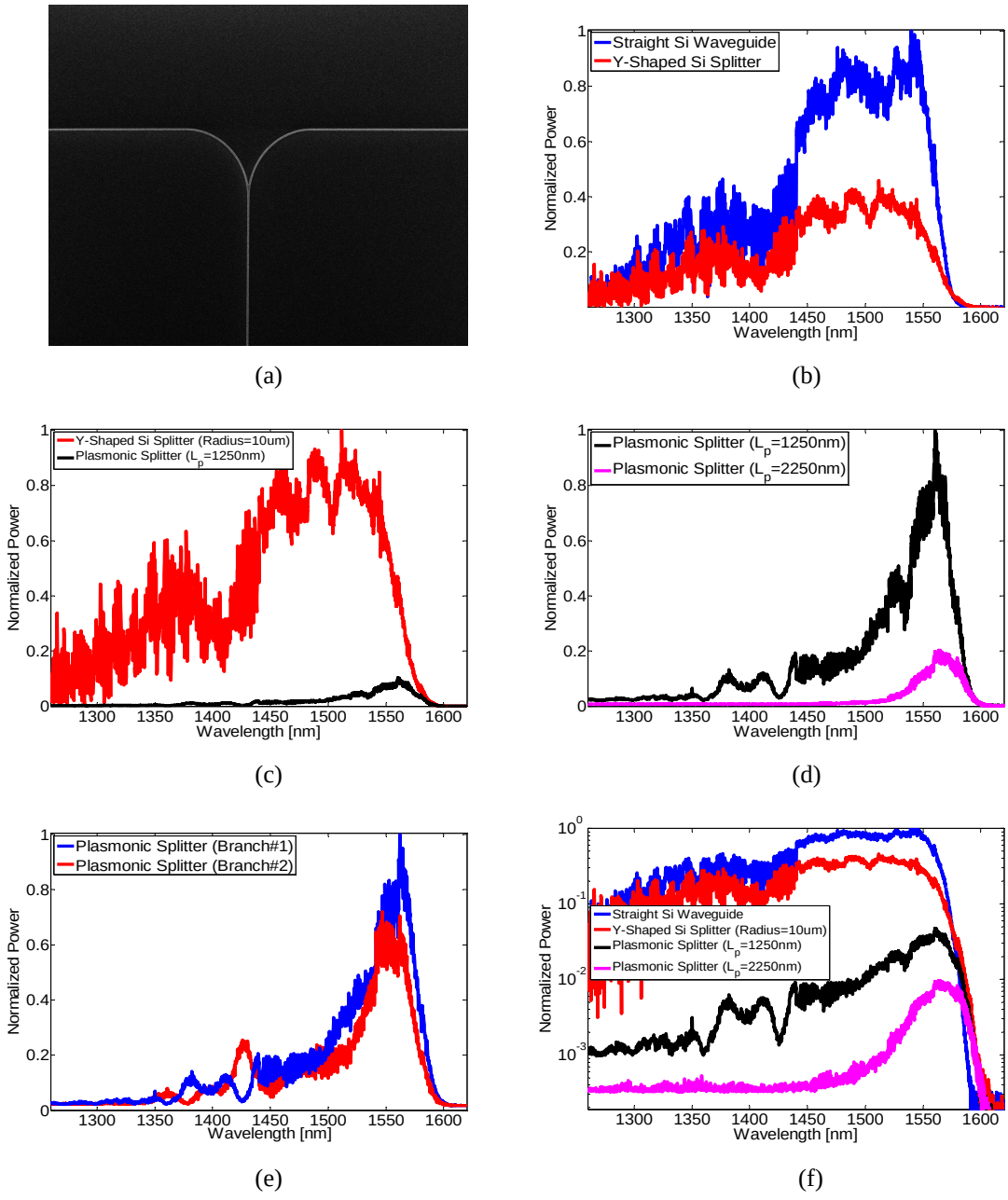


Figure 6.25: (a) SEM image of a Y-shaped silicon waveguide with a radius of 10 μm. Experimental results of (b) a straight silicon waveguide and a Y-shaped silicon splitter, (c) a Y-shaped silicon splitter and a plasmonic splitter, (d) two plasmonic splitters of different lengths, (e) each branch of a plasmonic splitter, and (f) a straight silicon waveguide, a Y-shaped silicon splitter, and two plasmonic splitters of different lengths.

## 6.5 Summary

In this chapter, we proposed a direct yet efficient short plasmonic coupler of a length of 33 nm to increase the coupling efficiency between a silicon waveguide and a silver-air-silver plasmonic waveguide. Based on the coupler, we proposed a splitter that delivers light from a silicon waveguide into two plasmonic waveguides achieving a coupling efficiency of 45% for each branch. We also presented two potential applications of the proposed coupler and splitter in two nano-scale plasmonic devices: a directional coupler and a Mach-Zehnder interferometer. The overall efficiency was 37% for a 2 × 2 directional coupler switch and above 50% for the proposed designs of a Mach Zehnder Interferometer. To confirm the analytical results, we fabricated and tested the coupler and splitter.

## References


[1] R. A. Wahsheh, Z. Lu, and M. A. G. Abushagur, "Efficient couplers and splitters from dielectric waveguides to plasmonic waveguides", in Frontiers in Optics, OSA Technical Digest (CD) (Optical Society of America), October 2008, pp. FThS4. http://www.opticsinfobase.org/abstract.cfm?URI=FiO-2008-FThS4

[2] R. A. Wahsheh, Z. Lu, and M. A. G. Abushagur, "Ultra-compact nanoplasmonic splitter," International Symposium on High Capacity Optical Networks and Enabling Technologies, HONET, December 2009, pp. 179-181.

[3] R. A. Wahsheh, Z. Lu, and M. A. G. Abushagur, "Nanoplasmonic couplers and splitters," Optics Express, vol. 17, October 2009, pp. 19033-19040.

[4] R. A. Wahsheh, Z. Lu, and M. A. G. Abushagur, “Compact Nanoplasmonic Mach-Zehnder Interferometers,” International Symposium on High Capacity Optical Networks and Enabling Technologies, HONET, December 2009, pp. 182-183.

[5] R. A. Wahsheh, Z. Lu, and M. A. G. Abushagur, “Nanoplasmonic Directional Couplers and Mach-Zehnder Interferometers,” Optics Communications, vol. 282, September 2009, pp. 4622-4626.

[6] E. N. Economou, “Surface plasmons in thin films,” Physical Review, vol. 182, June 1969, pp. 539-554.

[7] D. F. P. Pile, T. Ogawa, D. K. Gramotnev, Y. Matsuzaki, K. C. Vernon, K. Yamaguchi, T. Okamoto, M. Haraguchi, and M. Fukui, “Two-dimensionally localized modes of a nanoscale gap plasmon waveguide,” Applied Physics Letters, vol. 87, December 2005, pp. 261114.1-261114.3.

[8] R. Coccioli, M. Boroditsky, K. W. Kim, Y. Rahmat-Samii, and E. Yablonovitch, “Smallest possible electromagnetic mode volume in a dielectric cavity,” IEE Proceedings: Optoelectronics, vol. 145, December 1998, pp. 391-397

[9] G. Veronis and S. Fan, “Theoretical investigation of compact couplers between dielectric slab waveguides and two-dimensional metal-dielectric-metal plasmonic waveguides,” Optics Express, vol. 15, February 2007, pp. 1211-1221.

[10] P. Ginzburg and M. Orenstein, “Plasmonic transmission lines: From micro to nano scale with λ/4 impedance matching,” Optics Express, vol. 15, May 2007, pp. 6762-6767.

[11] D. F. P. Pile and D. K. Gramotnev, “Adiabatic and nonadiabatic nanofocusing of plasmons by tapered gap plasmon waveguides,” Applied Physics Letters, vol. 89, July 2006, pp. 041111.1-041111.3.

[12] P. Ginzburg, D. Arbel, and M. Orenstein, “Gap plasmon polariton structure for very efficient microscale-to-nanoscale interfacing,” Optics Express, vol. 31, November 2006, pp. 3288-3290.

[13] R. Charbonneau, N. Lahoud, G. Mattiussi, and P. Berini, “Demonstration of integrated optics elements based on long-ranging surface plasmon polaritons,” Optics Express, vol. 13, February 2005, pp. 977-984.

[14] R. Charbonneau, C. Scales, I. Breukelaar, S. Fafard, N. Lahoud, G. Mattiussi, and P. Berini, “Passive integrated optics elements based on long-range surface plasmon polaritons,” Journal of Lightwave Technology, vol. 24, January 2006, pp. 477-494.

[15] C. Manolatou, S. G. Johnson, S. Fan, P. R. Villeneuve, H. A. Haus, and J. D. Joannopoulos, “High-density integrated optics,” Journal of Lightwave Technology, vol. 17, September 1999, pp.1682-1692.

[16] J. S. Jensen and O. Sigmund, “Topology optimization of photonic crystal structures: A high-bandwidth low-loss T-junction waveguide,” Journal of the Optical Society of America B, vol. 22, June 2005, pp. 1191-1198.

[17] G. Veronis and S. Fan, “Bends and splitters in metal-dielectric-metal subwavelength plasmonic waveguides,” Applied Physics Letters, vol. 87, September 2005, pp. 131102.1-131102.3.

[18] B. Wang and G. P. Wang, “Surface Plasmon polariton propagation in nanoscale metal gap waveguides,” Optics Express, vol. 29, September 2004, pp. 1992-1994.

[19] Z. Han, L. Liu, and E. Forsberg, “Ultra-compact directional couplers and Mach-Zehnder interferometers employing surface Plasmon polaritons,” Optics Communications, vol. 259, March 2006, pp. 690-695.

[20] Z. Kang and G. P. Wang, “Coupled metal gap waveguides as plasmonic wavelength sorters,” Optics Express, vol. 16, May 2008, pp. 7680-7685.

[21] H. Zhao, X. G. Guang, and J. Huang, “Novel optical directional coupler based on surface plasmon polaritons,” Physica E, vol. 40, September 2008, pp. 3025-3029.

[22] R. Zia, M. D. Selker, P. B. Catrysse, and M. L. Brongersma, “Geometries and materials for subwavelength surface Plasmon modes,” Journal of the Optical Society of America A, vol. 21, December 2004, pp. 2442-2445.

[23] L. Chen, J. Shakya, and M. Lipson, “Subwavelength confinement in an integrated metal slot waveguide on silicon,” Optics Letters, vol. 31, July 2006, pp. 2133-2135.

[24] V. R. Almeida, Q. Xu, C. A. Barrios, and M. Lipson, "Guiding and confining light in void nanostructure," Optics Letters, vol. 29, June 2004, pp. 1209-1211.

# Chapter 7

# Fabrication Process and Challenges

In this chapter, we introduce the fabrication process that we have used in fabricating all the devices in this dissertation. We address the process steps and the challenges we faced and the ways we were able to overcome them. In this research we used silicon-on-insulator substrates for the fabrication of the devices. Other materials could have been used.

## 7.1 Fabrication Process

Silicon-on-insulator (SOI) substrates are used in the fabrication of the optical waveguides because they provide a high index contrast with low transmission losses that is required for guiding light. Also, SOI technology is widely used in microelectronics fabrication which makes it possible for future integration of optoelectronic components on the same chip. The main source of losses in the SOI waveguides is from the sidewall roughness. Lee *et al.* [1] reduced the sidewall roughness of a $Si/SiO_2$ strip waveguide by oxidation

smoothing and anisotropic etching methods and measured a transmission loss of 0.8 dB/cm. The fabrication process of SOI technology (as shown in Figure 7.1) mainly involves: SOI cleaning, photoresist coating, electron-beam lithography, chemical or plasma etch, and film deposition. The surface of the SOI wafers should be maintained cleaned during the fabrication process to prevent defects from occurring in the integrated optical circuit. Cleaning is done by immersing the wafers in hot chemical paths to remove heavy metal, organic and ionic contaminations in addition to removing oxide from the top of the SOI. After cleaning, a photoresist that is sensitive to electron-beam is spun coated on the top of the wafer. The two types of photoresist that we used in our work are a negative resist (XR-1541) and a positive resist (Zep 520A). The unexposed areas in the former one is removed by using AZ® 300 metal-ion-free (MIF) and the exposed areas in the latter one is removed by using ZED-N50. In this work, the negative resist is used to transfer the pattern to the silicon layer while the positive resist is used to define the waveguide regions where metal deposition is needed.

High resolution lithography is required in optical integrated circuits. The resolution of the G-line (1000 nm), I-line (500 nm), and deep ultra violet (300 nm) is insufficient to fabricate the PC structures. High resolution lithography is possible using electron-beam lithography that can directly transfer the pattern to the photoresist without using a mask. When the accelerated electron-beam electrons interact with the negative resist, the resist transforms to hydrogen silsesquioxane (HSQ) that does not dissolve in the MIF developer. HSQ acts as silicon oxide except that it has many hydrogen bonds. Heating up the resist for several minutes reduces the number of hydrogen bonds and consequently hardens HSQ [2]. Secondary electrons may be generated due to the interaction of the electron-beam

electrons with the substrate. These secondary electrons increase the dose of the features that are affected by them. This is called the proximity effect. It has the effect of changing the feature size in addition to reducing the resolution of the fabricated devices [3]. One way to decrease the proximity effect is by adjusting the size and separation distance between the written features. Another way is by performing a dose test to find out the exact dose that is needed to write the features. Figure 7.2 shows how a high dose causes surface roughness and a bad sidewall angle.

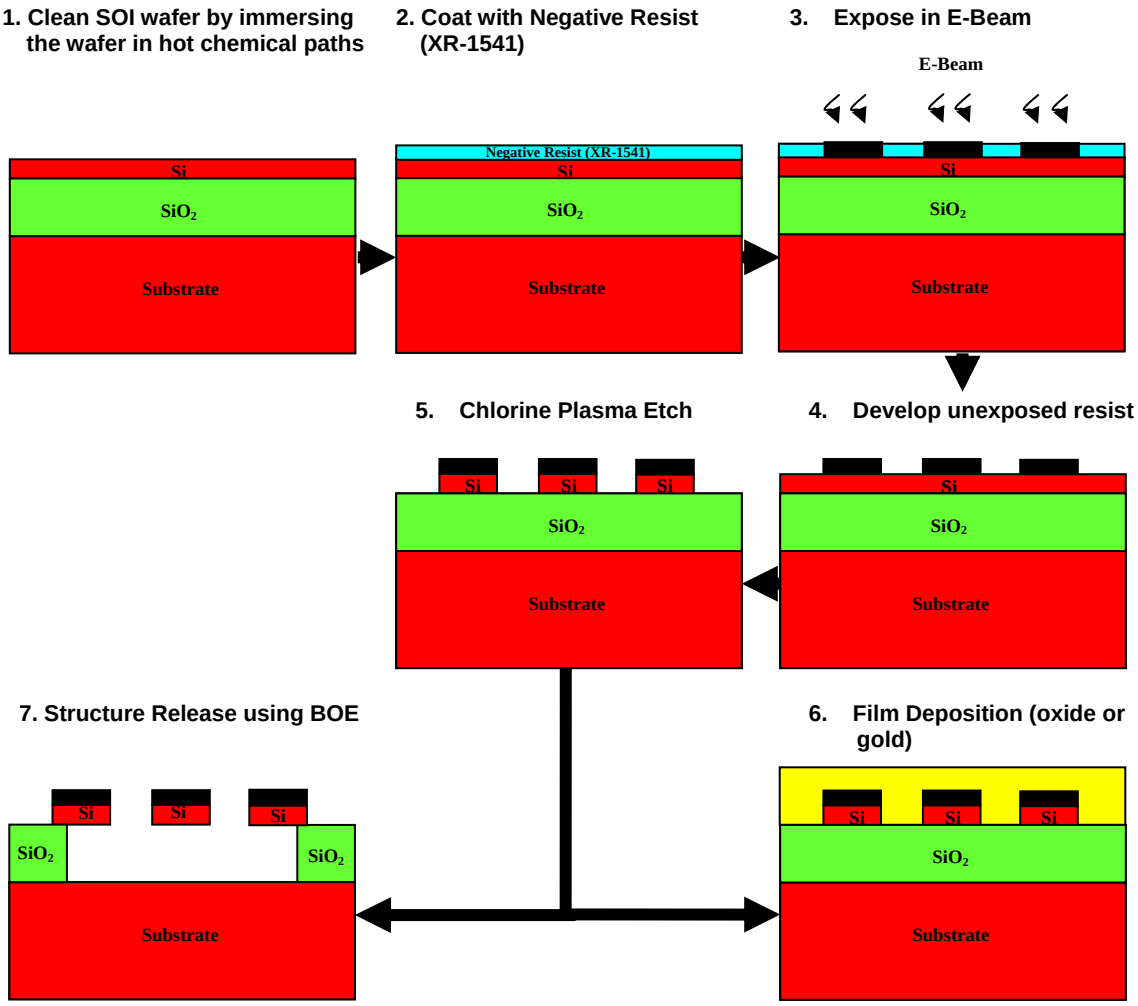


Figure 7.1: Fabrication process of the dielectric, photonic crystal, and plasmonic waveguides.

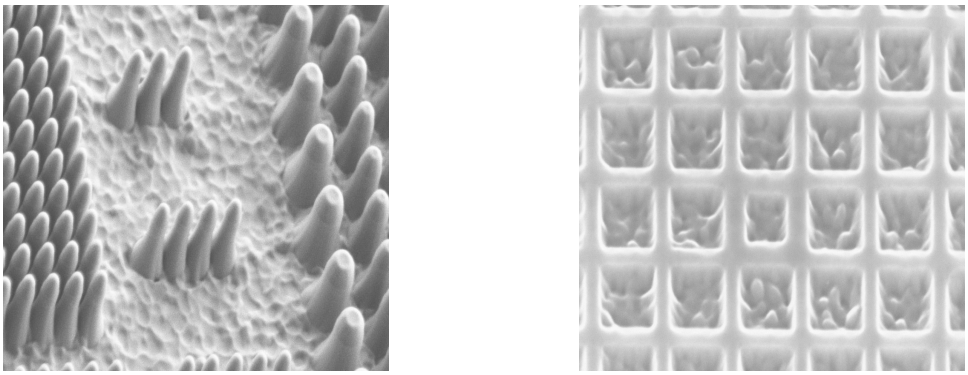

(a) (b)

Figure 7.2: High dose causes both surface roughness and bad sidewall angles in a PC structure that consists of (a) silicon pillars in air and (b) square air-holes in silicon.

Several minutes to several hours are needed when using electron-beam lithography to transfer the pattern to the resist. The electron-beam divides the pattern into many square fields. Each field area is 300 × 300 $\mu m^2$. Longer exposure time is needed when either the total area of the written pattern or the number of exposure fields increases. Field stitching may occur when two or more exposure fields are performed to write a feature. This occurs when the tool fails to align the feature that was written in different exposure fields [3]. As shown in Figure 7.3, the straight waveguide was written in three exposure fields. Due to stitching, we measured high losses in the fabricated waveguides. The separation distance between the scattered light was measured and found to be equal to the electron-beam stage step (300 µm). In order to reduce the stitching effect, the features should be written within the exposure field and away from the corners of the exposure field.

After transferring the pattern on the negative resist, the unexposed areas of the resist are removed by developing the wafer in MIF developer for four minutes. The exposed resist acts as a mask during the etching process to transfer the pattern on the silicon. The mask should be thick enough to protect the underneath features during the etching process. The sidewall angle of a feature is as good as its mask. Chlorine plasma, which

consists of $Cl_2$ and $BCl_3$, is used to etch the unprotected silicon. $Cl_2$ is used to etch silicon while $BCl_3$ is used to remove any native oxide. The mask is not removed after etching silicon because it acts as silicon oxide.

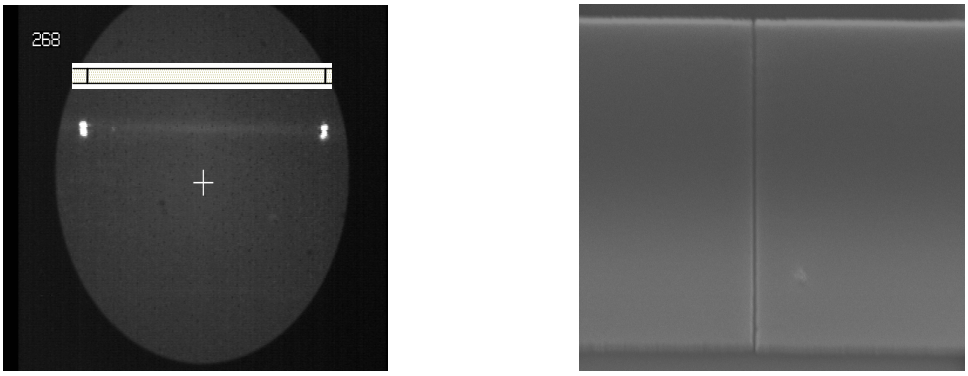


(a) (b)

Figure 7.3: Stitching effect. (a) Micrsocopic image of the scattered light at the locations of stitching. (b) Scanning electron microscope image of the separation distance that is caused by the stitching effect.

After the pattern is transferred onto the silicon, the waveguides are either released or buried in oxide (or metal) depending on the application of the fabricated devices. The waveguides are released by removing part of the oxide layer under the silicon layer using a buffered oxide etchant (BOE) solution for 10 minutes. In order to release a waveguide, the fabricated SOI is spun coated with a positive resist (HPR 504). The resist is exposed using the light of a microscope. The exposed resist is then removed using Cd-26 developer for one minute. Figure 7.4(a) shows the microscopic image of the opening on top of the features that will be released. The etch rate of the BOE solution was 56 nm/min. Figure 7.4(b) shows the scanning electron microscope (SEM) image of the released features.

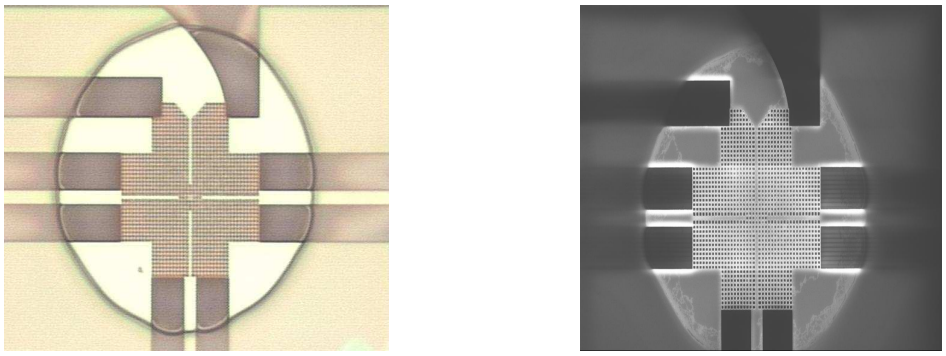

(a) (b)

Figure 7.4: Microsopic image of the photoresist shape (a) after development in Cd-26 and (b) after dipping the device in BOE.

Tetra-ethyl-ortho-silicate (TEOS) oxide and gold are used to cover the fabricated devices. Gold deposition is done using the lift-off process that involves using the bilayer technique. The bottom layer is 495MW PMMA and the top layer is ZEP 520A. The bottom layer is made thicker than that of the top layer to assist removing the deposited gold from the unwanted areas. The top resist is the one that is exposed to the electron-beam when defining the regions where gold is to be deposited. After exposure, the exposed top layer is developed using ZED-N50 for 45 seconds and the underneath layer is developed using methyl isobutyl ketone:isopropanol (MIBK:IPA) for 2 minutes [4]. The top layer is undercut to assist removing the deposited metal. Gold is deposited using an evaporator followed by a lift-off using acetone and methylene chloride.

## 7.2 Dose Test

The exposure dose of an isolated feature is different when it is among other features mainly due to the backscattering of electrons. A dose test is used to find out the required dose or set of doses that are required to write the features in each device. Writing a whole device for a dose test is inefficient and takes a lot of time. To reduce the writing time, a

sample of the device under investigation is written. This sample is repeated many times in which a different dose is used at each time. To find out the required dose or set of doses to write the features, SEM is used to inspect the size and height of the features in each sample after the pattern is transferred to silicon. The dose of the feature that matches the design parameters was used later on to fabricate the actual designed devices with their original size. The dose tests that we performed in this work are for the following structures.

### 7.2.1 Silicon Pillars in Oxide

We selected a sample from the PC structure of silicon pillars in air (as shown in Figure 7.5) to perform the dose test. The circles represent the circular silicon pillars and the rectangles represent the strip waveguides. The sample was repeated 12 times in which a different dose is used at each time. The dose range was from 750 – 2400 $\mu C/cm^2$.

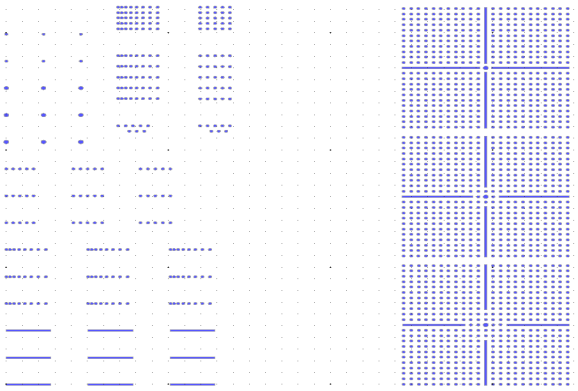

Figure 7.5: Sample of the silicon pillars in air.

Chlorine plasma, which consists of $Cl_2$ and $BCl_3$, was used to etch the unprotected silicon. Different etching recipes were used to find out the one that achieves vertical sidewalls of a height of about one micron without surface roughness. Table 1 shows some of the recipes that were used with SEM images of the transferred pattern. The RF and pressure values were changed in addition to the $Cl_2$ and $BCl_3$ flow rates. The etch time

for all samples was fixed for 7 minutes. The selectivity of silicon to XR-1541 is about 12 to one if the XR-1541 is crosslinked (i.e. transformed to oxide after exposure). We found that the etch rate is low when the pressure is low as shown in recipes (1-4). Also we found that the surface roughness increases when RF = 100 Watts (i.e., maximum operating value of the tool) as shown in recipe # 3. Using $BCl_3$ is important to smooth the sidewalls of the features (compare recipes # 1 and # 2). A faulty recipe may result in a bottle neck shaped or slanted sidewall, as shown in recipe # 5. The optimal recipe is when RF = 70 – 90 Watts, pressure = 20 mtorr, and flow rates of $Cl_2$ and $BCl_3$ are 70 sccm and 2 sccm, respectively (as shown in recipes # 6 and # 7).

Table 7.1: Demonstration of a few etching recipes that were done to find the one that resulted in vertical sidewalls.

| Recipe # | RF [Watts] | Pressure [mtorr] | $Cl_2$ [sccm] | $BCl_3$ [sccm] | SEM Images | Results |
|---|---|---|---|---|---|---|
| 1 | 90 | 5 | 70 | 2 | 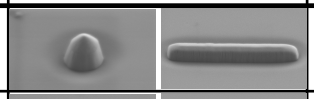 | Sidewall is not vertical. Required feature height was not reached. |
| 2 | 90 | 5 | 70 | 0 | 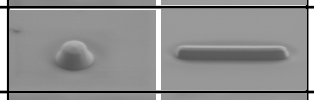 | Sidewall suffers more tapering when $BCl_3$ is not used. Required feature height was not reached. |
| 3 | 100 | 5 | 70 | 2 | 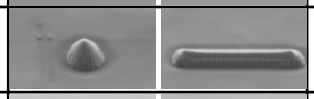 | Surface roughness is high. Required feature height was not reached. |
| 4 | 90 | 10 | 70 | 2 | 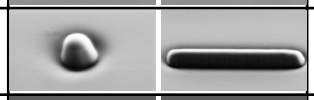 | Sidewall is not straight and vertical. Mask shrinked in lateral direction. Required feature height was not reached. |
| 5 | 90 | 15 | 50 | 2 |  | Sidewall is not vertical. Required feature height was reached. |
| 6 | 70 | 20 | 70 | 2 |  | Sidewall is almost vertical except that the base of the rod is wide. Required feature height was reached. |
| 7 | 90 | 20 | 70 | 2 | 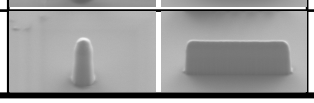 | Best recipe. Reasonable vertical sidewalls of a height of about one micron without surface roughness. |

After fabricating the silicon pillars, the whole device was buried in oxide in order to maximize the photonic band gap and provide index guiding in the vertical direction. We used two methods to do that. One method was by using TEOS oxide (as shown in Figure 7.6(a)) and the other was by using XR-1541 (as shown in Figure 7.6(b)). In the

former method, the oxide covered the top edges of the pillars and closed the spacing between the adjacent pillars. This prevented oxide from reaching the bottom of the pillars. To keep depositing oxide without closing the top was impossible because the spacing between the pillars is small compared to the height of the pillars. In the latter method, the XR-1541 caused a lot of stress that in turn caused a lot of cracks, as shown in Figure 7.6(b). Clearly, the approach that was followed is not suitable to fabricate this device. In the future we will look for another method to deposit oxide.

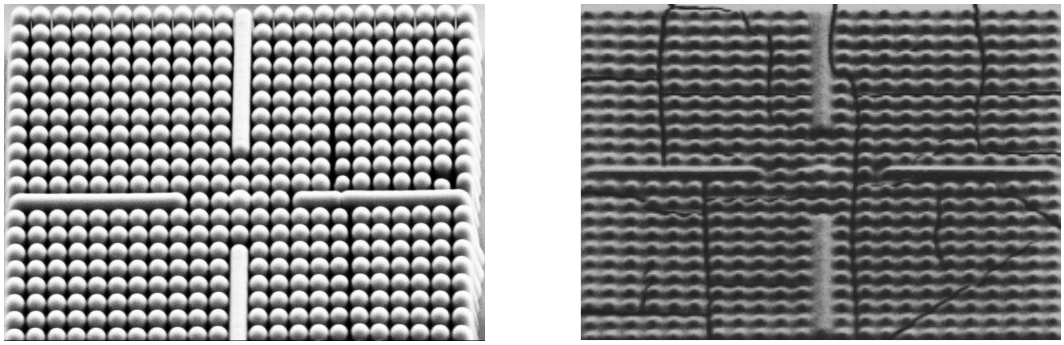

(a) (b)

Figure 7.6: SEM images of silicon pillars after partially covered with (a) TEOS and (b) XR-1541.

### 7.2.2 Square Air-Holes in Silicon

We selected a sample from the PC structure of air-holes in silicon (as shown in Figure 7.7) to perform the dose test. The dose test was performed to find out the required dose to write the square air-holes. The sample was repeated 12 times at different doses. The dose range for the square air-holes was from 750 – 2400 $\mu C/cm^2$. The dose for the input and output silicon waveguides as well as the device holders (blue color in Figure 7.7) was fixed at 700 $\mu C/cm^2$. On the other hand, the dose for the line defect waveguides and the tapered input waveguide (pink color in Figure 7.7) was fixed at 1200 $\mu C/cm^2$.

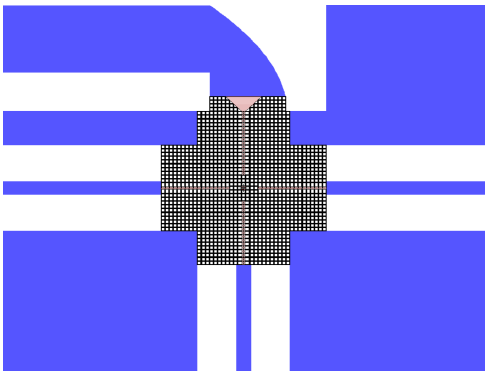

Figure 7.7: Sample of the square air-holes in silicon.

We used the same etch recipe that was used to fabricate the silicon pillars. To release the air-hole structure, the fabricated device was dipped in BOE to etch about 500 nm of the oxide underneath the square-holes. A mask in the form of positive photoresist (HPR 504) was used to protect the places that did not interact with BOE. The photoresist was exposed by using the light from a microscope. A dose test was conducted to find out the shape and dimension of the exposed photoresist area. As shown in Figure 7.8(a), the minimum diameter of the circular opening was about 37 µm. The air-hole structure dimensions were designed to be slightly larger than 37 µm (as shown in Figure 7.8(b)) because BOE is an isotropic etching process in which oxide is removed in the vertical and lateral directions at the same rate.

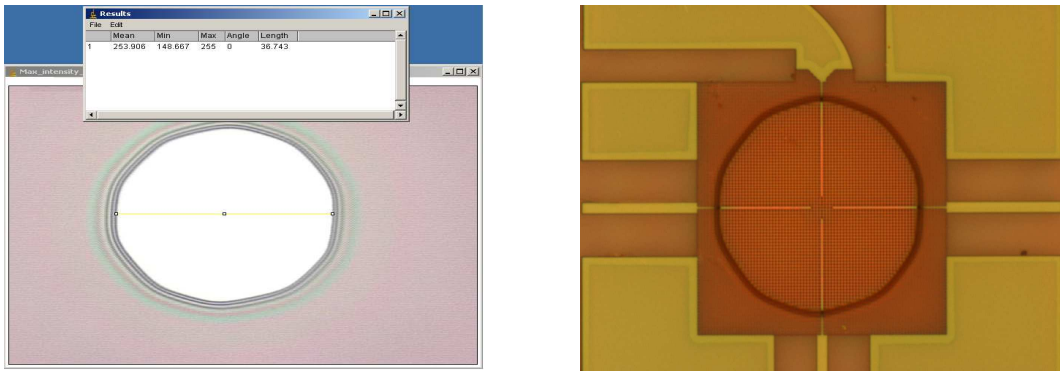


(a) (b)

Figure 7.8: Microscopic image of the opening by using the light from a microscope. (a) Diameter measurement of the circular opening. (b) Circular opening on the top of the air-hole structure.

In general when using the electron-beam lithography, low dose is required for large-feature areas and high dose for small-feature areas. This rule may change based on the geometry of the pattern. Lower dose value is required to write a small feature area that is close to large features than that of a standalone feature. This is because there is back reflection from the electron-beam electrons that were used to write large features. These reflected electrons lower the dose of the areas that are affected. Different doses are required to write the features in our design. We used a dose of 700 $\mu C/cm^2$, 1200 $\mu C/cm^2$, and 1550 $\mu C/cm^2$ to write the input and output waveguides, line defect waveguides and input taper, and the square air-holes, respectively. Figure 7.9(a) shows the SEM image of the square air-hole structure after it was released by using BOE. We found that the PC waveguides fell down because the waveguides were not released at the same time due to the circular opening diameter being smaller than the actual device dimension. To prove that this was the case, we increased the circular opening dimensions to cover the whole air-hole structure in addition to small parts of the waveguides. The SEM image of the released PC waveguides is as shown in Figure 7.9(b). The PC waveguides in this case did not fall down. They began to slope as we moved away from the waveguides towards the central area. A second dose test was carried out after we reduced the size of the air-hole structure to be lower than 37 $\mu m$.

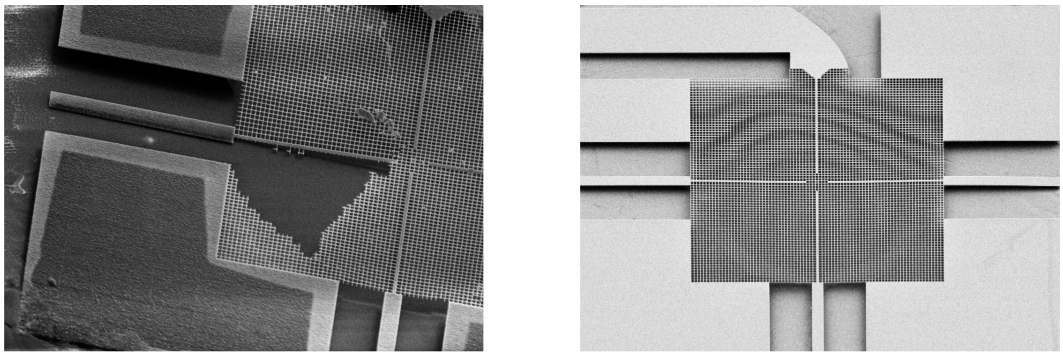

(a) (b)

Figure 7.9: Scanning electron microscope image of the released air-hole structure: (a) when the circular opening did not cover the whole air-hole structure and (b) when the circular opening covered the air-hole structure in addition to some parts of the waveguides.

### 7.2.3 Vertical Ring Coupler

We selected a sample from the vertical microring coupler (as shown in Figure 7.10) to perform the dose test. Two electron-beam lithographies are needed to fabricate these features. The circles represent the microring structure that will be written in the first electron-beam lithography, while the top shape in Figure 7.10 represents the waveguide that will be written on the SOI in the second electron-beam lithography. The sample was repeated 6 times in which a different dose is used at each time. The dose range was from 600 – 1350 $\mu C/cm^2$.

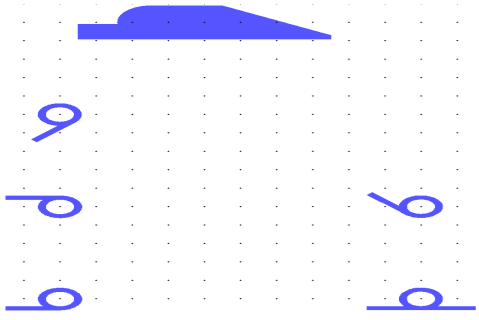

Figure 7.10: Sample of the vertical ring coupler.

We conducted a dose test to find out the required dose to write the vertical ring coupler and the required time to etch the top layer. To do that, we deposited 80 nm of

oxide on top of the SOI wafer. Then we deposited a 5 µm of polysilicon by using the low pressure chemical vapor deposition method. We found that polysilicon has many defects, as shown in Figure 7.11(a). We also found that the mask failed to protect the silicon during etching, as shown in Figures 7.11(b and c).

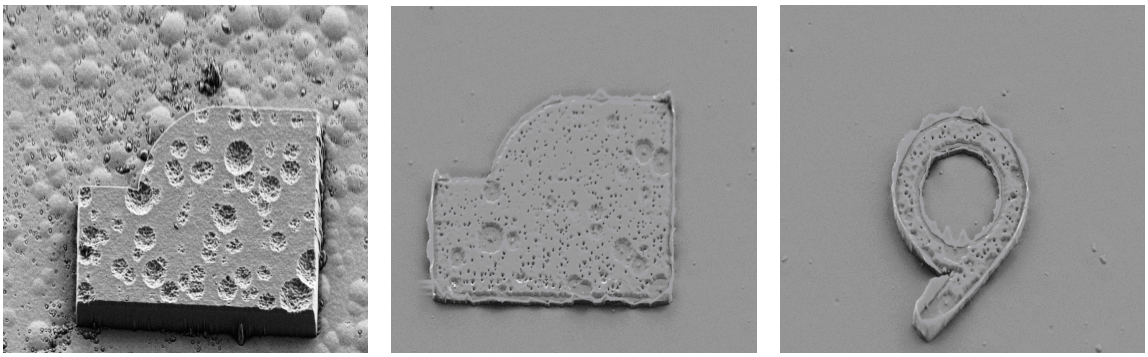

(a) (b) (c)

Figure 7.11: Scanning electron microscope images of: (a) polysilicon defects, (b and c) features height after etching silicon.

We found that two things should be done to fabricate the vertical ring coupler: one is to deposit silicon by using the epitaxial growth method to reduce the number of defects and the other is to reduce the silicon height to less than 2 µm so that the mask will be able to protect the top waveguides during the etching process. If silicon is grown on top of an oxide substrate by the epitaxial method, the resulted silicon is polysilicon with fewer defects than that if polysilicon is deposited. A second dose test was performed for the vertical ring coupler. A buffered oxide of a height of 80 nm was deposited on top of the SOI wafer, followed by the deposition of silicon of a height of 1700 nm by the epitaxial growth method. In order to fabricate the top waveguide including the microring, the wafer was spun coated with a negative resist (XR-1541 22%). The XR-1541 22% should be thick enough to protect the top waveguides during the plasma etch. A maximum film thickness of 845 nm can be achieved when coating a wafer at a speed of 1000 rpm for

one minute. The post bake was done for four minutes to remove solvent from the coated film.

The electron-beam was used to transfer the pattern on the negative resist. A hard bake was done to solidify the XR-1541 film. Next, the unexposed areas of the resist were removed by developing the wafer in MIF developer for 12 minutes. Another hard bake was done to harden the XR-1541. The stress of the XR-1541 film has increased as shown in Figure 7.12(a). Fortunately, the cracks in the XR-1541 film did not cross the written waveguides. Figure 7.12(b) shows the vertical ring coupler after developing the resist for 12 minutes.

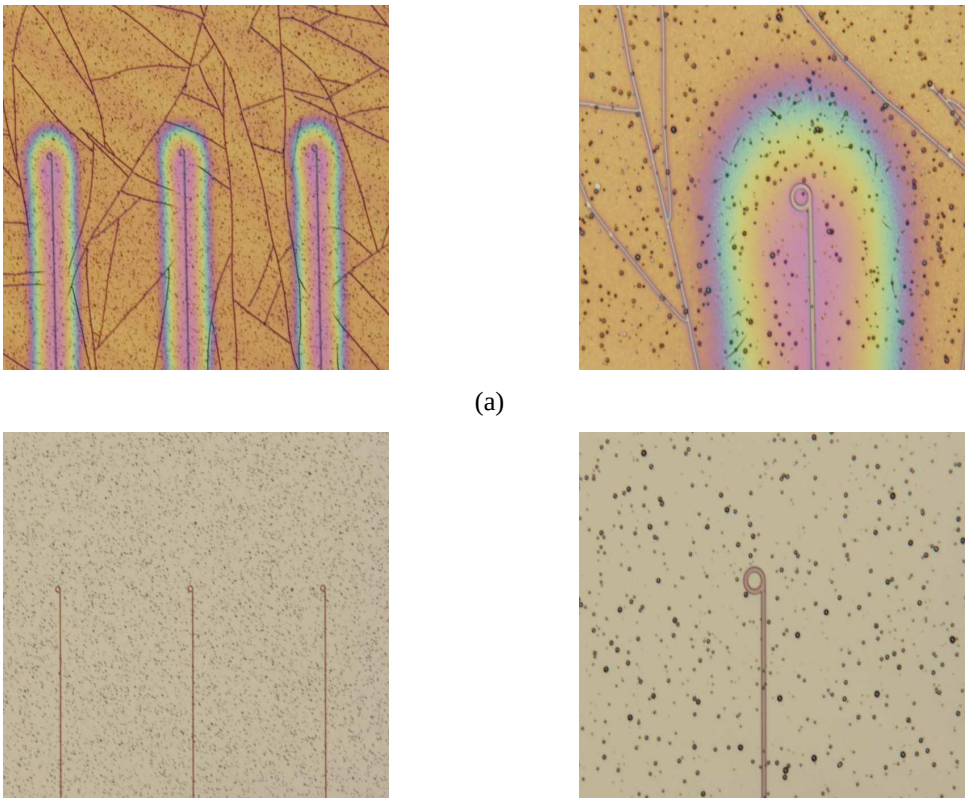

Figure 7.12: Microscopic image of the microring coupler after development the XR-1541 for (a) 4 minutes (with its magnified view of the ring coupler) and (b) 12 minutes (with its magnified view of the ring coupler).

### 7.2.4 Plasmonic Coupler and Splitter

We selected a sample from the plasmonic coupler and splitter (as shown in Figure 7.13) to perform the dose test. The width of the waveguides in Figure 7.13 is either 300 nm (dielectric waveguide) or 40 nm (plasmonic waveguide). The sample was repeated 12 times in which a different dose was used at each time. The dose range was from 750 – 2400 $\mu C/cm^2$.

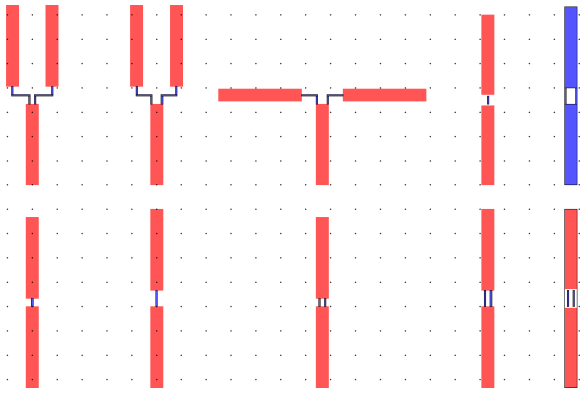

Figure 7.13: Sample of the plasmonic coupler and splitter.

We found that we may use the same dose (1550 $\mu C/cm^2$) to write the dielectric and plasmonic waveguides if the size of the plasmonic waveguide is adjusted to be 20 nm. A width of 20 nm at a dose of 1550 $\mu C/cm^2$ is written as 40 nm. We also found that when the plasmonic waveguide is at the center of the dielectric waveguide, the interface of the dielectric waveguide is rounded (as shown in Figures 7.14(a, b, d, and e). Straight interface between the dielectric and plasmonic waveguide is possible when two plasmonic waveguides are placed at the edges of the dielectric waveguide as shown in Figures 7.14(c and f).

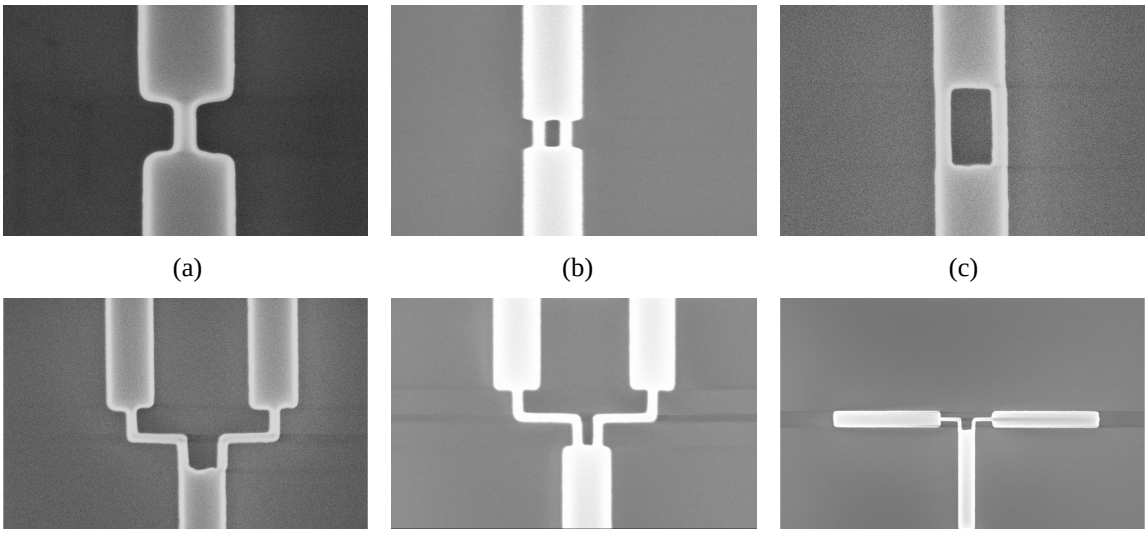

(a) (b) (c)

(d) (e) (f)

Figure 7.14: Scanning electron microscope images of (a-c) coupler and (d-f) splitter designs.

## 7.3 Summary

In this chapter, we presented the methods and processes used to fabricate the devices proposed in this dissertation document.

## References


[1] K. K. Lee, D. R. Lim, L. C. Kimerling, J. Shin, and F. Cerrina, “Fabrication of ultralow-loss Si/SiO2 waveguides by roughness reduction,” Optics Letters, vol. 26, December 2001, pp. 1888-1890.

[2] H. C. Liou and J. Pretzer, “Effect of curing temperature on the mechanical properties of hydrogen silsesquioxane thin films,” Thin Solid Films, vol. 335, December 1998, pp. 186-191.

[3] Cornell NanoScale Science and Technology Facility, Ithaca, NY. Electron beam lithography pattern preparation guidelines and procedures. http://www.cnf.cornell.edu/cnf_process_ebl_patternprep.html (accessed April 2009).

[4] Cornell NanoScale Science and Technology Facility, Ithaca, NY. SPIE handbook of microlithography, micromachining and microfabrication, volume 1: microlithography, section 2.7 resists. http://www.cnf.cornell.edu/cnf_spie7.html (accessed April 2009).

# Chapter 8

# Conclusions and Future Work

In this chapter, we conclude our research work and indicate directions for future work.

## 8.1 Conclusions

Mode mismatch, which is considered one of the obstacles that prevents the multiple applications of the optical integrated circuits, causes radiation and back reflection. In this dissertation, we designed, fabricated and experimentally demonstrated different couplers to achieve mode matching between waveguides of different geometries and propagation mechanisms. The three main types of waveguides that were involved in our work were: the conventional optical waveguides, the photonic crystal (PC) waveguides, and the plasmonic waveguides.

In Chapter 3, we proposed two engineering methodologies that provide higher coupling efficiency between a dielectric waveguide and a tapered planar PC waveguide than what has been reported in the literature. The proposed methods achieve mode

matching by introducing structural imperfections to change the mode size and shape inside the taper to match that of the line defect waveguide. In method one, we showed the importance of changing the size and position of each inner taper rod in increasing the coupling efficiency. Each inner taper rod is treated as matching impedance that is tuned by changing its size and position until maximum coupling is reached. The maximum coupling efficiency at 1.55 μm from the size change method was above 88%, while it was above 94% from the position change method. By combining the effect of the size and position change methods, we found that the order of which method to apply first is important because the wave faces different scattering mechanisms in each case. Our results show that applying the size change method, followed by the position change method, increased the coupling efficiency to about 96% without affecting the transmission spectrum of the coupler. In method two, we presented a hybrid PC structure that increases mode coupling. Series of cavities were introduced next to the upper taper rods' position from both sides before the inner taper rods' positions were changed, achieving over 94% power transmission at the end.

In Chapter 4, we used a resonant cavity at the intersection area between two intersecting waveguides to reduce the crosstalk into the intersected waveguides. The key idea is to excite modes orthogonal to each other at the intersection area. The resonant cavity used in our design is shown to be very compact. Three PC structures are studied: one consists of cylindrical silicon-rods in air, another consists of cubic silicon-rods in air, and the other consists of cubic air-holes in silicon. In the former structure, the quality factor of the cavity increases by replacing the line defect waveguides with the dielectric strip waveguides. Based on the two-dimensional simulation results, we found that the

“3 × 3” structure with the strip waveguides achieved crosstalk reduction of 21 dB lower than that achieved without using the strip waveguides. We also found that more crosstalk reduction could be achieved by reducing the spacing between the strip waveguide and the cavity. The overall crosstalk reduction for the “5 × 5”, “3 × 3”, and “1 × 1” structures was -91 dB, -76 dB, and -44 dB, respectively. The measured crosstalk values for the two latter structures are two times lower (in dB) than those reported in the literature. Replacing the cylindrical rods by cubic ones resulted in wider spectrum and less crosstalk. We found that more than -19 dB of crosstalk reduction can be achieved by applying the space reduction method. The overall crosstalk reduction for the “5 × 5”, “3 × 3”, and “1 × 1” structures was -105 dB, -90 dB, and -43 dB, respectively. Finally, the image reversal of the cubic rods (i.e., air-holes in silicon) was fabricated and tested. We experimentally showed that the crosstalk reduction of the “7 × 7” and “3 × 3” air-hole structures is about -20 dB and -10 dB, respectively. The experimental results exhibited similar performances to those predicted by the numerical simulations.

In Chapter 5, silicon-to-silicon couplers were proposed to couple light from optical fiber into SOI waveguides based on microring vertical couplers. Our simulation results show that the couplers have very high efficiency. A semi-disk was proposed to control the propagation direction of the coupled light in the SOI waveguide and to assist the mode conversion. The microring coupler was fabricated and tested to confirm the analytical results.

In Chapter 6, we showed that a matching coupler at the interface between a dielectric waveguide and a plasmonic waveguide can be designed to increase the coupling efficiency and improve the alignment tolerance. Based on the coupler, we designed a

nano-scale plasmonic splitter with a coupling efficiency of 45% for each branch that operates at the optical telecom wavelength. The splitting ratio can be controlled by either varying the position or width of the two branches. We also presented two potential applications of our proposed coupler and splitter in both the directional couplers and Mach-Zehnder interferometers (MZIs). The two devices are embedded between two dielectric waveguides. The overall efficiency was 37% for a 2 × 2 directional coupler switch and above 50% for the proposed designs for a MZI. Finally, the plasmonic air-slot coupler and the plasmonic splitter were fabricated and tested. The experimental results exhibited similar performances to those predicted by the numerical simulations.

## 8.2 Future Work

To extend our research, we propose the following work:

- In Chapter 4, we presented the experimental results of the crosstalk structure that consists of square air-holes in silicon. The coupling efficiency was poor because there was a mode mismatch between the line defect waveguide (width of 448 nm) and the output dielectric waveguide (width of 2 µm). Also, the bends that we used in our design have a width of 2 µm that caused high losses because of the interference between the fundamental mode and the higher order modes supported by the waveguide. The coupling efficiency can be increased by either adding J-couplers at all the output ports (as shown in Figure 8.1(a)) or by changing the width of the input and output dielectric waveguides to match that of the line defect waveguides (as shown in Figure 8.1(b)). The J-coupler is expected to increase the coupling efficiency, but its fabrication price will be almost four times

the price of fabrication of the structure shown in Figure 8.1(b). That is why we recommend the fabrication of the structure shown in Figure 8.1(b). Scanning electron microscope image of the proposed structure is shown in Figure 8.1(c).

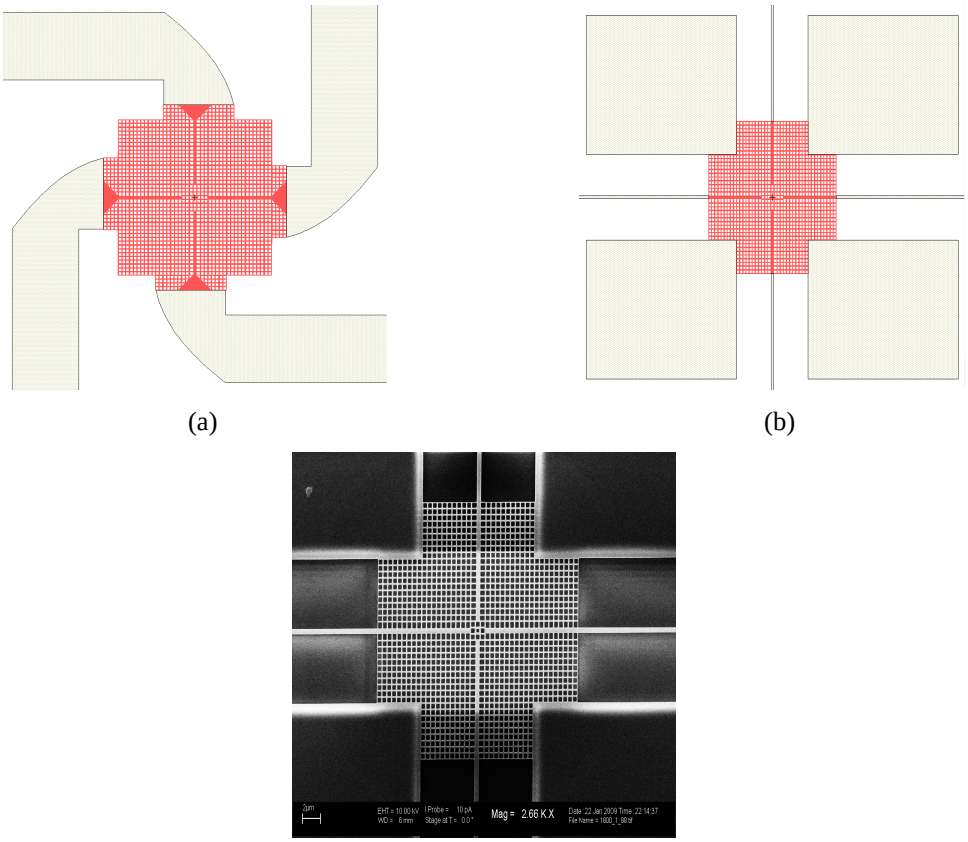

(a) (b)

(c)

Figure 8.1: Schematic of the proposed design for the crosstalk structure that can be used to increase the coupling efficiency by either (a) using a J-coupler for all the input and output waveguides or (b) by making the width of the input and output waveguides equal to that of the line defect waveguide. (c) Scanning electron microscope image of the fabricated structure that is shown in Figure 8.1(b).

- In Chapter 5, we presented the experimental results of the vertical microring coupler. We believe that the coupling efficiency was not much higher than that of the reference silicon-on-insulator (SOI) waveguide because of three main reasons. First, the deposited silicon (top layer) has many defects which caused back reflection and radiation losses. These defects are the result of depositing epitaxial silicon on top of an oxide layer. Second, tapering the 18 µm SOI waveguide

underneath the microring to 2 µm over a length of 3 mm caused high propagation losses. Third, the thickness of the oxide layer between the microring coupler and the SOI waveguide is somewhat thick (80 nm) that prevented more light from coupling into the SOI waveguide. The coupling efficiency can be increased by fabricating the structure (shown in Figure 8.2) in which the following conditions are met: the width of the SOI waveguide is reduced at the overlap area to about 13 µm, the tapering length of the SOI waveguide is about 1 mm, and the thickness of the deposited oxide is reduced to about 50 nm.

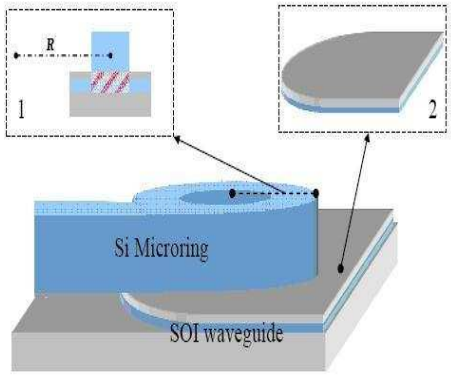


Figure 8.2: Schematic of the microring coupler.

- In Chapter 6, we presented the experimental results of the plasmonic air-slot coupler and splitter. The fabrication process involved the use of the focused ion beam (FIB) to define the air-slot waveguides. The FIB introduced gallium ions into the waveguides in addition to milling some of the gold layer during the alignment process. Consequently, the losses were high. The fabrication process can be simplified by replacing the air-slot waveguides with silicon waveguides (as shown in Figure 8.3). These waveguides are buried in gold to form the plasmonic splitter branches.

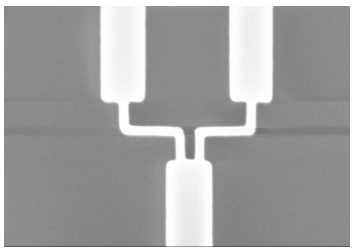

Figure 8.3: Schematic of the proposed plasmonic splitter.

## 8.3 Summary

In this chapter, we concluded our research work and indicated future research directions for this dissertation.

# APPENDIX A

## Crosstalk Reduction in Square Cavities

This appendix provides a copy of the following publication[1]:

R. A. Wahsheh, Z. Lu, and M. A. G. Abushagur, "Cross talk reduction in square cavities," IEEE Photonics Journal, vol. 1, September 2009, pp. 191-196.

[1]Reprinted from IEEE Photonics Journal, vol. 1, R. A. Wahsheh, Z. Lu, and M. A. G. Abushagur, "Cross talk reduction in square cavities," September 2009, pp. 191-196, Copyright 2009, with permission from IEEE.

# Crosstalk Reduction in Square Cavities

**Rami A. Wahsheh, Zhaolin Lu, and Mustafa A. G. Abushagur**

Microsystems Engineering, Kate Gleason College of Engineering,
Rochester Institute of Technology, Rochester, NY 14623 USA

*DOI: 10.1109/JPHOT.2009.2031621*
*1943-0655/$26.00 ©2009 IEEE*

Manuscript received July 18, 2009; revised August 10, 2009. First published Online August 31, 2009. Current version published September 18, 2009. Corresponding author: Z. Lu (e-mail: zxleen@rit.edu).

**Abstract:** Theoretically and experimentally, we demonstrate that low crosstalk between two crossed line-defect waveguides formed in a square lattice photonic crystal (PC) structure can be achieved using a resonant cavity at the intersection area. The PC resonator consists of cubic air-holes in silicon air-holes. The Q-factor of the cavity can be changed by increasing the number of holes that form the cavity. The theoretical and experimental crosstalk results are about −40 dB and −20 dB, respectively.

**Index Terms:** Waveguides, photonic crystals.

## 1. Introduction

When waveguides are crossed, guided waves suddenly expand due to the lack of confinement in the lateral direction. This results in coupling into the intersecting waveguides in addition to radiation and scattering losses. Ultra-low crosstalk between intersecting waveguides is required in optical integrated circuits in order to minimize the required area to produce multiple optical devices on the same chip. Low crosstalk is also beneficial for improving bit rate in optical communications systems. Recent work has shown that crosstalk between photonic devices can be reduced to a much smaller degree than that between their electronic counterparts [1]. However, the low crosstalk essentially relies on designing innovative photonic structures. More recently, a number of structures have been proposed and investigated to eliminate crosstalk [2]–[7]. One method that has attracted great attention is based on cavity coupling that can achieve low crosstalk over a wide spectrum [3]–[7]. The key idea is to excite modes orthogonal to each other at the intersection area. Johnson *et al.* [3] proposed a resonant cavity that supported two orthogonal modes at the intersection area of two line-defect waveguides in a two-dimensional (2-D) square lattice photonic crystal (PC) structure, which was composed of periodic cylindrical rods in air. In the work of Johnson *et al.* [3], as the quality factor (Q-factor) of the cavity increased by adding more rods next to the defect rod, crosstalk could be reduced. As a result of the Q-factor change, both the output bandwidth spectrum and crosstalk are controlled. Based on a similar structure, Liu *et al.* [4] reported crosstalk reduction by using two single-mode coupled resonator optical waveguides that had a nonoverlapping photonic band gap (PBG). Their results are very attractive and promising. Furthermore, all-optical transistors can potentially be achieved based on the PC cross-waveguide geometry [8]. However, in both works of Johnson *et al.* [3] and Liu *et al.* [4] the structures had an infinite thickness and light was guided in air, or void PBG waveguides, instead of dielectric waveguides. As a result, the structures are only ideal 2-D models that cannot be experimentally realized.

In order to experimentally demonstrate the structure proposed by Johnson *et al.* [3], Roh *et al.* [5] used two aluminum metal plates to insure confinement in the out-of-plane direction. One plate was placed on the top, and the other was placed at the bottom of the cylindrical alumina rods in air. Crosstalk reduction as large as −30 dB was experimentally achieved at the resonant frequency.

However, this metallic-cladding structure can not be scaled down for telecom wavelengths. To work for the telecom wavelengths, Teo *et al.* [6] fabricated a structure that was composed of 13-$\mu$m-high silicon rods in air, which are too high to provide effective out-of-plane field confinement. For practical applications, a widely used way is to convert a 2-D structure into a planar structure. Unfortunately, in a planar structure light cannot be confined in void PBG waveguides without out-of-plane confinement on light propagation.

In our previous work [7], we proposed transverse mode planar structures in a square lattice of silicon pillars for telecom wavelengths. We replaced the void PBG waveguides in the structures proposed by Johnson *et al.* [1] with dielectric strip waveguides to achieve out-of-plane field confinement. Herein, we propose transverse electric (TE) planar structures in a square lattice of air-holes in silicon for telecom wavelengths. The slab waveguide achieves the out-of-plane confinement by total internal reflection. To illustrate the effectiveness of our design, we performed a series of simulations. First, the Q-factor of the cavity was increased by adding more air-holes next to the defect air-hole. Then, the optimized devices were fabricated on silicon-on-insulator (SOI) wafers. The fabrication process details and experimental results are described.

## 2. Intersection Design

In order to achieve low crosstalk for TE modes, we propose a 2-D square lattice PC structure composed of square air-holes in silicon of a width of 0.8$a$ ($a$ is the lattice constant of the PCs). The TE PBG of the structures is between $0.34(a/\lambda)$ and $0.41(a/\lambda)$ as shown in Fig. 1(c). Two intersecting line-defect waveguides are created by replacing a row and a column of air-holes with a slab waveguide, as shown in Fig. 1(a) and (b). The slab waveguides have a width of 0.8$a$ as that of the bulk air-holes. The resonant cavity at the center of the intersection is introduced by creating a defect air-hole of a width of 0.6$a$ that has a resonant frequency of about $0.4(a/\lambda)$, as shown in Fig. 1(c). Fig. 1(d) shows the mode excited in a square lattice PC along the horizontal axis. Another orthogonal mode can be excited along the vertical axis. The Q-factor of the cavity is increased by increasing the number of air-holes next to the defect. The following names are given to the structures that are shown in Fig. 1 to denote the number of airholes that form the cavity: "7 $\times$ 7" and "3 $\times$ 3" for the structures that have seven air-holes and three air-holes along the row or column of the intersection area, respectively.

## 3. Numerical Results

The 2-D finite-difference time-domain method is used to analyze all the structures introduced in this paper. Each structure is terminated by a perfectly matched layer in order to reduce the back reflection from the waveguide ends. A broadband TE Gaussian pulse is used as a light source. Two detectors are used to measure the forward (throughput) and crosstalk coupling powers, as shown in Fig. 1(a). The measured power is plotted as a function of frequency. A linear scale is used for the forward power measurement while a log scale is used for the crosstalk measurement.

The cavity size is changed by increasing the number of air-holes that form the cavity. As shown in Fig. 2, we found that the measured throughput values for the "7 $\times$ 7," "3 $\times$ 3," and "1 $\times$ 1" structures are 85%, 82%, and 34%, while the crosstalk values at resonance are $-40$, $-22$, and $-10$ dB, respectively. The Q-factor for the "7 $\times$ 7," "3 $\times$ 3," and "1 $\times$ 1" structures are 250, 30, and 5, respectively. As the Q-factor increases, both the throughput spectrum and crosstalk decrease.

## 4. Fabrication Process and Experimental Results

We fabricated the optimized "7 $\times$ 7" and "3 $\times$ 3" structures on SOI platform using e-beam lithography. The scanning electron microscope (SEM) image of the fabricated "7 $\times$ 7" structures is shown in Fig. 3. According to three-dimensional simulations, we found that in order to have a band gap centered at 1480 nm, the height of the air-hole should be 250 nm, and the lattice constant should be 560 nm. To fabricate the optimized devices, the SOI wafer was spun coated with a negative resist (XR-1541). Then, the e-beam was used to transfer the pattern on the negative resist.

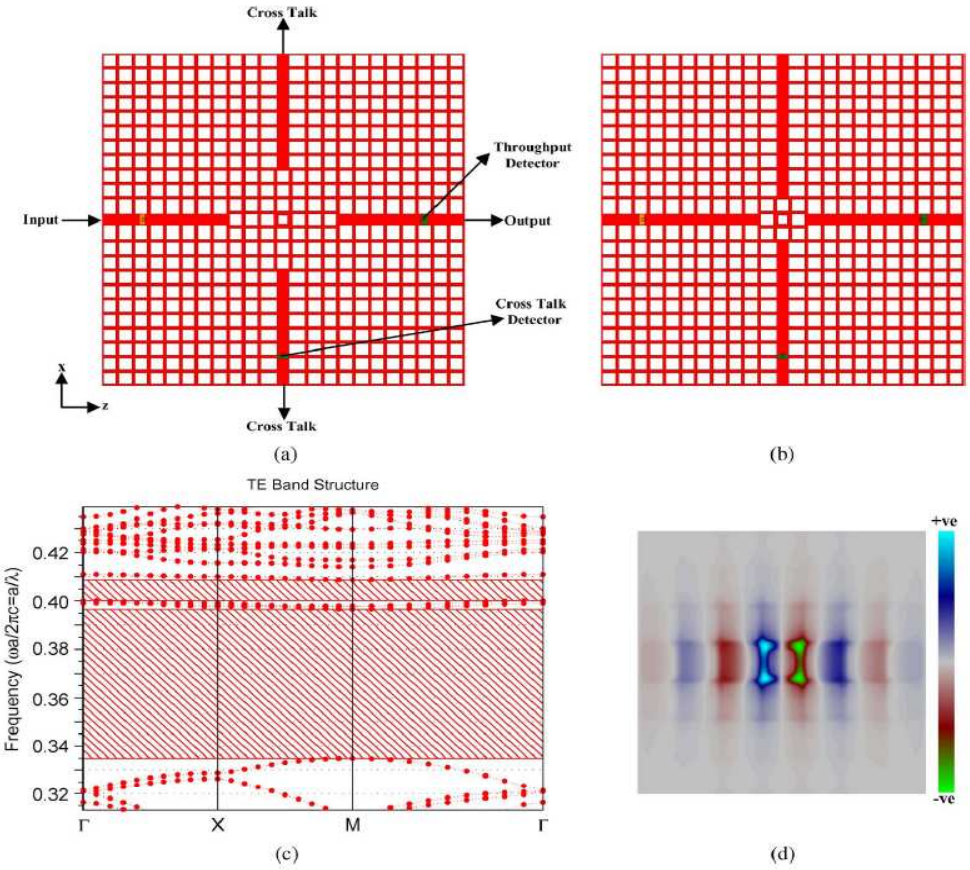


Fig. 1. Two-dimensional photonic crystal structures of square air-holes in silicon for the following cavity sizes: (a) "7 × 7" cavity size and (b) "3 × 3" cavity size. (c) TE band diagram. (d) Field pattern inside the cavity.

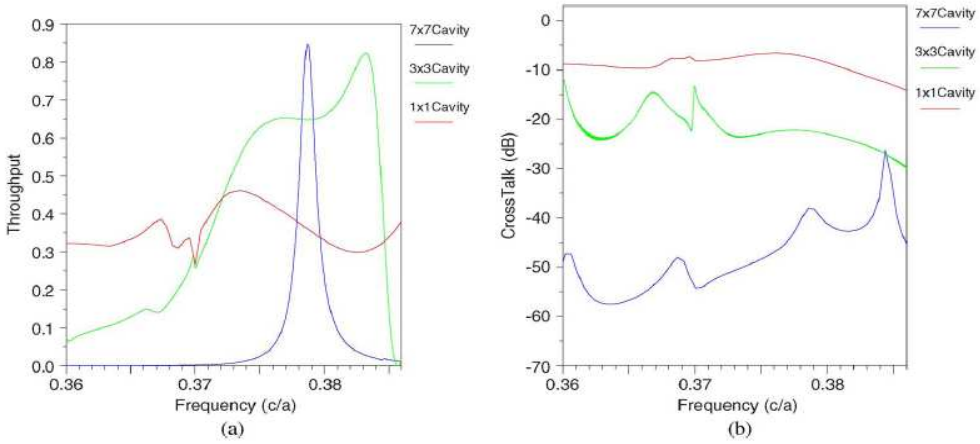


Fig. 2. Comparison of the (a) throughput and (b) crosstalk for the "7 × 7," "3 × 3," and "1 × 1" structures of cubic air-holes in silicon.

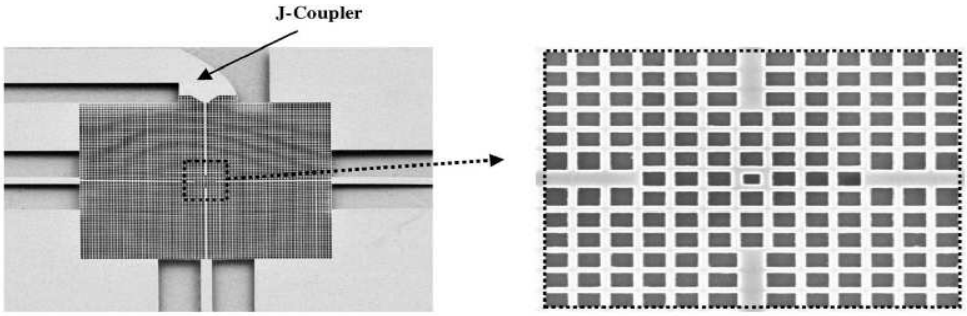


Fig. 3. SEM image of the fabricated "7 × 7" PC structure. (a) PC structure and the testing platform, which consists of a J-coupler and three waveguides. (b) Close-up image of the "7 × 7" PC cavity.

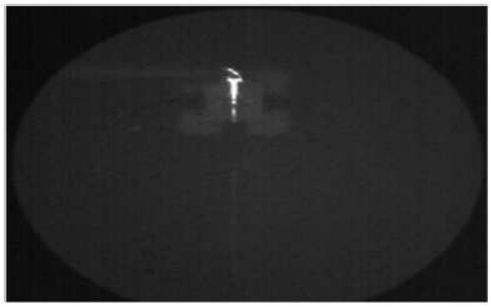

Fig. 4. Microscopic image of the cavity at resonance.

Next, the unexposed areas of the resist were removed by developing the wafer in AZ® 300 MIF (metal-ion-free) developer for 4 minutes. The exposed resist acted as a mask during the etching process. Chlorine plasma, which consists of $Cl_2$ and $BCl_3$, was used to etch the unprotected silicon. The mask was not removed after etching silicon because it acted as silicon oxide. Finally, the buried oxide under the air-holes was etched using a buffered oxide etchant solution for 10 minutes. In order to be able to test the PC cavity a testing platform was fabricated at the same time. It is made of a holder to carry the PC device, a J-coupler [9] to couple the light effectively from an optical fiber into the PC and three waveguides to couple the light out of the device.

We tested the fabricated "7 × 7" and "3 × 3" TE devices. The experimental measurement set up was as follows: the light from a tunable laser with spectral range from 1260 nm to 1520 nm propagated through a polarization controller to allow TE-like modes to couple into a 10-$\mu$m silicon waveguide. Coupling into and out of the silicon waveguides was achieved using tapered micro-lens fibers with a spot diameter of $2.5 \pm 0.5$ $\mu$m. A J-coupler was fabricated and used to couple light from the 10-$\mu$m silicon waveguide into the 448-nm PC line-defect waveguide. Translational stages were used to align the input and output fibers to the device under testing. An infrared camera mounted on a microscope was used to capture the vertically scattered light from the waveguides. The output power was measured using an infrared detector and recorded using a power meter. A microscopic image of a cavity at resonance is shown in Fig. 4.

A comparison between the experimental and simulation results of the "7 × 7" and "3 × 3" structures are shown in Fig. 5. The Fabry Perot oscillations are formed by the reflection from the end-facets of the waveguides and the cavity. In our simulations, the light source, the output detector, and the crosstalk detector are all placed inside the PC line-defect waveguides. In our experiment, the light source and detector are out of the SOI chip. To be able to compare the

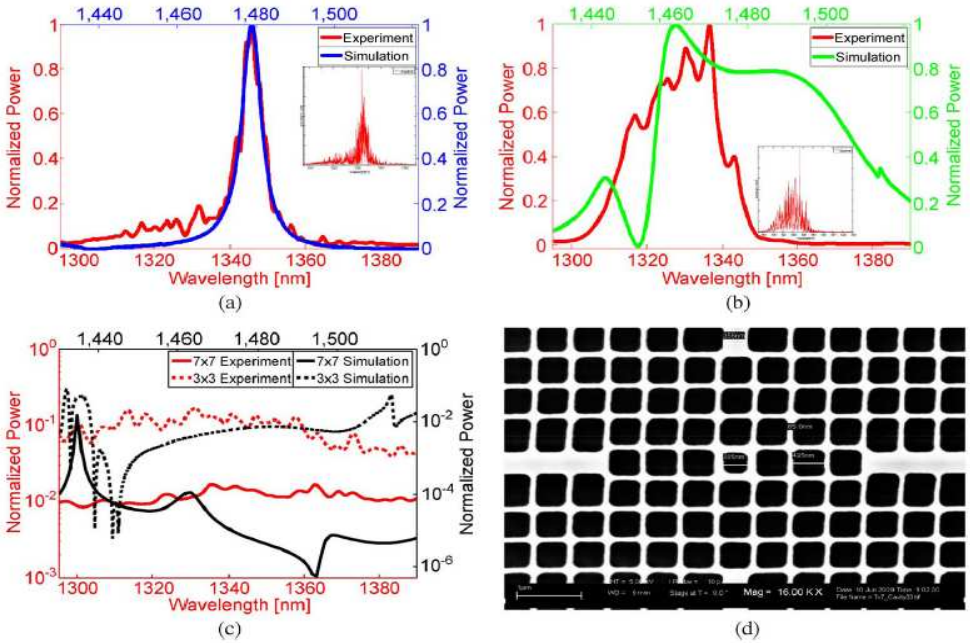


Fig. 5. Comparison of experimental results with simulation results of (a) throughput "7 × 7" structure and (b) throughput "3 × 3" structure. The inset shows the unfiltered transmission measurements. (c) Crosstalk "7 × 7" and "3 × 3" structures. (d) SEM image of the tested "7 × 7" structure that shows the measured widths of the bulk crystals and defect.

simulation with the experiment, both results should be normalized to one. Also, the resonant frequency in both results should match. As expected from simulation and theory, as the size of the cavity increases, the Q-factor and the crosstalk decreases. The Q-factor and crosstalk value for the fabricated "7 × 7" structure [see Fig. 5(a) and (c)] is 168 and −20 dB and that of the "3 × 3" structure [see Fig. 5(b) and (c)] is 54 and −10 dB. The measured Q-factors and crosstalk values are slightly different from that resulted from the numerical simulations. This is due to fabrication errors. From the plots in Fig. 5, it is clear that the resonance frequency is shifted for the experimental results from that predicted by the simulation results. Based on the 2-D simulation results, to get a shift in the resonance frequency from 1480 nm to 1345 nm requires that the widths of the fabricated square air-holes and defect be wider than that used in the simulation by about 5% (i.e., lattice constant is still the same (i.e., $a = 560$ nm), square air-holes of a width of $0.842a$, and a defect Air-hole of a width of $0.642a$). However, based on the measured values using the SEM for the tested "7 × 7" device [see Fig. 5(d)], the measured widths of the bulk square air-holes and cavity defect are wider than that predicted by simulation by about 5% (i.e., lattice constant is still the same (i.e., $a = 560$ nm), square air-holes of a width of $0.884a$, and a defect air-hole of a width of $0.688a$). The difference between the simulation and the measured values is because we did a 2-D simulation which does not take into consideration the out-of-plane effect. The measured spectrum of the throughput for the "7 × 7" cavity matches very well the simulation data, taking into account the shift of the resonance frequency, as shown in Fig. 5(a). The measured spectrum of the throughput for the "3 × 3" cavity has the bandpass in the same range of frequencies but exhibited a narrower spectrum, a higher Q [as shown in Fig. 5(b)]. This is very well expected because of the sensitivity of the devices due to any fabrication tolerance. However, the fabrication error is not the same for both the defect air-hole and the bulk air-holes. As a result of that, the Q-factor of the fabricated "3 × 3" is higher than that of simulation which is evident in its narrower spectrum. Practically speaking the throughputs of the devices were quite close to the simulation predictions. The crosstalk experimental curves show consistently that the "7 × 7" cavity has lower crosstalk values than

that of the "3 × 3" as predicted by the simulation data. The crosstalk simulation results show stronger wavelength dependence than the experimental results, Fig. 5(c), which is might be due in the major part to the low sensitivity and narrow dynamic range of the photodetector used in the experiment.

## 5. Conclusion

We designed, fabricated, and experimentally demonstrated two intersecting waveguides formed in a square lattice PC structure. The proposed structures provide index guiding and confinement in the vertical direction. We have fabricated several different variations of the devices where the waveguides are separated by a different number of air-holes to improve the coupling efficiency and reduce the crosstalk. We experimentally showed that the crosstalk reduction of the "7 × 7" and "3 × 3" air-hole structures is about −20 dB and −10 dB, respectively. The experimental results exhibited similar performance to those predicted by the numerical simulations.

## References

[1] R. G. Hunsperger, *Integrated Optics: Theory and Technology*. Berlin, Germany: Springer-Verlag, 2002.
[2] W. Bogaerts, P. Dumon, D. V. Thourhout, and R. Baets, "Low-loss, low-cross-talk crossings for silicon-on-insulator nanophotonic waveguides," *Opt. Lett.*, vol. 32, no. 19, pp. 2801–2803, Oct. 2007.
[3] S. G. Johnson, C. Manolatou, S. Fan, P. R. Villeneuve, J. D. Joannopoulos, and H. A. Haus, "Elimination of cross talk in waveguide intersections," *Opt. Lett.*, vol. 23, no. 23, pp. 1855–1857, Dec. 1998.
[4] T. Liu, M. Fallahi, M. Mansuripur, A. R. Zakharian, and J. V. Moloney, "Intersection of nonidentical optical waveguides based on photonic crystals," *Opt. Lett.*, vol. 30, no. 18, pp. 2409–2411, Sep. 2005.
[5] Y. G. Roh, S. Yoon, H. Jeon, S. H. Han, and Q. H. Park, "Experimental verification of cross talk reduction in photonic crystal waveguide crossings," *Appl. Phys. Lett.*, vol. 85, no. 16, pp. 3351–3353, Oct. 2004.
[6] S. H. G. Teo, A. Q. Liu, J. B. Zhang, and M. H. Hong, "Induced free carrier modulation of photonic crystal optical intersection via localized optical absorption effect," *Appl. Phys. Lett.*, vol. 89, no. 9, pp. 091910.1–091910.3, Aug. 2006.
[7] R. A. Wahsheh, Z. Lu, M. A. G. Abushagur, and S. F. Preble, "Ultra low cross talk in crossed strip waveguides with the assistance of a photonic crystal cavity," in *Proc. SPIE*, 2008, vol. 7056, p. 70560E.
[8] M. F. Yanik, S. Fan, M. Soljačić, and J. D. Joannopoulos, "All-optical transistor action with bistable switching in a photonic crystal cross-waveguide geometry," *Opt. Lett.*, vol. 28, no. 24, pp. 2506–2508, Dec. 2003.
[9] D. W. Prather, J. Murakowski, S. Shi, S. Venkataraman, A. Sharkawy, C. Chen, and D. Pustai, "High-efficiency coupling structure for a single-line-defect photonic-crystal waveguide," *Opt. Lett.*, vol. 27, no. 18, pp. 1601–1603, Sep. 2002.
[10] C. Manolatou, S. G. Johnson, S. Fan, P. R. Villeneuve, H. A. Haus, and J. D. Joannopoulos, "High-density integrated optics," *J. Lightw. Technol.*, vol. 17, no. 9, pp. 1682–1692, Sep. 1999.

# APPENDIX B

## Nanoplasmonic Couplers and Splitters

This appendix provides a copy of the following publication[1]:

R. A. Wahsheh, Z. Lu, and M. A. G. Abushagur, "Nanoplasmonic couplers and splitters,"

Optics Express, vol. 17, October 2009, pp. 19033-19040.

[1]Reprinted from Optics Express, vol. 17, R. A. Wahsheh, Z. Lu, and M. A. G. Abushagur, "Nanoplasmonic couplers and splitters," October 2009, pp. 19033-19040, Copyright 2009, with permission from Optical Society of America.

# Nanoplasmonic couplers and splitters

**Rami A. Wahsheh, Zhaolin Lu * and Mustafa A. G. Abushagur**

*Microsystems Engineering, Kate Gleason College of Engineering,*
*Rochester Institute of Technology, Rochester, New York 14623, USA*
**zxleen@rit.ed*

**Abstract:** In this paper, we present novel designs and analysis of ultra-compact couplers and 1 x 2 splitters based on plasmonic waveguides. Numerical simulation shows coupling efficiency up to 88% for the former one and 45% for each branch for the latter one. The proposed coupler design has the advantages of improving the alignment tolerance of the plasmonic waveguide with respect to the dielectric waveguide and broadening the spectrum response of the splitter.



**OCIS codes:** (130.3120) Integrated optics devices; (230.7370) Waveguides; (240.6680) Surface plasmons.

## References and links

1. W. L. Barnes, A. Dereux, and T. W. Ebbesen, "Surface plasmon subwavelength optics," Nature **424**(6950), 824–830 (2003).
2. R. Zia, M. D. Selker, P. B. Catrysse, and M. L. Brongersma, "Geometries and materials for subwavelength surface plasmon modes," J. Opt. Soc. Am. **21**(12), 2442–2446 (2004).
3. E. N. Economou, "Surface plasmons in thin films," Phys. Rev. **182**(2), 539–554 (1969).
4. D. F. P. Pile, T. Ogawa, D. K. Gramotnev, Y. Matsuzaki, K. C. Vernon, K. Yamaguchi, T. Okamoto, M. Haraguchi, and M. Fukui, "Two-dimensionally localized modes of a nanoscale gap plasmon waveguide," Appl. Phys. Lett. **87**(26), 261114 (2005).
5. R. Coccioli, M. Boroditsky, K. W. Kim, Y. Rahmat-Samii, and E. Yablonovitch, "Smallest possible electromagnetic mode volume in a dielectric cavity," IEE Proc., Optoelectron. **145**(6), 391–397 (1998).
6. G. Veronis, and S. Fan, "Theoretical investigation of compact couplers between dielectric slab waveguides and two-dimensional metal-dielectric-metal plasmonic waveguides," Opt. Express **15**(3), 1211–1221 (2007).
7. P. Ginzburg, and M. Orenstein, "Plasmonic transmission lines: from micro to nano scale with λ/4 impedance matching," Opt. Express **15**(11), 6762–6767 (2007).
8. D. F. P. Pile, and D. K. Gramotnev, "Adiabatic and nonadiabatic nanofocusing of plasmons by tapered gap plasmon waveguides," Appl. Phys. Lett. **89**(4), 041111 (2006).
9. P. Ginzburg, D. Arbel, and M. Orenstein, "Gap plasmon polariton structure for very efficient microscale-to-nanoscale interfacing," Opt. Express **31**, 3288–3290 (2006).
10. R. Charbonneau, N. Lahoud, G. Mattiussi, and P. Berini, "Demonstration of integrated optics elements based on long-ranging surface plasmon polaritons," Opt. Express **13**(3), 977–984 (2005).
11. R. Charbonneau, C. Scales, I. Breukelaar, S. Fafard, N. Lahoud, G. Mattiussi, and P. Berini, "Passive integrated optics elements based on long-range surface plasmon polaritons," J. Lightwave Technol. **24**(1), 477–494 (2006).
12. C. Manolatou, S. G. Johnson, S. Fan, P. R. Villeneuve, H. A. Haus, and J. D. Joannopoulos, "High-density integrated optics," J. Lightwave Technol. **17**(9), 1682–1692 (1999).
13. J. S. Jensen, and O. Sigmund, "Topology optimization of photonic crystal structures: A high-bandwidth low-loss T-junction waveguide," J. Opt. Soc. Am. B **22**(6), 1191–1198 (2005).
14. G. Veronis, and S. Fan, "Bends and splitters in metal-dielectric-metal subwavelength plasmonic waveguides," Appl. Phys. Lett. **87**(13), 131102 (2005).
15. B. Wang, and G. P. Wang, "Surface Plasmon polariton propagation in nanoscale metal gap waveguides," Opt. Express **29**, 1992–1994 (2004).
16. Z. Han, L. Liu, and E. Forsberg, "Ultra-compact directional couplers and Mach-Zehnder interferometers employing surface Plasmon polaritons," Opt. Commun. **259**(2), 690–695 (2006).
17. R. A. Wahsheh, Z. Lu, and M. A. G. Abushagur, "Nanoplasmonic Directional Couplers and Mach-Zehnder Inerferometers," Opt. Commun. (to be published).
18. A. Taflove, *Computational Electrodynamics* (Artech, Norwood, MA, 1995).
19. J. P. Berenger, "A perfectly matched layer for the absorption for electromagnetic waves," J. Comput. Phys. **114**(2), 185–200 (1994).
20. R. A. Wahsheh, Z. Lu, and M. A. G. Abushagur, "Efficient couplers and splitters from dielectric waveguides to plasmonic waveguides", in Frontiers in Optics, OSA Technical Digest (CD) (Optical Society of America, 2008), paper FThS4. *http://www.opticsinfobase.org/abstract.cfm?URI=FiO-2008-FThS4*

#114470 - $15.00 USD Received 21 Jul 2009; revised 14 Sep 2009; accepted 22 Sep 2009; published 7 Oct 2009

## 1. Introduction

Recent interest arises in plasmonic waveguides (i.e., waveguides in conjunction with surface plasmons), which promise to play an important role in minimizing the footprint required to integrate multiple optoelectronic devices on the same chip. In particular, plasmonic waveguides formed by metal-dielectric-metal (MDM) structures can tightly confine light in the dielectric region on deep sub-wavelength scales [1–4] which is not possible using conventional dielectric waveguides due to diffraction limit [5]. However, the smaller the modal size in the dielectric region of the MDM, the larger the propagation loss due to the metallic losses. The tradeoff between mode confinement and propagation loss can be addressed by integrating both dielectric waveguides and plasmonic waveguides in the same system. To this end, efficient coupling between dielectric waveguides and plasmonic waveguides is of great significance.

It is necessary to use dielectric waveguides to connect the plasmonic devices to the light source and detector so that the propagation losses due to the metallic interaction are dramatically reduced. To achieve that, several different coupling methods have been proposed to increase the coupling efficiency from a dielectric waveguide into a plasmonic waveguide, such as direct coupling [6], multi-section taper [6], λ/4 coupler [7], adiabatic tapered coupler [8], and nonadiabatic tapered coupler [8,9]. Also, several different T- and Y-shaped splitters have been proposed [10–14]. Splitters are used in optical circuit elements and devices such as Mach-Zehnder interferometers (MZIs) [15–17] because they are considered as the platform for the optical sensors. In Y-junctions, the radius of curvature plays an important role in reducing radiation losses and increasing the size of the fabricated devices [10,11]. In T-junctions, the intersection area should be designed to increase the coupling efficiency and reduce back reflection. Coupling efficiency can be increased using a resonant cavity at the intersection area [12], using photonic crystal waveguides [13], or using plasmonic waveguides [14].

A recent numerical simulation demonstrated a coupling efficiency of 68% by directly coupling light from a 300 nm wide silicon waveguide into a 40 nm silver-air-silver plasmonic waveguide [6]. Coupling efficiency was further improved to 93% by using a multi-section taper of a length of 400 nm, which was designed by a genetic global optimization algorithm and analyzed with a finite-difference frequency-domain methodology. In this work, we propose a direct yet efficient short plasmonic coupler of a length of 33 nm to increase the coupling efficiency between a silicon waveguide and a silver-air-silver plasmonic waveguide. Based on the coupler, we also propose a splitter that delivers light from a silicon waveguide into two plasmonic waveguides. To the best of our knowledge, this is the first time that one reports a 1 x 2 splitter from a silicon waveguide into two MDM plasmonic waveguides. The coupling efficiency and the spectrum response of both devices are investigated using the two-dimensional (2D) finite-difference time-domain method [18] with a uniform mesh size of 1 nm to accurately capture the change of the field at the interface between the dielectric and plasmonic waveguides. The fundamental transverse magnetic mode is excited in the single-mode dielectric waveguide and the transmitted power is measured by a power monitor that is placed close to the interface with the single-mode plasmonic waveguide [6]. Then, the coupling efficiency is calculated by normalizing the transmitted power with respect to the input power. The perfectly matched layer is used to attenuate the field within its region without back reflection [19]. The metal losses are included in our simulations and the relative permittivity of the silver at the free-space wavelength $\lambda_o$ = 1.55 μm using the commercial software FullWAVE from RSOFT is -103.7 + 8.1j.

In order to validate our results, we started by simulating the structure proposed by Veronis and Fan [6] and obtained the same coupling efficiency (68%) by directly coupling light from a 300 nm wide silicon waveguide into a 40 nm silver-air-silver plasmonic waveguide. By analyzing the numerical results, it is obvious that the light wave from the dielectric waveguide

#114470 - $15.00 USD Received 21 Jul 2009; revised 14 Sep 2009; accepted 22 Sep 2009; published 7 Oct 2009

excites surface plasmon polaritons (SPPs) along the dielectric-plasmonic boundaries and the SPPs will be "funneled" into the MDM plasmonic waveguides. This funneling process can conceptually explain why light can be efficiently coupled from a large (300 nm) dielectric waveguide into a tiny (40 nm) dielectric slot MDM waveguide. Recently, we found that the coupling efficiency can be greatly improved simply by incorporating a rectangular air-gap (i.e., slot waveguide) and hence preventing transverse "funneling leakage" at the interface between the dielectric waveguide and the MDM plasmonic waveguide [20]. Herein, we present the design steps and numerical results for the proposed air-gap couplers (AGCs) and splitters.

## 2. Air-gap coupler design

First, we consider an ultra-short matching rectangular AGC inside the plasmonic waveguide at the interface with silicon, as shown in Fig. 1(a). In the 2D simulation, we varied the dimensions of the coupler and measured the corresponding coupling efficiency. The dependence of the coupling efficiency on the coupler's width $W$ and length $L$ is shown in Fig. 1(b). We found that coupling efficiency had a maximum value when $W$ matches the width of the silicon waveguide. In particular, the coupling efficiency is above 87.7% for 30 nm < $L$ < 40 nm and is maximized for $L$ = 33 nm (coupling efficiency = 88.1%). Tapering the edges of the rectangular AGC can further increase the coupling efficiency to 90% [20], but doing so will also increase the fabrication complexity. In this work, we only consider the rectangular AGC and optimize its length as 40 nm to match that of the width of the plasmonic waveguide. The field distribution of the coupled light for the rectangular AGC is shown in Fig. 1(c).

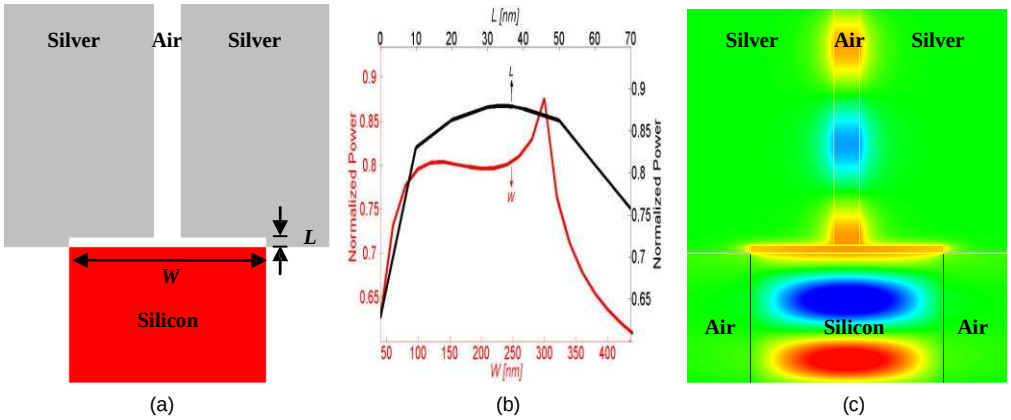


Fig. 1. (a) Schematic of the basic proposed coupler (top view). (b) Coupling efficiency as a function of the coupler's width $W$ and length $L$. (c) Field distribution of the coupled light at $\lambda_o$ = 1.55 μm for the air-gap coupler.

Veronis and Fan [6] found that to maximize the coupling efficiency between the dielectric waveguide and the plasmonic waveguide, there is an optimal width of the dielectric waveguide for a given width of the plasmonic waveguide. As shown in Fig. 2, the optimal width of the dielectric waveguide is 300 nm when the width of the plasmonic waveguide is 40 nm. We found that this dependency is broadened when using our proposed AGC. Increasing the size of the dielectric waveguide from 300 nm to 500 nm resulted in a decrease in the coupling efficiency by about 15% as opposed to 45% for the case without using the AGC.

#114470 - $15.00 USD Received 21 Jul 2009; revised 14 Sep 2009; accepted 22 Sep 2009; published 7 Oct 2009

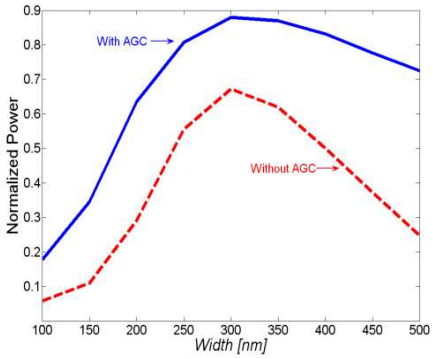


Fig. 2. Coupling efficiency for the basic structure [Fig. 1(c)] as a function of the dielectric waveguide's width.

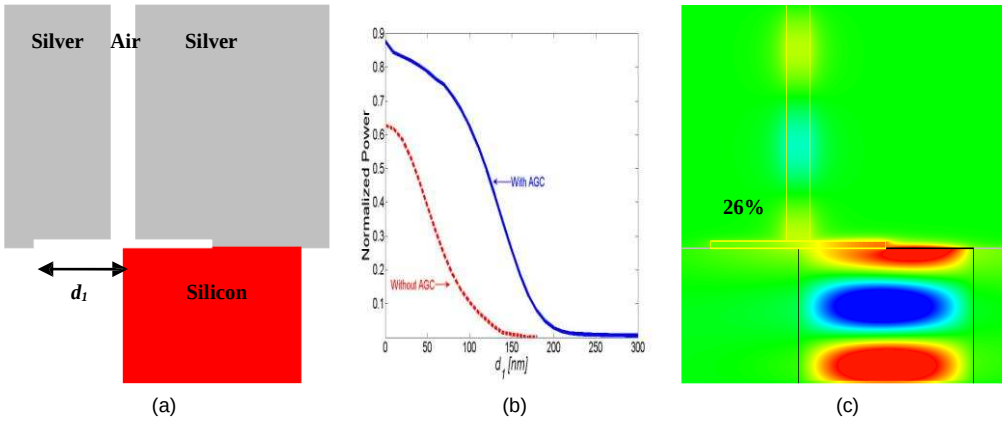


Fig. 3. (a) Schematic of the position misalignment $d_1$ between the silicon waveguide and the plasmonic waveguide with the AGC connected to it. (b) Coupling efficiency as a function of $d_1$. (c) Field distribution for the structure shown in Fig. 3(a) when $d_1$ = 150 nm.

Moreover, our coupler allows for considerable alignment tolerance, which is necessary for practical applications since accurately aligning the silicon waveguide to the plasmonic waveguide is a difficult task. To evaluate the effect of the misalignment, two configurations are examined. One is for the misalignment of both the MDM waveguide and the AGC with respect to the silicon waveguide as a function of the displacement $d_1$ [as shown in Fig. 3(a)]. Another is for the misalignment of the MDM waveguide with respect to both AGC and silicon waveguide as a function of the displacement $d_2$ [as shown in Fig. 4(a)]. The misalignment in both cases is exaggerated in order to show the effect of using the AGC. Figures 3(b) and 4(b) show the coupling efficiency with and without using the AGC as a function of the displacement $d_1$ and $d_2$, respectively. We found that the misalignment tolerance is much higher for both cases when using the AGC. For example, if the plasmonic waveguide center is at the edge of the silicon waveguide (i.e., $d_1$ = 150 nm) as shown in Fig. 3(a), the coupling efficiency is about 1% without using the AGC and about 26% when the AGC is used. In another example, if the MDM waveguide is placed next to the AGC (i.e., $d_2$ = 170 nm) as shown in Fig. 4(c), then coupling efficiency is negligible without using the AGC and about 41% when the AGC is used. Note that there is almost no alignment overlap between the dielectric waveguide and the MDM plasmonic waveguide. From this analysis, it is obvious that in order to achieve high coupling efficiency, the AGC's edges should be aligned to the silicon waveguide edges and the MDM waveguide should be placed at the center of the silicon waveguide.

#114470 - $15.00 USD Received 21 Jul 2009; revised 14 Sep 2009; accepted 22 Sep 2009; published 7 Oct 2009

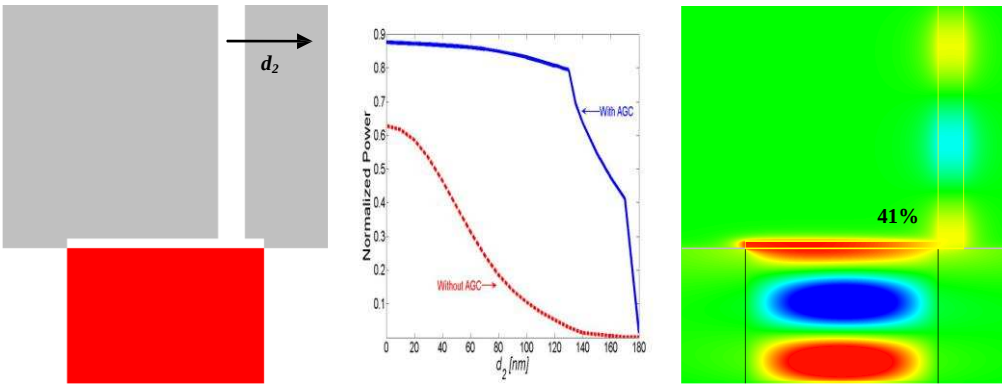


Fig. 4. (a) Schematic of the position misalignment $d_2$ between the silicon waveguide with the AGC connected to it and the plasmonic waveguide. (b) Coupling efficiency as a function of $d_2$. (c) Field distribution for the structure shown in Fig. 4(a) when $d_2$ = 170 nm.

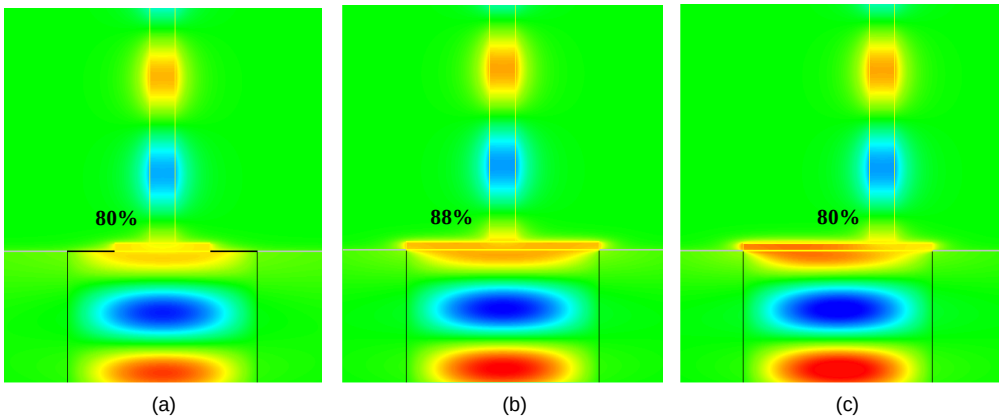


Fig. 5. The electric field distribution when (a) the width of the AGC does not match that of the silicon waveguide, (b) the width of the AGC matches that of the silicon waveguide and the MDM waveguide is at the center, and (c) the width of the AGC matches that of silicon waveguide and the MDM waveguide is not at the center.

In our couplers, the rectangular air-gap plays an important role in increasing both the coupling efficiency (as shown in Fig. 1) and improving the alignment tolerance of the plasmonic waveguide with respect to the dielectric waveguide (as shown in Figs. 3 and 4). To verify this, we made several additional simulations and found that without using the AGC the plasmonic mode was excited at the interface between metal and silicon that had a different mode size than that of the MDM waveguide. After using the AGC, the plasmonic mode size partially matched that of the MDM waveguide because the AGC formed a cavity between the metal and silicon, which enabled more power to couple into the MDM waveguide. When the AGC does not have the same width as that of the silicon waveguide, the SPP excitation starts from the area that is not covered with the AGC. Then the SPP is coupled inside the AGC and propagates towards the MDM waveguide and couples into the MDM waveguide, as shown in Fig. 5(a). When AGC covers the whole silicon area and the MDM waveguide is at the center, as shown in Fig. 5(b), the SPP excitation starts at an equal distance from the MDM waveguide and then is coupled into the MDM waveguide. When the MDM waveguide is not at the center, SPP excitation starts away from the MDM waveguide before it is coupled into the MDM waveguide [Fig. 5(c)]. This proves that the MDM waveguide introduces transverse

#114470 - $15.00 USD Received 21 Jul 2009; revised 14 Sep 2009; accepted 22 Sep 2009; published 7 Oct 2009

metal boundaries that prevent the transverse leakage of SPPs and consequently increases the coupling efficiency.

We can further explain why one structure has higher coupling efficiency than another. For example, the coupling efficiency for the structure shown in Fig. 1(c) has the highest coupling efficiency (about 88%) because the SPP excitation starts at equidistance from both sides of the centered MDM waveguide and are "funneled" into the MDM waveguide. In another example, the coupling efficiency for the structure shown in Fig. 5(a) is less than that for the structure shown in Fig. 1(c) because part of the excited SPP propagates away from the AGC and also the excited SPP mode at the interface between silicon and metal travels towards the AGC, which has a different dielectric material (air). On the other hand, when the width of the AGC is higher than that of the silicon waveguide, the AGC does not act as a cavity because the bottom of the extra length is terminated by air and not by silicon. Thus, the coupling efficiency dropped dramatically.

### 3. Splitter design

Ultra compact splitters are required in nanophotonic circuits in order to minimize the required area to produce multiple photonic devices on the same chip. The coupler introduced in the previous section can be easily used to design splitters. In this section, two methods were used to design splitters: one method by using the AGC and the other one without using the AGC.

In the first method, we designed a 3-dB splitter by increasing the separation distance $g_1$ between the two MDM waveguides [as shown in Fig. 6(a)] until maximum coupling is achieved. We found that the maximum coupling efficiency is about 37% for each branch when $g_1$ = 160 nm, as shown in Figs. 6(b) and 6(c). This configuration has the advantage in easy fabrication.

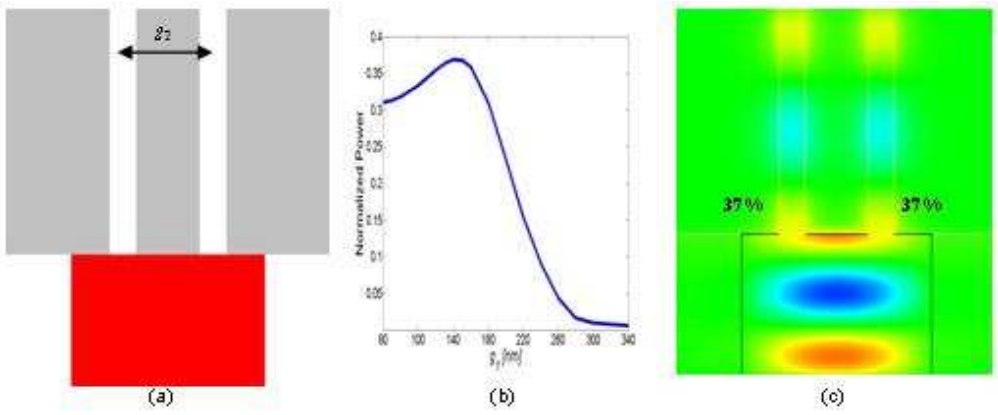


Fig. 6. (a) Schematic of the splitter structure without the air-gap coupler. (b) Coupling efficiency as a function of the separation distance $g_1$. (c) Field distribution for the structure shown in Fig. 6(a) for $g_1$ = 160 nm.

The efficiency can be further increased using the air-gap coupler. In the second method, we designed a 3-dB splitter by increasing the separation distance $g_2$ between the two MDM waveguides [as shown in Fig. 7(a)] until maximum coupling is achieved. The increase in $g_2$ was done after the addition of the rectangular AGC. We found that the maximum coupling efficiency is about 45% for each branch for $g_2$ = 260 nm, as shown in Figs. 7(b) and 7(c). Over 90% of power in total can be delivered into two MDM plasmonic waveguides.

#114470 - $15.00 USD Received 21 Jul 2009; revised 14 Sep 2009; accepted 22 Sep 2009; published 7 Oct 2009

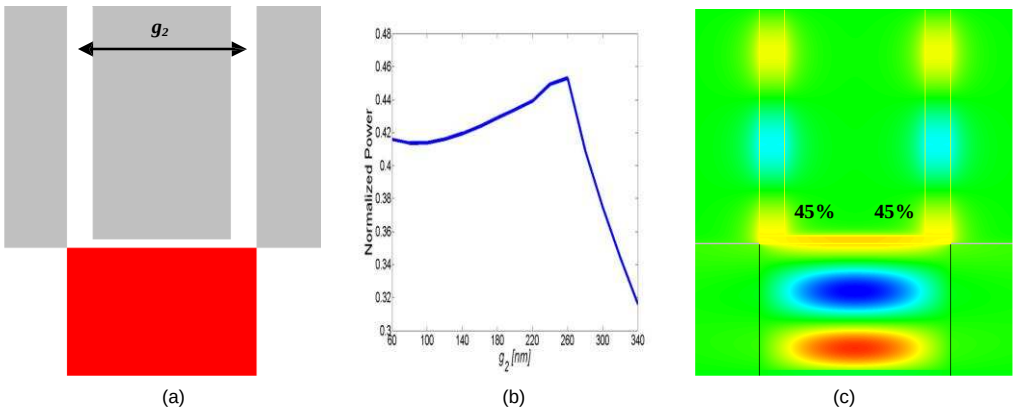


Fig. 7. (a) Schematic of the splitter structure with the air-gap coupler. (b) Coupling efficiency as a function of the separation distance $g_2$. (c) Field distribution for the structure shown in Fig. 7(a) for $g_2$ = 260 nm.

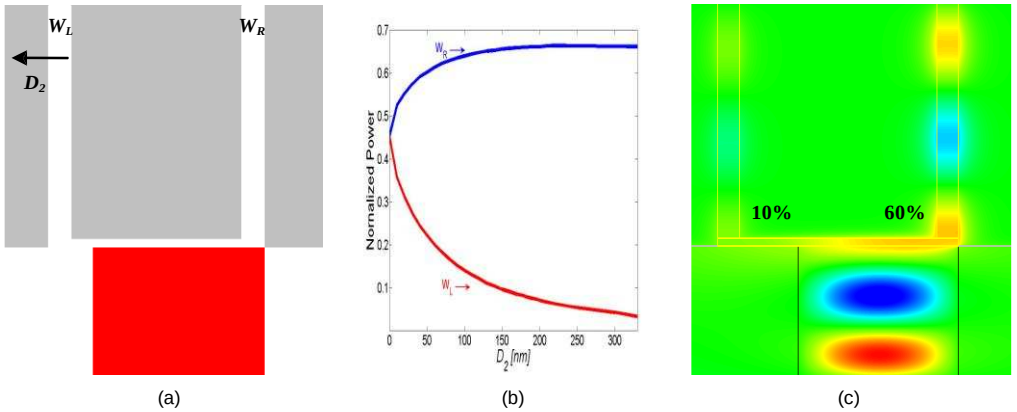


Fig. 8. (a) Schematic of the asymmetric splitter structure. (b) Coupling efficiency as a function of the displacement $D_2$. (c) Field distribution for $D_2$ = 150 nm.

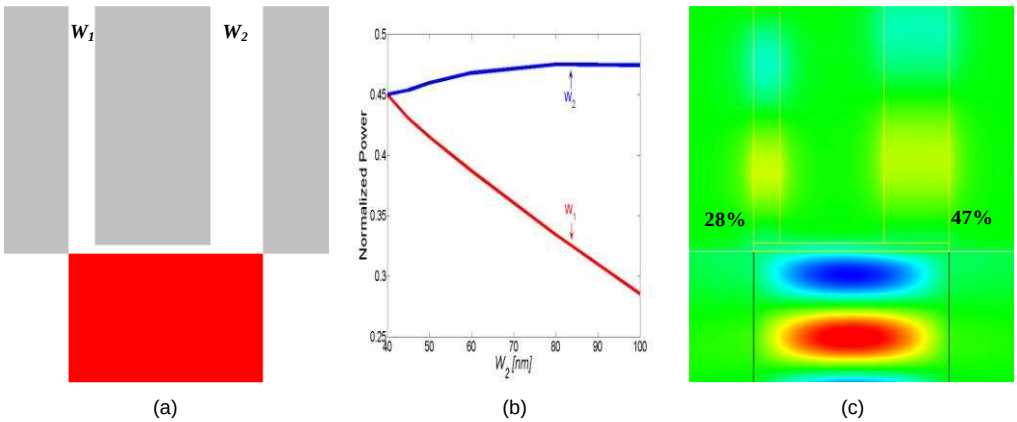


Fig. 9. (a) Schematic of the asymmetric splitter structure. (b) Coupling efficiency as a function of $W_2$. (c) Field distribution for $W_2$ = 100 nm and $W_1$ = 40 nm.

The splitting ratio can be easily controlled by the position of the MDM waveguides $W_R$ and $W_L$, as shown in Fig. 8(a). Before shifting $W_L$, the displacement between the two

#114470 - $15.00 USD Received 21 Jul 2009; revised 14 Sep 2009; accepted 22 Sep 2009; published 7 Oct 2009

waveguides was 260 nm, which resulted in a coupling efficiency of 45%. As expected, we found that as $D_2$ increases, coupling efficiency into the shifted waveguide decreases and coupling efficiency into the fixed waveguide increases [as shown in Fig. 8(b)]. Figure 8(c) shows the coupling efficiency ratio between $W_L$ and $W_R$ for $D_2$ = 150 nm. Even when there is no overlap between the shifted MDM waveguide and silicon waveguide, the coupled power is about 10% in $W_L$.

Another way to control the splitting ratio is by varying the width of MDM waveguides $W_1$ and $W_2$, as shown in Fig. 9(a). We found that as the width of $W_2$ increases from 40 nm to 100 nm, the coupling efficiency in $W_2$ increases slightly from 45% to 47%, while the coupling efficiency in a 40 nm wide $W_1$ decreases from 45% to 28% [as shown in Fig. 9(b)]. The field distribution for $W_2$ = 100 nm and $W_1$ = 40 nm is shown in Fig. 9(c).

## 4. Spectrum analysis

The proposed couplers and splitters can also operate at a broad frequency range. To show that, we varied the wavelength of the light source and measured the corresponding coupling efficiency. The coupling efficiency with respect to wavelength for the structures shown in Figs. 1(c) (with and without AGC), 5(c), and 6(c) is shown in Fig. 10(a). Using AGC broadens the spectrum range around the communication wavelength 1.55 μm for all structures. Using two plasmonic waveguides in addition to AGC broadens the spectrum over longer range. The wavelength dependent of the permittivity of metal is not very clear because the coupling efficiency is measured close to the interface with silicon. If the coupling efficiency is measured far away from the interface, then it will be obvious that the losses of the metal increase significantly as the wavelength decreases.

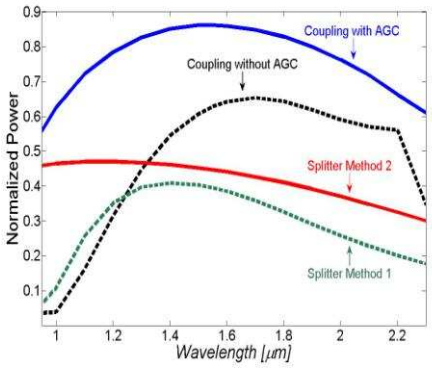


Fig. 10. Spectrum of the structures shown in Fig. 1(c) (with and without the AGC) and Figs. 5(c) and 6(c).

## 5. Conclusions

To summarize, we showed that a matching coupler at the interface between a dielectric waveguide and a plasmonic waveguide can be designed to increase the coupling efficiency as well as the alignment tolerance when aligning a dielectric waveguide to a plasmonic waveguide. In addition, based on the efficient couplers, nano-scale plasmonic 1 x 2 splitters can be designed with a coupling efficiency of 45% for each branch that operates at the optical telecom wavelength. The splitting ratio can be controlled by varying either the relative position or width of the two branches. Finally, we investigated the spectrum of the proposed structures and found that using the air-gap coupler broadens the spectrum around the optical communication wavelength. Two potential applications of our proposed coupler and splitter: a directional coupler and a Mach-Zehnder interferometer are presented in [17].

#114470 - $15.00 USD Received 21 Jul 2009; revised 14 Sep 2009; accepted 22 Sep 2009; published 7 Oct 2009

# APPENDIX C

# Nanoplasmonic Directional Couplers and Mach-Zehnder Interferometers

This appendix provides a copy of the following publication[1]:

R. A. Wahsheh, Z. Lu, and M. A. G. Abushagur, "Nanoplasmonic Directional Couplers and Mach-Zehnder Interferometers," Optics Communications, vol. 282, September 2009, pp. 4622-4626.

[1]Reprinted from Optics Communications, vol. 282, R. A. Wahsheh, Z. Lu, and M. A. G. Abushagur, "Nanoplasmonic Directional Couplers and Mach-Zehnder Interferometers," September 2009, pp. 4622 4626, Copyright 2009, with permission from Elsevier.

Optics Communications 282 (2009) 4622–4626

Contents lists available at ScienceDirect

Optics Communications

journal homepage: www.elsevier.com/locate/optcom

# Nanoplasmonic directional couplers and Mach–Zehnder interferometers

Rami A. Wahsheh, Zhaolin Lu *, Mustafa A.G. Abushagur

*Microsystems Engineering, Kate Gleason College of Engineering, Rochester Institute of Technology, Rochester, NY 14623, USA*

ARTICLE INFO

*Article history:*
Received 28 July 2009
Received in revised form 24 August 2009
Accepted 24 August 2009

*PACS:*
42.79.Fm
42.79.Gn

*Keywords:*
Integrated optics devices
Waveguides
Surface plasmons

ABSTRACT

We present a novel design and analysis of two nano-scale plasmonic devices: a directional coupler and a Mach–Zehnder interferometer. The designs of the two devices are based on our recent work on the air-gap coupler that resulted in high coupling efficiency between a dielectric waveguide and a plasmonic waveguide. The two devices are embedded between two dielectric waveguides and operate at optical telecom wavelengths. The overall efficiency was 37% for a 2×2 directional coupler switch and above 50% for the proposed designs for a Mach–Zehnder Interferometer. The efficiency in the proposed devices can be increased using broader plasmonic waveguides.



## 1. Introduction

Surface plasmon polariton (SPP) occurs at the interface between metal and dielectric material due to the interaction between the free surface electrons with the incident photons [1–3]. Thus, light can be confined in ultra small dimensions. To confine light further in the dielectric region, the dielectric region is put between two metals. In this configuration, the decaying SPP mode at each dielectric–metal interface interacts with the other, creating a confined light in the dielectric region. The dielectric width can be far below the diffraction limit because as the dielectric width decreases the effective refractive index increases. Reducing the width of the dielectric region improves the mode confinement and decreases the propagation length [4,5]. The propagation length is decreased because as the mode confinement increases, the interaction with metal increases and consequently the losses increase.

Several different optical circuit elements and devices such as directional couplers [6–8] and Mach–Zehnder interferometers (MZIs) [8,9] have been proposed because they are considered as the platform for the optical sensors. To the best of our knowledge none of the proposed directional couplers and MZIs in the literature has dealt with the coupling from a dielectric waveguide into a plasmonic waveguide and back into the dielectric waveguide, which is taken into consideration in our work. It is necessary to use dielectric waveguides to connect the plasmonic devices to the light source and detector so that the propagation losses due to the metallic interaction are dramatically reduced. The size of the directional coupler depends on the separation distance between the two adjacent waveguides, widths of the waveguides, the refractive index of the waveguides, the refractive index of metal, and the operating wavelength. Zia et al. [4] found that negligible cross talk between two adjacent metal–dielectric–metal waveguides occurs when the separation distance between the two waveguides is greater than 150 nm. Traditional dielectric directional couplers are used as splitters in which there is a 90° phase shift between the two split beams. A different phase behavior occurs in metal–dielectric–metal directional couplers in which the phase difference between the two split beams is less than 90° [9]. Wang and his co-worker [9] attribute this phase behavior to the interaction of the field with the complex refractive index of metal. Unlike traditional dielectric directional couplers, plasmonic directional couplers have wavelength coupling dependence because the real part of the complex refractive index of metal changes as wavelength changes [7].

In our previous work [10,11], we proposed a direct yet efficient short plasmonic air-gap coupler (AGC) to increase the coupling efficiency between a silicon waveguide and a silver–air–silver plasmonic waveguide. We also proposed a splitter that delivers light from a silicon waveguide into two plasmonic waveguides achieving a coupling efficiency of 45% for each branch. In this work, we present two potential applications of our proposed coupler and splitter: a directional coupler and a Mach–Zehnder interferometer.

* Corresponding author. Tel.: +1 585 475 2106.
*E-mail addresses:* raw7949@rit.edu (R.A. Wahsheh), zxleen@rit.edu (Z. Lu), maaeen@rit.edu (M.A.G. Abushagur).

0030-4018/$ - see front matter © 2009 Elsevier B.V. All rights reserved.
doi:10.1016/j.optcom.2009.08.045

To this end, we used the finite-difference time-domain method to simulate all the proposed two-dimensional structures. The mesh size was 1 nm which is small enough to capture the change of the field at the interface between the dielectric waveguide and the plasmonic waveguide. The transverse magnetic mode was excited in the dielectric waveguide and the transmitted power was measured close to the interface with the plasmonic waveguide. Perfectly matched layers were used to attenuate the field within its region. The metal losses were included in our simulations. The relative permittivity of the silver at the free space wavelength $\lambda_o = 1.55\ \mu m$ was $-103.7 + 8.1j$.

## 2. Plasmonic directional coupler

Fig. 1a shows the schematic of the proposed plasmonic directional coupler. It consists of two air-gap slot waveguides (AGSWs), $W_1$ and $W_2$. $W_1$ was kept connected to the air-gap coupler (AGC) while $W_2$ had a separation distance of 80 nm from the top of the AGC. We studied the effect of changing the separation distance between the two AGSWs, $D_3$, on the efficiency into $W_2$. Fig. 1b shows the coupling efficiency as a function of the overlapped propagation length, $L$, between $W_1$ and $W_2$ for two cases when $D_3 = 10$ and 220 nm. As expected, as $D_3$ increases, the cross talk between the two AGSWs decreases and the coupling length increases. The coupling length, $L_c$, is defined as the propagation length needed to completely transfer light from $W_1$ to $W_2$. The attenuation of the coupled power as $L$ increases is due to the metallic losses. Our simulation results show that $L_c$ increased from 870 (Fig. 1c) to about 1700 nm (Fig. 1d) as $D_3$ increased from 10 to 20 nm, respectively. Also, our simulation results show that the cross talk between the two AGSWs is negligible when $D_3$ is larger than 150 nm. The coupling length at which the maximum value of the transferred power occurs is slightly off than that of the minimum value of the other waveguide. Zhao et al. [7] attributed the position offset to the interaction of the field with the complex refractive index of metal.

An efficient and compact directional coupler can be made when $D_3 = 10$ nm. The power is continuously coupled from one AGSW to another along the propagation direction (Fig. 1c). Total power transfer occurs when the propagation length is equal to about 870 nm. A 3 dB coupler (~40% in each branch) can be made when the propagation length is equal to 453 nm.

Fig. 2 shows a 2×2 directional coupler switch in which light propagates through port 1 and exits through port 4 when total coupling occurs. The spacing between the two input- (or output-) ports is 320 nm and that between the s-shaped bends is 380 nm. The spacing ensures no cross talk between the waveguides. The s-shaped bends did not start from the center of the AGC to reduce the size of the switch and the propagation losses. The trade-off is that 4% of the coupling efficiency is lost at each interface [11]. The width of the two AGSWs is 40 nm, whereas the separation distance between them within the coupling region is 10 nm. Fig. 2b shows the efficiency into ports 3 and 4 as a function of the coupling

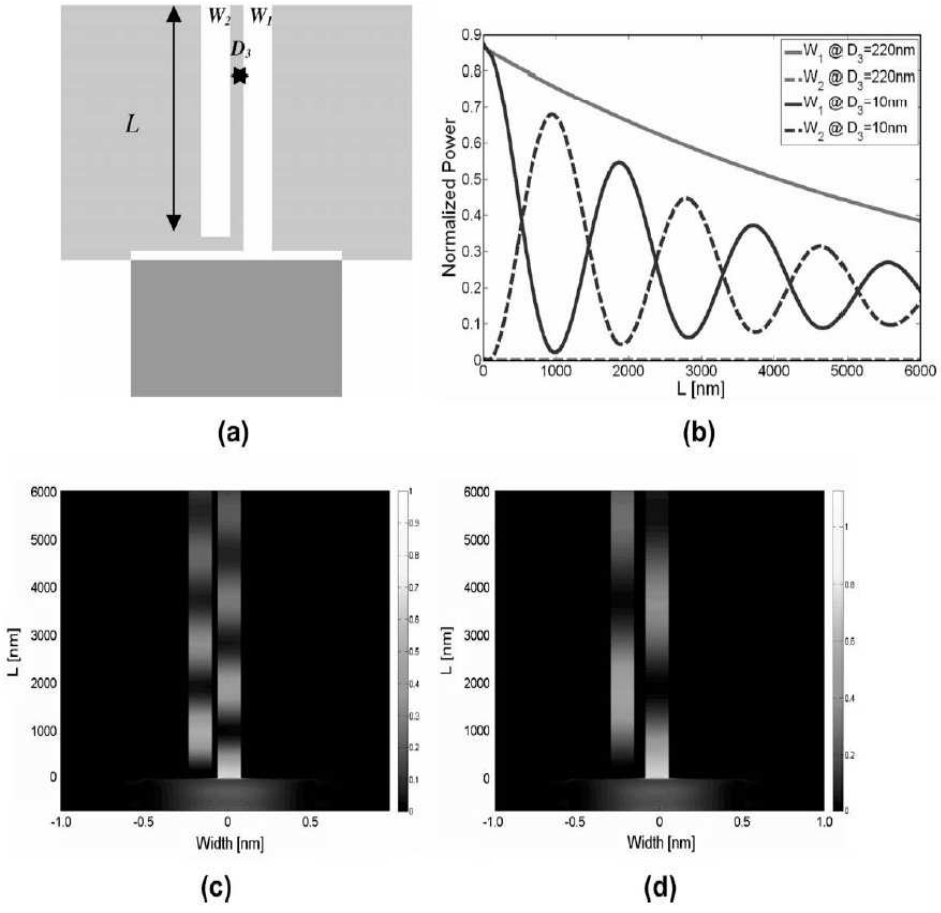


**Fig. 1.** (a) Schematic of the directional coupler structure. (b) Coupling efficiency as a function of the overlapped propagation length, $L$, between $W_1$ and $W_2$ at different values of $D_3$. (c,d) Power density profile for $D_3 = 10$ and 20 nm, respectively.

length, $L_D$. As $L_D$ increases the power is periodically transferred between the two ports. The interaction length required to achieve total power transfer is equal to 910 nm (see Fig. 2c). The excess loss is about −16 dB (coupling efficiency inside port 4 is 37%), while the isolation is about −23 dB (cross talk in port 3). A 3 dB beam splitter can be achieved when $L_D$ is equal to about 440 nm.

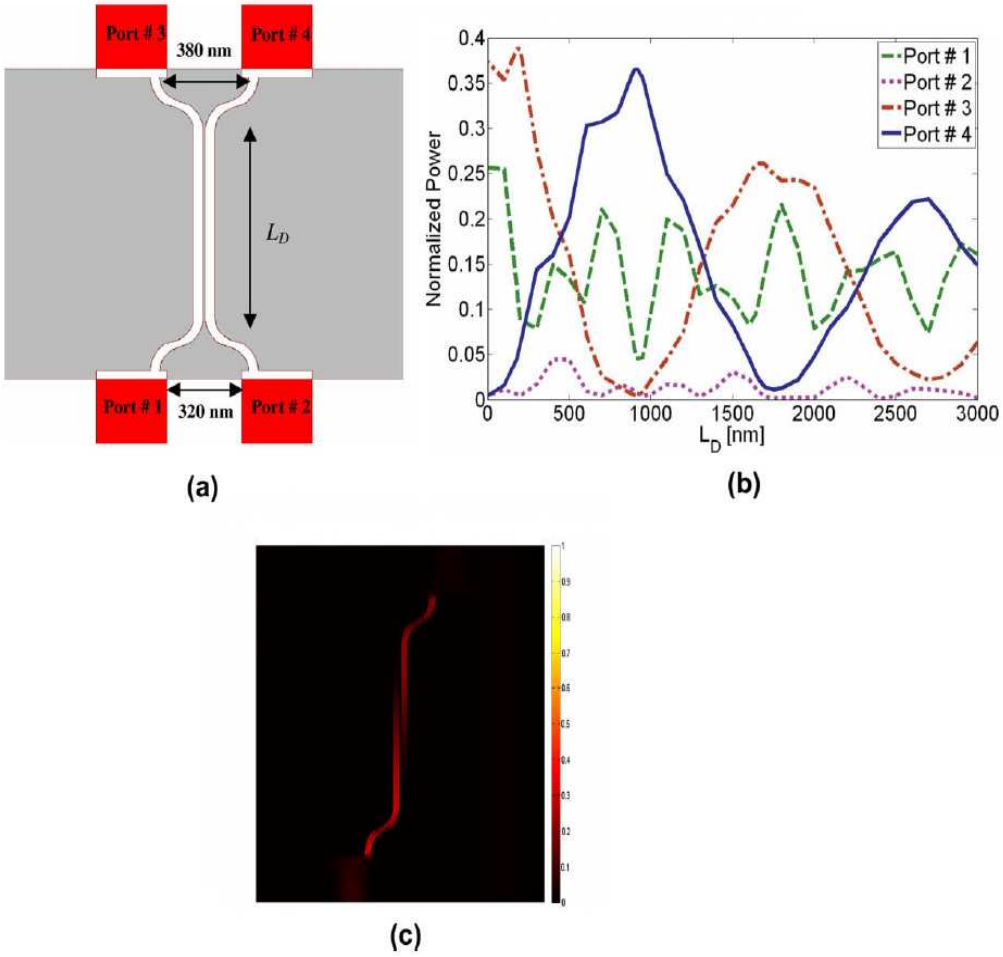


**Fig. 2.** (a) Schematic of the switch structure. (b) Coupled power into each port as a function of $L_D$. (c) Power density profile for the proposed switch when $L_D$ = 910 nm.

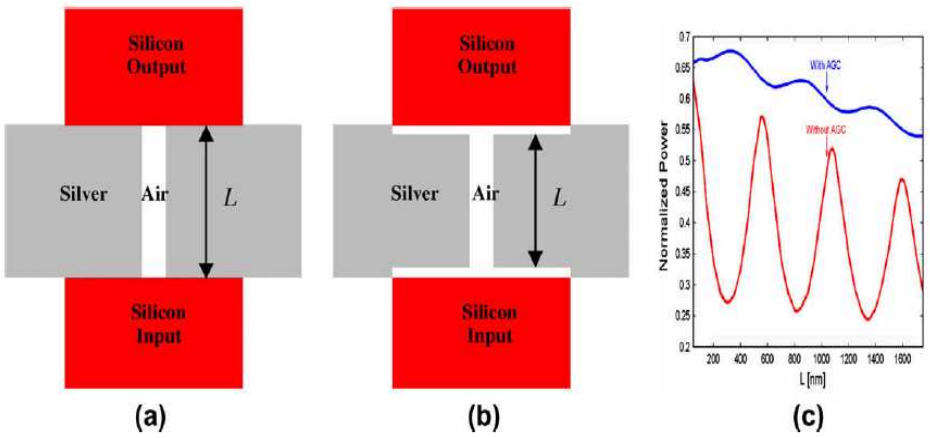


**Fig. 3.** (a, b) Schematic of the Fabry–Perot cavity structures with and without the AGC, respectively. (c) Efficiency as a function of the AGSW length, $L$.

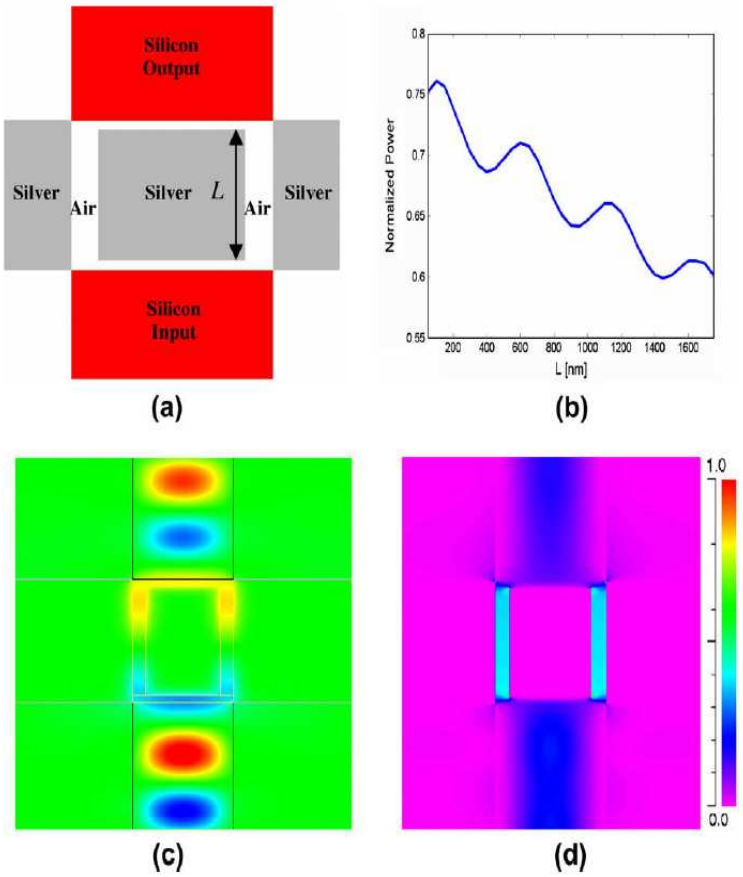


**Fig. 4.** (a) Schematic of the proposed silver–air–silver Mach–Zehnder interferometer. (b) Output power as a function of Mach–Zehnder arm length, $L$. (c, d) Field distribution and power density profile for $L = 600$ nm, respectively.

### 3. Plasmonic Mach–Zehnder interferometer

Coupling light in and out of the plasmonic waveguide can be achieved by using one of the Fabry–Perot cavity structures as shown in Fig. 3a and b. One structure (Fig. 3a) consists of a 40 nm-wide AGSW embedded between two silicon waveguides. The other structure (Fig. 3b) consists of a 40 nm-wide AGSW and two AGCs embedded between two silicon waveguides. The coupling efficiency into the output silicon waveguide as a function of the AGSW length, $L$, for both structures is shown in Fig. 3c. Efficiency decreases as $L$ increases because of the propagation losses due to the metallic absorption. The oscillation in the measured coupling efficiency was dramatically reduced by using the two AGCs. Also, higher coupling efficiency was achieved by using the two AGCs.

Based on our recent work on a 3 dB splitter [10,11], we propose two designs for an MZI using silver–air–silver geometry. The first

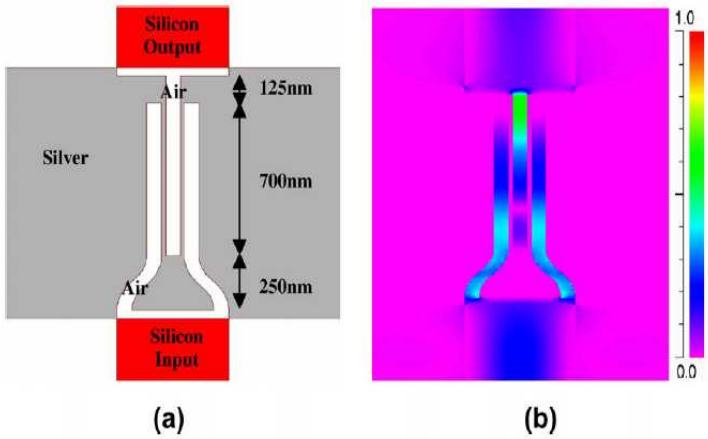


**Fig. 5.** Schematic of the proposed three-waveguide silver–air–silver Mach–Zehnder interferometer. (b) Power field distribution.

design is achieved by connecting two splitters back to back, as shown in Fig. 4a. In this configuration, the input light is equally split into each AGSW and then recombined at the output silicon waveguide. The two AGSWs form the Mach–Zehnder propagation arms. The separation between the AGSWs is 220 nm. The output power was measured at the output silicon waveguide as a function of the Mach–Zehnder arm length, $L$, (Fig. 4b). The oscillation in the measured coupling efficiency is due to the Fabry–Perot cavity response that is caused by the reflection of the plasmon mode from each dielectric waveguide. Efficiency decreases as $L$ increases because of the propagation losses due to the metallic absorption. Fig. 4c and d show the electric field intensity and the power density profile for the proposed structure. It is clear that the input light is equally split into the two AGSWs arms and recombines at the output dielectric waveguide. A potential application of this structure is in integrated optical sensors [12], where the electromagnetic field in the gap between the two AGSWs is strongly confined that can be easily disturbed by an external effect.

We propose another MZI structure that consists of a splitter and a directional coupler (a three-waveguide coupler structure), as shown in Fig. 5a. The input light is equally split into the two AGSWs arms and recombines at the middle AGSW before it couples into the output dielectric waveguide. The field is highly localized at the end of the middle MZI arm (Fig. 5b). The coupling efficiency is about 53% when the interaction length is about 703 nm and the width of the metal between the three AGSW is 10 nm. The length of the MZI structure can slightly be reduced by placing the central AGSW between the two s-shaped plasmonic waveguides.

## 4. Conclusion

We showed how a compact size plasmonic 2×2 directional coupler switch and a plasmonic Mach–Zehnder interferometer (MZI) can be designed. The efficiency in the former one was 37%, and that in the latter one was above 50%. The coupling efficiency can be increased by using broader plasmonic waveguide.

## References

[1] E.N. Economou, Physical Review 182 (1969) 539.
[2] D.F.P. Pile, T. Ogawa, D.K. Gramotnev, Y. Matsuzaki, K.C. Vernon, K. Yamaguchi, T. Okamoto, M. Haraguchi, M. Fukui, Applied Physics Letters 87 (2005) 261114.1–261114.3.
[3] W.L. Barnes, A. Dereux, T.W. Ebbesen, Nature 424 (2003) 824.
[4] R. Zia, M.D. Selker, P.B. Catrysse, M.L. Brongersma, Journal of the Optical Society of America A – Optics Image Science and Vision 21 (2004) 2442.
[5] L. Liu, Z. Hana, S. Hea, Optics Express 13 (2005) 6645.
[6] Z. Kang, G.P. Wang, Optics Express 16 (2008) 7680.
[7] H. Zhao, X.G. Guang, J. Huang, Physica E 40 (2008) 3025.
[8] Z. Han, L. Liu, E. Forsberg, Optics Communications 259 (2006) 690.
[9] B. Wang, G.P. Wang, Optics Express 29 (2004) 1992.
[10] R.A. Wahsheh, Z. Lu, M.A.G. Abushagur, Frontiers in Optics, OSA Technical Digest (CD), Optical Society of America, 2008, paper FThS4. <http://www.opticsinfobase.org/abstract.cfm?URI=FiO-2008-FThS4>.
[11] R.A. Wahsheh, Z. Lu, M.A.G. Abushagur, Optics Express, submitted for publication.
[12] J. Topol'ancik, P. Bhattacharya, J. Sabarinathan, P.-C. Yu, Applied Physics Letters 82 (2003) 1143.